

ABSTRACT

GOZEN, ARIF OMER. Lateral Structuring and Stability Phenomena Induced by Block Copolymers and Core-Shell Nanogel Particles at Immiscible Polymer/Polymer Interfaces. (Under the direction of Jan Genzer and Richard J. Spontak).

We have investigated the parameters such as copolymer/nanoparticle concentration, architecture and molecular weight combined with film thickness, time and temperature in order to develop a molecular-level insight on how lateral interfacial structuring occurs at immiscible polymer/polymer interfaces.

In order to develop a molecular-level understanding of how these ‘smart’ self-assembling materials and core-shell nanogel particles interact both intra- and inter-molecularly and form ordered structures in bulk, as well as at immiscible interfaces, we first focused on the response of core-shell polymer nanoparticles, designated CSNGs, composed of a cross-linked divinylbenzene core and poly(methyl methacrylate) (PMMA) arms as they segregate from PMMA homopolymer. We have demonstrated that these nanogel particles exhibit autophobic character when dispersed in high molecular weight homopolymer matrices and segregate to the interface with another fluid.

We have further explored the migration of these new-generation nanogel particles (CSNG-Rs) segregating from PS homopolymer to PS/PMMA interfaces. Unlike the instability patterns observed with the CSNGs, which exhibit classical nucleation and growth mechanism with circular hole formation, we have observed an intriguing dewetting pattern and CSNG-Rs forming lateral aggregates and tentacle-like structures at the interface.

In parallel with our core-shell particle studies, we have also explored the structuring of copolymer molecules that are far from equilibrium in bulk and complex laminate of polymer thin films. Our early triblock copolymer studies have proven that molecular asymmetry has a profound effect on order-disorder transition temperature.

We focused primarily on the effect of the copolymer chemical composition (i.e., block sizes) on the dewetting behavior of PS/SM thin films on PMMA. We elucidate the interfacial segregation and concurrent micellization of diblock copolymers in a dynamically evolving environment with changing boundary conditions as spherical holes develop. These studies reveal that in-plane interfacial nanostructures produced by block copolymers may not always provide stabilization of the bilayer; this behavior has been attributed to the interplay between copolymer micellization and copolymer segregation at the immiscible polymer interface.

Lastly, we have investigated the dewetting behavior of PS/PMMA assemblies containing compositionally varied mixtures of mirrored copolymers, such as PS₅₀-*b*-PMMA₁₀ / PS₁₀-*b*-PMMA₅₀ and PS₅₀-*b*-PMMA₂₀ / PS₂₀-*b*-PMMA₅₀. The dewetting rates of systems composed of copolymer mixtures lie between those of systems modified with the neat copolymers. This observation suggests that the dewetting behavior of the double layer with a copolymer mixture may be approximated satisfactorily by a linear rule of mixtures.

Lateral Structuring and Stability Phenomena Induced by Block Copolymers and Core-Shell
Nanogel Particles at Immiscible Polymer/Polymer Interfaces

by
Arif Omer Gozen

A dissertation or submitted to the Graduate Faculty of
North Carolina State University
in partial fulfillment of the
requirements for the degree of
Doctor of Philosophy

Chemical Engineering

Raleigh, North Carolina, USA

2010

APPROVED BY:

Prof. Jan Genzer
Chair of Advisory Committee

Prof. Richard J. Spontak
Co-Chair of Advisory Committee

Prof. Peter Kilpatrick

Prof. Orlin Velev

Dedication

August 3rd, 2004... the day I left Istanbul to start a completely new life. I was very nervous because I did not know what to expect, on the other hand, I was unbelievably excited and all I knew was I had always wanted this so bad, but, beyond all, I was far to recognize the situation until I started packing my bags the night before. I still remember it like yesterday that none of us at home could look at each other in the eye, without shedding a single teardrop. We all knew that this leave was going to be different this time, a great, but, a longer one. None of us expected the unfortunate losses we have had along the way though... So soon... This great journey has been a total rollercoaster for me. Although I was very fortunate to cross paths with so many absolutely wonderful people, there were times that I was so close to lose my faith, and more importantly, my will to complete this journey. With the greatest and unconditional love given to me by my dear parents and sister, I was able to stand up again and carry on with my mission. They are the reason of the person that I have become; thus, I dedicate this work to them and to the ones that are, physically, no longer with us from the bottom of my heart.

Canım Ablam... My love for you is beyond words, defies explanations. Your presence in this world, to me, is my greatest inspiration. It would have been impossible to carry on without your endless support and love. Since I was born, you have always picked me up whenever I was down. You mean the world to me!

Canım Annem, fedakar Annem... Seni çok seviyorum. Varlığın için, tüm sevgin ve desteğin için, geceyarıları telefonlarda ağlamalarımı dinleyip içimi dökmeme izin verdiğin

için, benimle ağladığın için ve beni bugünlere getirdiğin için sana minnettarım. Bundan sonra herşey çok daha güzel olacak!

Canım Babam... I have always lived for this day to write this dedication letter to you, but never in a million years, would I have imagined that I would have to do it without your presence... You were always there for me; only one phone-call away to talk to me, comfort me, and tell me “Don’t worry about it, Son, everything is going to be okay”... You were my motivation, inspiration... everything! I know that you are always with me, and will always be... Everybody misses you so much, but me, the most... May your soul rest in peace wherever you are. I LOVE AND MISS YOU SO MUCH!

*I won't be afraid
I'll be alright if you help me
I know you're looking down from heaven
And I won't let you down
I'll be everything you taught me
And all that I know is
I'll wait patiently to see you in heaven...*

Biography

Arif Omer Gozen was born on July 31st, 1981 in Istanbul, Turkey. He has one elder sister, Elif, who is one of the leading businesswomen in phone banking in Turkey. Growing up, Omer always suffered from having excessive amounts of energy and he mostly spent it on causing trouble for Elif, racing motorcycles, jumping off high places, doing acrobatics, poking crab nests with his bare hands, swimming, singing songs in languages he didn't know, dancing etc.

He has always been a very persistent person with his demands and developed his communication skills accordingly to obtain what he wants (as a kid, at first, these were mostly food-oriented such as junk food, corn, soda, chewing gum, candies, cookies etc.).

He has always had an enormous love for his family, and his loved dog, Kuki. He is a 14-year-old black/white Cocker Spaniel (and you do not want to know what kind of a trick Omer pulled to convince his parents to adopt Kuki!).

Omer is extremely competitive when it comes to playing sports and he thinks he inherited this from his father, who was a three-time former dirt-bike champion of Turkey. He also did stunts in many movies in the 70's. Omer learned how to ride a motorcycle before learning to ride a bicycle, which he hates. He believes that riding motorcycles is in his blood and he has never lost his obsession for motorcycles since then, and fast things with no roof on the top in general. He always has been very adventurous and fascinated with fast cars. As youngster growing up, one of his favorite activities was to hitch hike and ride in sports cars (No, that habit no longer exists!)

He has learned how to swim, after a few failing attempts, at the age of two without any help (As a result of those attempts he can hold his breath for over 3 minutes). Omer has been always fortunate to study by the sea. That is why Omer absolutely adores his city, Istanbul. He went to Kabatas Erkek High school located by the infamous Bosphorus and he never hesitated to dive in to the cold waters of Bosphorus even a bit during the lunch breaks. Omer has never lost his interest in swimming (after swimming competitively in college, he switched lanes –literally– and started playing water polo as soon as he joined NCSU in Fall 2004).

After high school, he first attended the department of Chemical Engineering at Istanbul Technical University for the freshman year, then, transferred to the department of Chemical Engineering at Bogazici University. In his junior year, he developed an interest in the world of polymers when he met his thermodynamics professor, Ms. Turkan Haliloglu (although he had thought that she was from somewhere out of the space by the end of her first lecture) During the last two years in college, he took many courses in fundamentals of polymers, statistical mechanics, advanced thermodynamics and gained research experience on molecular dynamics studies on protein folding/unfolding under the supervision of Ms. Haliloglu (then, Ms. Haliloglu and Omer were finally on the same page!)

In August 2004, he joined the department of Chemical and Biomolecular Engineering at North Carolina State University to pursue his doctorate degree in polymer science and nanotechnology, specifically to reversibly pattern or functionalize polymer surfaces via smart materials (*e.g.* nanogel particles and self-assembly *via* block copolymers) for applications requiring responsive nanolithography. Over the summer 2009, he worked as a PhD intern in

Procter & Gamble Co. at Beauty Care-Technology Division on developing novel materials for hair styling products.

If he had not pursued a career to be a scientist, he would have probably chosen to be in language-related studies, drama/acting/dancing or an athlete (of course it is never too late for anything!)

Acknowledgments

My sincerest appreciation goes to my advisers, Prof. Jan Genzer and Prof. Richard J. Spontak, for, first of all, believing in me, and their great motivation and continuous support over the course of this journey, during the hard times especially.

Dear Rich, you mean more than just an adviser to me. Thank you for sharing all of your experience and expertise on shaping my career and helping my personal development.

Dear Sir, *píši Vám, ne jako Váš student, ale jako někdo, koho jste velmi inspiroval během této dlouhé cesty. Měl jsem velké štěstí, že jsem Vás potkal a mohl pracovat pod Vaším vedením. Za posledních pět let jste zanechal nesmazatelnou stopu v mém životě i v mém srdci a jsem Vám vděčný za každý okamžik. Vždy si Vás budu pamatovat jako skvělého přítele s obrovským srdcem a neobyčejným duchem. Jste ta nejlepší věc, která může potkat studenta doktorského studia. Bez Vás by byla tato cesta nemožná. Děkuji Vám za nekonečnou podporu.*

I would like to thank my committee members, Prof. Orlin Velez and Prof. Peter Kilpatrick for their guidance and insightful comments on my work and making this work possible.

I am utterly grateful to all my teachers, instructors and professors, who, at some point in my life, have affected me as a person or as a role model during my entire education. Amongst all these people, my most special thanks go to, first, Prof. Turkan Haliloglu in the department of Chemical Engineering at Bogazici University, Turkey, who introduced me to the wonderful world of polymers and strongly encouraged me to pursue a doctorate degree. Secondly, Prof. Birgul Tantekin-Ersolmaz in the department of Chemical Engineering at

Istanbul Technical University, Turkey, encouraged me to apply to NCSU. I could not express how impactful their roles have been in my life.

I would like to give my greatest appreciation to the outstanding faculty of the department of Chemical and Biomolecular Engineering at North Carolina State University, first of all, for accepting me to their doctorate program, giving me the opportunity prove myself to pursue this career path and guiding me with their expertise whenever I needed. I am specifically thankful to, Prof. Kirill Efimenko for his guidance in our laboratories, Prof. Saad Khan, Prof. Greg Parsons, Prof. Orlin Velez, Prof. Michael Dickey, and Prof. Wesley Henderson for granting me access to their laboratories.

The greatest staff of all times: Ms. Sandra “The Queen” Bailey, Ms. Diane Harper, Ms. Saundra Doby, Ms. Rajani Verghese, Ms. Sheila Hayes, Ms. Gwen “My Lady” Johnson, Mr. Kit Yeung, Ms. Shirley Kow, Ms. Clarice Whitmarsh, Ms. Angela Efimenko. You are all wonderful people and you have made this possible. Thank you for all your help and doing things without me even having to speak a word!

Over the past years, I have had the pleasure of being a part of two great research groups and interacting with incredibly talented people. First of all, from the current and past members of the GIRLS: Dr. Bin Wei, Dr. Julie Willoughby, Dr. Young Kuk Jhon, Dr. Hyun-Kwan Yang, Jason Stone, Salomon Turgman, Evren Ozcam, Erich “the Rocket” Bain, Casey Galvin, Shafi Arifuzzaman, Kiran Goli, Xiaojing Cai and the Polymer Morphology Group, a.k.a PMG: Anand Patel, Xiaoyu Sun, Michelle Bowman Gaines, Chris Aberg, Juan Weaver, Kristen Roskov, Arjun “Cajun” Krishnan and Pruthesh Vargantwar. It has been a blast with all of you guys!

I would like to thank Daniel Halbert and Peter Cronin from Siemens Healthcare Diagnostics (formerly Dade Behring) for giving me the opportunity to gain experience in the field of gel nanocomposites and also providing my PhD funding.

During my internship at Miami Valley Innovation Laboratories (MVIC), P&G Co, OH, I had the great opportunity of working with Dr. Randy Washington. I have learned so much from our fruitful discussions. I cannot possibly thank him and Dr. Steve Smith enough for making one of my greatest dreams come true.

Raleigh stands out as one of the best experiences of my life and I owe that solely to the wonderful people from all over the world and every possible nationality, I have crossed paths over the past 5.5 years. They have affected me in so many great ways, and more importantly, made me even further develop as a very open-minded human being who truly appreciates different cultures. I truly value your friendship so much. Amongst these great friends, there are some very special souls that have become my family abroad. I would like to thank a few special ones here that have touched my heart in every possible way a human being could. Even though they joined the department one year after I started, Evren and Murat quickly became the brothers I have never had. Since then we have been inseparable. Their beautiful families have always treated me as one of their own children. I am very fortunate and humbled to have them in my life.

Evren, az zamana o kadar cok sey sigdirdik ki! Doktora ogrencisi yasamini en kral biz yasadik. Benim icin yerin cok ayri.

And many other special people: Murat, Mehmet, Ozan, Melda, Tugce, Can Sezer, Erdem, Acar, Elif, Ozge, Baha, Michael Lawson, my awesome homie Jared Klein and the roomies in the past... You all mean a lot to me!

IT HAS BEEN MY GREATEST PLEASURE TO KNOW YOU ALL!

Table of Contents

	Page
List of Tables	xiv
List of Figures	xv
CHAPTER 1: Importance of macromolecular structuring in polymer thin films	1
1.1 Motivation	1
1.2 Generic topics in polymer thin-films	3
1.2.1 Polymer thin-film stability	3
1.2.2 Block copolymers and their use as compatibilizers in thin-film stabilization	6
1.2.3 Core-shell polymer nanoparticles (CSPNs) in thin-films	12
References	16
CHAPTER 2: Autophobicity-driven surface segregation of core-shell polymer nanogel particles (CSNGs)	21
2.1 Motivation	21
2.2 General concepts on core-shell nanogel particles	22
2.3 Experimental	23
2.3.1 Materials	23
2.3.2 Particle synthesis and characterization	24
2.3.2.1 Divinyl benzene-core (DVB)/PMMA-arm particles (CSNGs)	24
2.3.2.2 PEGDMA-core/PS-arm particles (CSNG-Rs)	25
2.3.3 Thin-film preparation and characterization	25
2.4 Results and discussion	27
2.4.1 Autophobicity-driven segregation of CSNG	27
2.4.2 Time-dependence of the autophobicity-driven segregation of CSNG	34
2.4.3 Image analysis of CSNG	36
2.4.4 Electric field-driven segregation of CSNG	37
References	44
Appendix	48
Appendix A. Synthesis and characterization of CSNG-Rs	49
Chapter 3: Lateral structuring at immiscible polymer/polymer interfaces induced by aggregation and adsorption of core-shell polymer nanoparticles	52
3.1 Motivation	52
3.2 Experimental	53
3.2.1 Materials	53
3.2.2 Methods	55
3.3 Results and discussion	56
3.3.1 CSNG as stabilizers	56
3.3.2 Effect of CSNG concentration	61
3.3.3 Effect of PS homopolymer molecular weight	68

3.4 Summary.....	72
References.....	74
CHAPTER 4: Mean-field phase behavior of triblock copolymers varying in molecular asymmetry.....	
4.1 Introduction.....	76
4.2 Experimental.....	78
4.2.1 Materials.....	78
4.2.2 Methods.....	78
4.2.2.1 Rheological characterization.....	78
4.2.2.2 Mean-field phase behavior.....	79
4.3 Results and discussion.....	81
Acknowledgments.....	87
References.....	88
Appendix.....	92
Appendix A. Fortran algorithm of mean-field phase behavior.....	93
CHAPTER 5: Asymmetric block copolymers at immiscible polymer/polymer interfaces... 134	
5.1 Block copolymer architecture.....	134
5.2 Overview on block copolymer micelles and critical micelle concentration (CMC) ...	135
5.3 Motivation for this study.....	138
5.4 Experimental.....	140
5.4.1 Materials.....	140
5.4.2 Methods.....	142
5.4.2.1 (PS/SM)/PMMA bilayers.....	142
5.4.2.2 PS/(PMMA/SM) bilayers.....	143
5.4.2.3 PS/SM/PMMA and (PS/SM)/SM/PMMA trilayers on silicon substrates.....	144
5.4.2.4 Self-standing thin-films of (PS/SM) on Cu TEM grids.....	145
5.5. Results and discussion.....	146
5.5.1 (PS/SM)/PMMA bilayers.....	146
5.5.2 (PS/SM)/PMMA bilayers.....	152
5.5.3 Self-standing thin-films of (PS/SM) on Cu TEM grids.....	154
5.5.4 PS/SM/PMMA and (PS/SM)/SM/PMMA trilayers on silicon substrates.....	155
References.....	166
Appendix.....	169
Appendix A. CMC values via dry-brush theory.....	170
Appendix B. CMC values via self-consistent field theory (SCFT).....	173
Appendix C. Interfacial tension vs. diblock asymmetry and concentration in PS/SM/PMMA bilayers via Self-Consistent Field Theory.....	174
Chapter 6: Mixtures of asymmetric block copolymers at immiscible ps/pmms interfaces... 176	
6.1 Motivation.....	176
6.2 Experimental.....	179
6.2.1 Materials.....	179
6.2.2 Methods.....	179
6.3 Results and discussion.....	181
6.3.1 Equimass mixtures of PS ₅₀ -b-PMMA ₂₀ / PS ₂₀ -b-PMMA ₅₀	181

6.3.2 Mixtures of PS ₅₀ -b-PMMA ₁₀ / PS ₁₀ -b-PMMA ₅₀	183
Chapter 7: Conclusions and recommendations for future work	188
7.1 General Remarks	188
7.2 Conclusions.....	192
7.2.1 Thermal Response of PMMA-arm CSNGs	192
7.2.2 Nanoparticle Architecture on Dewetting Mechanism And Lateral Structuring: PS-arm vs. PMMA-arm CSNGs.....	194
7.2.3 Effect of Block Copolymer Nature and Architecture on Polymer Thin-Film Stability: Stability Induced by Mixing vs. Destabilization due to Micellization	196
7.2.4 Copolymer Mixtures in Thin-Films: Competition Between Interfacial Structuring vs. Micellization	197
7.3 Recommendations for Future Work	198
7.3.1 Core-Shell Nanoparticles.....	199
7.3.2 Block Copolymers	200

List of Tables

	Page
Chapter 3	
Table 3.1 Properties of CSNG-R(w). (“w” denotes the molecular weight in kg/mol).	53
Chapter 5	
Table 5.1 Molecular weight and the PDI values for the SM copolymers.	141
Table A5.1 Molecular weight and the PDI values for the SM copolymers.	172
Table A5.2 Molecular weight and the PDI values for the SM copolymers.	173

List of Figures

	Page
Chapter 1	
Figure 1.1. Wetting and dewetting behavior of two polymer films.	3
Figure 1.2. Two mechanisms of dewetting: (i) nucleation and growth (NG) (top row) and spinodal dewetting (SD) (middle and bottom rows) at various time intervals. The bottom scale marker signifies 30 μm	5
Figure 1.3. Mean-field representation of the equilibrium phase diagram for a bulk diblock copolymer system: (a) theoretical, (b) experimental.	6
Chapter 2	
Figure 2.1 Schematic illustration of CSNGs. Structural properties: gyration diameter ($D_g = 26$ nm), number of PMMA arms attached to the core ($\#_{\text{PMMA}} = 28$), molecular weight of each PMMA arm ($M_{\text{PMMA}} = 11$ kDa) and grafting density of the PMMA arms ($\sigma_{\text{PMMA}} = 0.013$ arms/ nm^2).	24
Figure 2.2 Schematic illustration of CSNG-R# particles (R# denotes the weight-average molecular weight. Structural properties: gyration diameter ($D_g = 13.1$ -14.5 nm), number of PS arms attached to the core ($\#_{\text{PMMA}} = 22$ -32), molecular weight of each PS arm ($M_{\text{PS}} = 11$ kDa) and grafting density of the PS arms ($\sigma_{\text{PMMA}} = 0.010$ -0.012 arms/ nm^2).	25
Figure 2.3 Schematic illustrations showing the distribution of CSNGs in (a) PMMA bottom layer and (b) the PS top layer in PS50/PMMA243 bilayer arrangements prior to annealing. Redistribution of the CSMG nanoparticles after annealing at 180°C is portrayed in (c), wherein the PS layer dewets into discrete islands. Irrespective of the starting point (a or b), the CSMG nanoparticles and their aggregates protrude from the PMMA surface under the PS islands, whereas the exposed PMMA surface remains relatively smooth.	27
Figure 2.4 Series of AFM height images showing the PMMA surface after different exposure conditions at 180°C: (a) complete dewetting of the PS capping layer after 80 h; formation, and subsequent solvent-removal, of PS islands after (b) 80 and (c) 20 h; and (d) further annealing of (b) without the PS capping layer for 40 h.	28
Figure 2.5 (a) AFM height image showing the PMMA surface after annealing for 6 h at 180°C. The dashed line marks the periphery where a dewetted PS island resided prior to	

selective dissolution, and the circle identifies several partially protruding CSMG nanoparticles that have begun to sink back into the PMMA matrix upon dewetting-induced surface exposure. A schematic series of top and side views are provided in (b) to illustrate this mechanism of surface energy-induced CSMG submersion as a function of annealing (PS dewetting) time. 30

Figure 2.6 Energy-filtered TEM images of CSMG-R nanoparticles acquired from (a) the interior of a thin PS film and (b, c) the interface between 216 kDa PS and 900 kDa PS after annealing at 180°C for 24 h. The PS homopolymer matrices and arms of the CSMG-R nanoparticles are selectively stained and the light features correspond to the unstained acrylic cores of the nanoparticles. The regions separated by dashed lines in (b) are discussed in the text. The circled feature in (a) and the arrow in (b) highlight examples of large nanoparticle aggregates. 33

Figure 2.7 AFM height images showing the time-dependence of CSNG aggregation on PMMA243 surface after PMMA243/CSNG/PS50 was annealed for (a) 1 h, (b) 3 h, (c) 6 h, (d) 9 h, (e) 12 h and (f) 84 h at 180°C. PS50 was selectively removed prior to AFM topography imaging. 35

Figure 2.8 Total number of particles in aggregates vs. annealing time. 37

Figure 2.9 Schematic illustration of the electric field experimental setup. 39

Figure 2.10 Optical microscopy images of (a) Au-coated glass surface, (b) PMMA/CSNG layer on Au electrode after floating, (c) PMMA/CSNG after on Au-electrode after 27 h at 180°C, and (d) PMMA/CSNG on Au, after 24 h electric field applied at 180°C. Scale marker is 50 microns. 41

Figure 2.11 AFM images of (a) PMMA/CSNG layer on Au electrode after floating, (b) PMMA/CSNG after on Au-electrode after 27 h at 180°C, (c) PMMA/CSNG (dewetted areas corresponding to cf. Fig. 2.9c) on Au after 24 h at 180°C electric field applied and (d) 3D image of the structuring in part c. Scale marker is 1 micron. 42

Chapter 3

Figure 3.1 Illustration of CSNG-R378. 54

Figure 3.2 Optical micrographs of (a) pure PS204, (b) PS204/CSNG-R378 as cast films on silicon wafers, (c) pure PS204 at 180°C for 80 h, and (d) PS204/CSNG-R378 at 180°C for 80 h. Scale marker is 20 microns. 57

Figure 3.3 48 nm thick pure CSNP-R378 at 180°C for 80 h on silicon wafer (a) optical micrograph at 20x with DIC optics, (b) by scanning electron microscopy in field emission mode, 5 kV at 100,000x.	58
Figure 3.4 Optical micrographs of (a) as-cast film of PS204/PMMA51 on silicon substrate (the inlet image is the surface topography scan showing a roughness value of 0.216 nm), (b) as-cast film of PS204/CSNG-R378/PMMA51 on silicon substrate, (c) PS204/CSNG-R378/PMMA51 bilayer at 180°C for 80 h (the inlet shows a PS layer dewetting from a PMMA substrate with the evidence of PS islands), and (d) PS204/CSNG-R378/PMMA51 bilayer at 180°C for 80 h after PMMA51 layer was selectively removed with acetic acid. ..	60
Figure 3.5 Optical micrographs of (a) PS204/CSNG-R263(1wt%)/PMMA51 at 190°C for 2 h, and (b) PS204/CSNG-R263(10 wt%)/PMMA51 bilayer at 190°C for 4 h, (c) (b) PS204/CSNG-R378 (10 wt%)/PMMA51 at 190°C for 16 h and (d) AFM of topography and 3D views of the features displayed in part (c).	63
Figure 3.6 Optical micrographs of (a) PS204/CSNG-R263(15wt%)/PMMA51 at 180°C for 39 h and (b) PMMA51-free areas of the PS204/CSNG-R263 substrate at 180°C for 39 h and the sample was treated in acetic acid for 4.5 h.	64
Figure 3.7 Optical micrographs of PS204/CSNG-R263(15wt%)/PMMA51 taken at 50x magnification with RGB optics. The sample was treated at 180°C for 39 h, and, then was immersed in acetic acid for 27 h to remove the PMMA51 top layer. (d) AFM of topography and 3D views of the tentacle-like structures displayed in part (c).	65
Figure 3.8 Optical micrographs of PS204/CSNG-R378 (15wt%)/PMMA51 at 190°C for 16 h taken at 20x magnification with DIC optics, and, then was immersed in acetic acid for (b) 1 h and (c) 27 h, to remove the PMMA51 top layer. AFM topography imaging was performed on the tentacle-like structures as shown in part (d).	67
Figure 3.9 Optical micrographs of PS204/CSNG-R378(20wt%)/PMMA51 at 180°C for 80 h taken at 20x magnification with DIC optics, and, then (b) was immersed in acetic acid for 24 h to remove the PMMA51 top layer.	68
Figure 3.10 Optical micrographs of PMMA51 dewetting from PS879 at 180°C for 80 h taken at 20x magnification with DIC optics, and, then (b) was immersed in acetic acid for 4 h to remove the PMMA51 top layer.	69
Figure 3.11 Optical micrograph of PS879/CSNG-R263(1wt%)/PMMA51 bilayer at 190°C for 2 h.	70

Figure 3.12 Optical micrographs of PS879/CSNG-R378/PMMA51: (a) 1wt% CSNG-R378 loading at 190°C for 2 h, (b) 5wt% CSNG-R378 loading at 190°C for 3.5 h (c) 15wt% CSNG-R378 loading at 190°C for 40 h. 72

Chapter 4

Figure 4.1. Dependence of the order-disorder transition temperature (T_{ODT}) measured by dynamic rheology on the mass of the growing A_2 endblock (M_{A_2}) in the 9-46- A_2 (●) and 9-17- A_2 (○) triblock copolymer series (see the text for details). The solid lines connect the data, and the dotted vertical lines identify the conditions corresponding to molecularly symmetric triblock copolymers wherein $M_{A_1} = M_{A_2}$ 81

Figure 4.2. Values of $(\chi N)_{ODT}$ presented as a function of molecular asymmetry (t) as predicted from the mean-field theory of Mayes and Olvera de la Cruz^{30,31} for two asymmetric triblock copolymer designs: (a) fixed molecular composition (f_A) and (b) variable molecular composition. Corresponding values of f_A are listed in (a), and the two copolymer systems under investigation (see the text for details) are labeled in (b). 83

Figure 4.3. Values of T_{ODT} for the 9-46- A_2 (●) and 9-17- A_2 (○) triblock copolymer series normalized with respect to T_{ODT} for the parent diblock copolymer ($\tau = 1$) in each series and presented as functions of (a) molecular asymmetry (t) and (b) molecular composition (f_A). The solid lines are mean-field theory predictions used in conjunction with $c(T)$ reported by Lodge et al.³⁴ The dotted lines identify the conditions corresponding to $\tau = 0.5$ (a) and $T_{ODT,r} = 1$ (a and b). 84

Figure 4.4 Dependence of T_{ODT} on τ for the 9-46- A_2 (●) and 9-17- A_2 (○) triblock copolymer series. The solid lines represent fits of the mean-field predictions displayed in Fig. 2.2b to both datasets. The inset is a schematic illustration depicting the chain conformations associated with the transformation of an A_1B diblock copolymer (a) to an A_1BA_2 triblock copolymer (b-e). A relatively short A_2 block initially remains mixed with the B midblock (b). As the length of the A_2 block is further increased, it microphase-separates to form a bidisperse brush with the A_1 block (c). When $\tau = 1/2$, the triblock copolymer becomes molecularly symmetric in which case the lengths of the A_1 and A_2 endblocks are identical (d). A further increase in the length of the A_2 block ($\tau < 1/2$) is accompanied by a bidisperse brush and an order-disorder transition governed by the A_2 block (e). 85

Chapter 5

Figure 5.1 Copolymer-induced changes in dewetting mechanism presented with the macroscopic dewetting rate (dD/dt) and AFM height images (5 mm x 5 mm) of the

polymer/polymer interface after selective dissolution of the top layer. The different symbols correspond to results from different analyses of the data.²⁰ 135

Figure 5.2 Illustration of an AB diblock copolymer molecules (A: red , B: blue) in an A-selective solvent. At concentrations much lower than the CMC (top), copolymer molecules exhibit single chains, and at concentrations that are higher than the CMC (bottom), copolymer molecules tend to form micellar structures and minimize the interactions between the hydrophobic core and the surrounding solvent molecules. 136

Figure 5.3 Cross-section illustration of a dewetting hole in the presence of free micelles, surface micelles and interfacial copolymer patches on the PS/PMMA double-layered assemblies investigated. 139

Figure 5.4 Illustration of block asymmetry in SM copolymers used in the study (PS block in red, PMMA block in blue. 140

Figure 5.5 Illustrative representation laminate systems: Bilayers: (PS/SM)/PMMA (top left) and PS/(PMMA/SM) (bottom left). Trilayers: (PS/SM)/SM/PMMA (top right) and PS/SM/PMMA (bottom right). 142

Figure 5.6 Linear dewetting rate of PS/SM on PMMA243 at 180°C as a function of SM concentration: (a) PS30, (b) PS5, (c) PS216. 148

Figure 5.7 Illustration of aggregates formed by PS₁₀-*b*-PMMA₅₀ in PS30 on PMMA243 (top). Upon annealing, micelle aggregates and free SM molecules migrate to the PS/PMMA interface (bottom). PMMA blocks of the SM copolymer exhibit autophobic behavior with high molecular weight PMMA243 homopolymer chains; they can, however, be partially adsorbed on the PMMA243 surface, which might result in an increase the interfacial area between PS30/PMMA243. 150

Figure 5.8 Representation of SM micelles segregating from PS30 and not having sufficient time to break and adsorbed at the interface. PS30 layer dewets much faster than the micelles travelling to the interface, and not being able to break fast enough to pin the PS layer on PMMA243. 151

Figure 5.9 Linear dewetting rate of PS50 on PMMA243/SM at 180°C as a function of SM concentration for four different copolymers. 152

Figure 5.10 Representation of SM micelles segregating from PMMA243 and having sufficient time to break and adsorbed at the interface, thus, stabilizing the top PS layer. ... 154

Figure 5.11 60nm-thick self-standing films of PS50 and PS50/PS₁₀-*b*-PMMA₅₀ (0.15 wt%) on Cu TEM grid with 1mm grid size. The grids are not touching the graphite plates; they are

standing between two glass pieces on the corners. The middle hole where the film is located is freely standing, having an air/air interface on both sides. 154

Figure 5.12 Linear dewetting rate of PS30/PS₁₀-*b*-PMMA₅₀ on PMMA243 at 180°C as a function of PS₁₀-*b*-PMMA₅₀ layer film thickness: (a) copolymer-free PS30 and (b) 0.25wt% copolymer-added PS30. Grafting densities are represented as a function of midlayer film thickness. Mushroom-to-brush crossover for the PS block is at $\Sigma_{PS10} = 1$ 157

Figure 5.13 Linear dewetting rate of PS30/PS₅₀-*b*-PMMA₁₀ on PMMA243 at 180°C as a function of PS₅₀-*b*-PMMA₁₀ layer film thickness: (a) copolymer-free PS30 and (b) 0.25wt% copolymer-added PS30. Grafting densities are represented as a function of midlayer film thickness. 161

Figure 5.14 (Left) Linear dewetting rate of PS30/PS₅₀-*b*-PMMA₅₄ on PMMA243 at 180°C as a function of PS₅₀-*b*-PMMA₅₄ layer film thickness: (a) copolymer-free PS30 and (b) 0.25wt% copolymer-added PS30. Grafting densities are represented as a function of midlayer film thickness. 162

Figure A5.1 Typical density profile for PS30/PS₅₀-*b*-PMMA₅₄/PMMA243. 174

Chapter 6

Figure 6.1 Linear dewetting rates of PS50/SM on PMMA243 at 180°C as a function of SM copolymer concentration. One symmetric and three asymmetric copolymers are embedded in PS. 177

Figure 6.2 Linear dewetting rate for PS50 containing equimass PS₂₀-*b*-PMMA₅₀ and PS₅₀-*b*-PMMA₂₀ mixtures on PMMA243 at 180°C as a function of copolymer concentration. 181

Figure 6.3 Linear dewetting rate for PS50 containing PS₁₀-*b*-PMMA₅₀ and PS₅₀-*b*-PMMA₁₀ mixtures on PMMA243 at 180°C as a function of copolymer concentration. The composition of PS₁₀-*b*-PMMA₅₀ was varied from 50wt% (yielding an equimass mixture, 50/50) to 99wt% (99/1). The composition of the PS₅₀-*b*-PMMA₁₀ copolymer was varied accordingly. The grey bar represents the concentration regime, beyond which the stability is governed by PS₅₀-*b*-PMMA₁₀. The cartoon on the top left is an illustration of PS₁₀-*b*-PMMA₅₀ micelles at the interface, and the one on the bottom right side represents the stability induced by PS₅₀-*b*-PMMA₁₀ chains. 184

Figure 6.4 Linear dewetting rate for PS₁₀-*b*-PMMA₅₀ and PS₅₀-*b*-PMMA₁₀ mixtures containing PS50 on PMMA243 at 180°C as a function of PS₅₀-*b*-PMMA₁₀ copolymer concentration. PS50-*b*-PMMA10 copolymer is denoted as 50-10 (w%) for simplicity and “w” represents the weight composition of this copolymer in the mixture. 185

CHAPTER 1: Importance of macromolecular structuring in polymer thin films

1.1 Motivation

Understanding nanoscale segregation of macromolecular surfactants, such as block and graft copolymers, to polymer/polymer interfaces is of vital importance in achieving compatibilization in bulk polymer blends and stability in thin films. Compatibilization results in the formation of smaller dispersions due to lower radius of curvature, yielding reduced interfacial tension, on the other hand, a flat surface is desirable for thin-film stabilization. A limiting factor encountered commonly in the preparation of compatible polymer blends via conventional polymer processing (e.g., melt extrusion) is self-organization of the copolymer molecules, which serves to deplete the reservoir of molecules available for interfacial modification and, hence, effective compatibilization. While this effect may be expected intuitively to be less pronounced in laminates composed of molecularly-thin films of two immiscible macromolecules, our results of such laminates in the melt at elevated temperatures have demonstrated that copolymer micellization occurs likewise within one of the polymer layers. Unexpected development of substantial copolymer structuring occurring laterally along the polymer/polymer interface has also been observed during the course of this study. While copolymer ordering along polymer/polymer interfaces has been reported previously at relatively high copolymer concentrations in ternary copolymer/polymer/polymer blends, the conventional picture of polymer/polymer interfaces at relatively low copolymer concentrations neglects the role of lateral interfacial structuring, which takes place to a nontrivial extent in the molten laminates that we have recently

investigated. These two competitive events, i.e., copolymer self-organization and interfacial structuring, affect the stability of the thin-film laminates, which is of general and crucial consideration in the development of, for instance, advanced coatings. In such confined systems, molecular self-organization may be transient, resulting in metastable nanostructural elements that dissolve as the global free energy of the system seeks a minimum. For comparison, we have likewise examined the interfacial segregation of core-shell polymeric nanoparticles that mimic effectively block copolymer micelles. Unlike copolymer micelles, however, the core of the purposefully designed nanoparticles is chemically cross-linked and cannot dissolve in homopolymers in which they are incorporated in this study. The interplay between the surface and interfacial tension force these nanoparticles migrate selectively and reversibly and reside along a polymer/polymer interface. Planar and topographical imaging have also shown nanoparticle aggregation along the interface. These results *(i)* raise fundamental questions regarding the competition between (supra)molecular self-organization and interfacial modification in confined thin-film laminates, and *(ii)* open new avenues to designer polymer laminates on polymer substrates for advanced coating, templating and responsive technologies.

1.2 Generic topics in polymer thin-films

1.2.1 Polymer thin-film stability

The stability of polymer thin films is critical to the development of advanced protective coatings and defect-free multilayer assemblies, in which case the molecular-scale processes responsible for film destabilization must be fully understood.

When a liquid is placed upon a solid, it can remain stable and "wet" the substrate or it can alternatively become unstable and "dewet" from the substrate, depending on the surface tension of the liquid and the interfacial tension between the liquid and the substrate. These scenarios are depicted in Fig. 1.1.

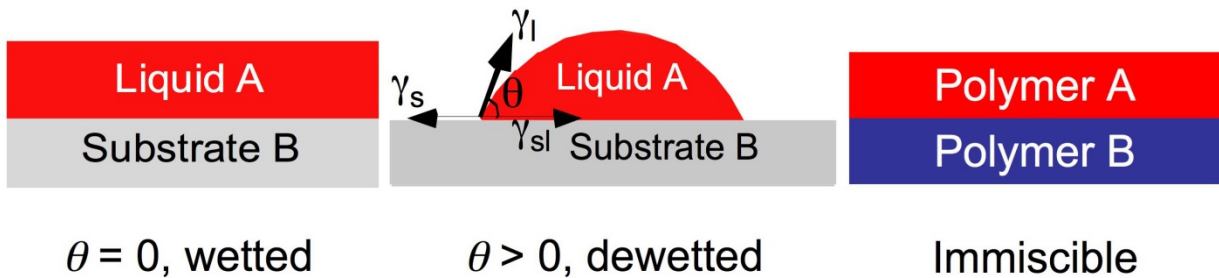


Figure 1.1. Wetting and dewetting behavior of two polymer films

Since we intend to investigate the dewetting of one polymer thin film from a polymer substrate, the degree to which the polymers interact must be considered. Polymer pairs are generally immiscible for two reasons: endothermic mixing and negligibly low entropy of mixing. The two polymers of interest here, i.e., polystyrene (PS) and poly(methyl methacrylate (PMMA), are inherently immiscible at the molecular weights to be used. At

temperatures higher than the glass transition temperatures of the polymer layers ($T > T_g$), both layers are liquid. If the melt viscosity of polymer B is significantly higher than that of polymer A ($\eta_B \gg \eta_A$), polymer B behaves solid-like relative to A and can be treated as such, according to the results of Brochard-Wyart *et al.*¹ The tendency for polymer A to dewet from substrate B is dictated by the spreading parameter (S), defined as

$$S = \gamma_{BAB} (\gamma_A + \gamma_{AB}) \quad , \quad (1.1)$$

where γ_A and γ_B denote the surface tensions of A and B, respectively, and γ_{AB} is the interfacial tension at the A/B interface. When $S > 0$, layer A remains stable and does not dewet. If $S < 0$, however, layer A becomes unstable, ruptures and dewets from substrate B. Dewetting occurs conventionally via the mechanism of nucleation and growth (NG), wherein discrete rupture sites develop in the dewetting film and grow as circular holes with time. At long times (t), these holes (of diameter D) impinge and the resultant islands are referred to as sessile droplets.² Hole growth typically proceeds without interfacial slip, in which case $D \sim t$. If interfacial slip governs hole growth, $D \sim t^{2/3}$. Partial slip may also be encountered in dewetting by NG. Dewetting may alternatively occur by another mechanism referred to as spinodal dewetting (SD), which appear similar to what is observed during spinodal decomposition during phase separation of two polymers in the bulk. In this case, discrete holes are replaced by surface modulations, or fluctuations, due to thermally induced capillary waves.³⁻¹⁰ These waves amplify with time and become the dominant mechanism of dewetting in very thin polymer films. Examples of these two modes of dewetting are displayed for illustrative purposes in Fig. 1.2.

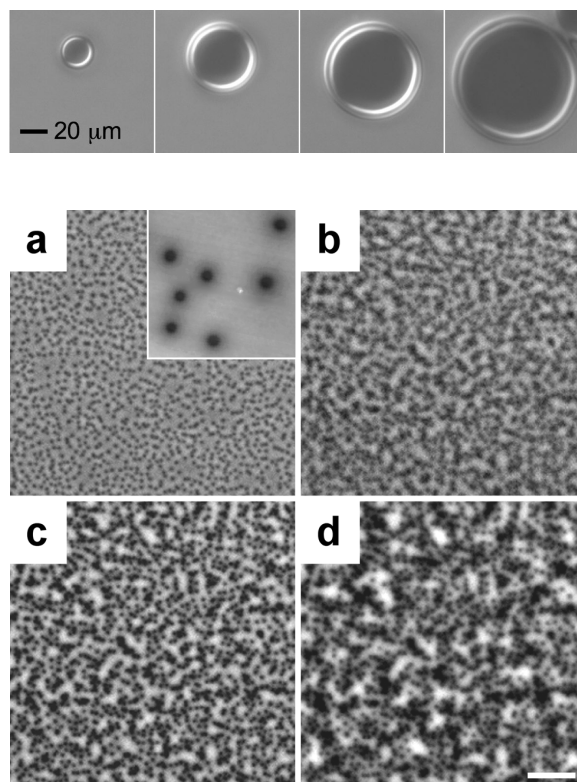


Figure 1.2. Two mechanisms of dewetting: (i) nucleation and growth (NG) (top row) and spinodal dewetting (SD) (middle and bottom rows) at various time intervals. The bottom scale marker signifies 30 μm.

Recent studies¹¹ have demonstrated that the addition of a block copolymer to an immiscible thin polymer/polymer interface reduces the rate at which dewetting proceeds. This constitutes an important consideration in that it (i) provides a reliable method to stabilize thin films for various technologies and (ii) marries the general concept of polymer/polymer compatibilization with stabilization of thin films arranged in alternating layers. As little as a few percent added diblock copolymer can reduce the measured dewetting rate (i.e., the time rate of change of hole diameter, dD/dt) by an order of

magnitude. This result is not entirely surprising since the intuitive limiting case requires that, at a sufficiently high copolymer concentration, the top film must be fully stabilized.

1.2.2 Block copolymers and their use as compatibilizers in thin-film stabilization

Block copolymers represent a fascinating class of self-assembling materials.¹²⁻²¹ They provide a large source of possible nanostructures differing in geometry that can be used to fabricate functionalized materials from neat copolymer melts, as well as from mixtures with a homopolymer (or a solvent), as the starting point.^{17,20,22-26}

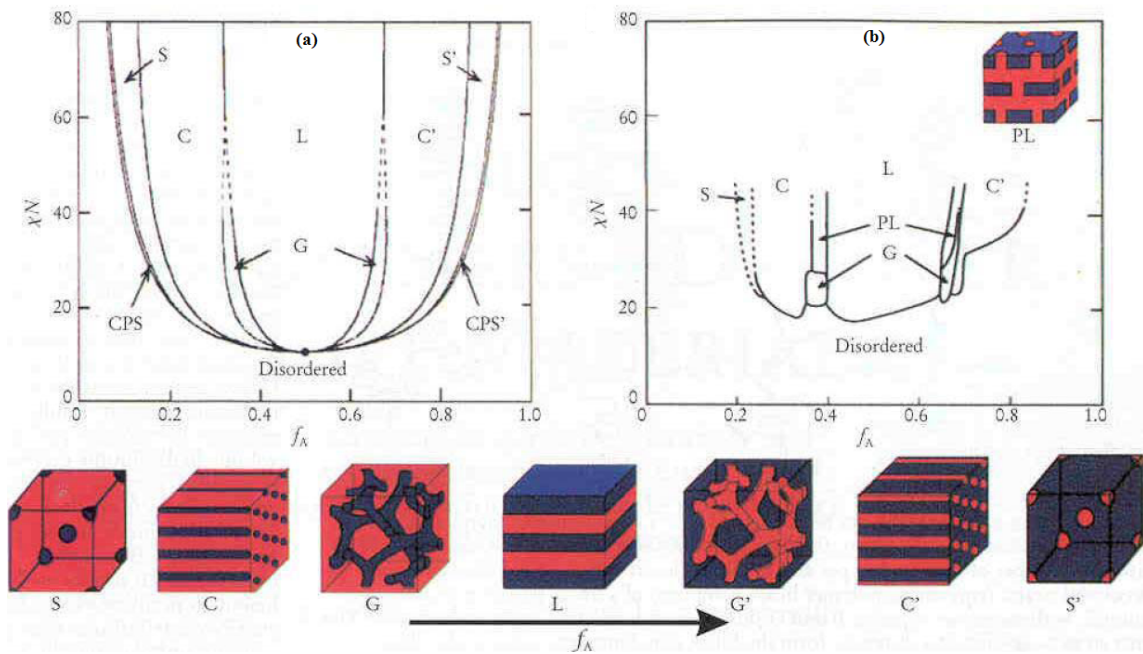


Figure 1.3. Mean-field representation of the equilibrium phase diagram for a bulk diblock copolymer system: (a) theoretical, (b) experimental.¹²

Block copolymers have quickly drawn due to their variety of composition-tunable properties.^{12-16,19,21-23,27-34} The simplest block copolymer motif consists of two immiscible

homopolymers covalently bonded to form a diblock copolymer. While homopolymers commonly undergo phase separation at macroscopic length scales, block copolymers self-assemble spontaneously into a variety of ordered morphologies due to the restriction arising from the covalent linkage. Commonly encountered morphologies are depicted in Fig. 1.3 and include spheres arranged on a body-or face-centered cubic lattice, cylinders arranged on a hexagonal lattice, bicontinuous channels and alternating lamellae.^{12,18,19} Other aperiodic morphologies including sponge and network morphologies have likewise been reported,³⁵ but are not considered further here. The important parameters to be considered in the design of block copolymer molecules (cf. Fig. 1.3) are (i) the molecular composition (expressed in terms of the number, or volume, fraction of one of the blocks, f_A) and the interblock incompatibility parameter (χN).

One strategy developed to increase the versatility of block copolymers and explore systematically differences between diblock and triblock copolymers is to introduce progressively a third block to a diblock copolymer, thereby forming a triblock copolymer. Incorporation of a chemically dissimilar third block results in an ABC triblock copolymer, which can greatly extend the phase behavior by varying the relative block lengths and thus, incompatibilities.^{14,18} Midblock bridging and network formation in ABA triblock copolymer systems investigated by experimental³⁶ and theoretical³⁷ means have thus far focused exclusively on *molecularly symmetric* copolymers, wherein the two endblocks are the same length. To identify the conditions responsible for midblock bridging, we have explored²⁹ the transformation from an A_1B diblock copolymer to *molecularly asymmetric* A_1BA_2 triblock

copolymers varying in asymmetry as the A_2 endblock is grown via living anionic polymerization. The result of this specific study is further discussed in Chapter 4.

The morphological design rules described above are only applicable to bulk systems wherein edge or surface effects are completely neglected. Geometric confinement can affect profoundly the manner by which block copolymer molecules distribute and organize, as demonstrated both experimentally and theoretically. Geometric confinement, such as that encountered in molecularly thin films, can also affect the equilibrium morphologies of block copolymers or copolymer/homopolymer blends, resulting in markedly different morphologies in thin films compared to those in the bulk.^{24-26,38,39}

The dynamic field-theory results of Fraaije and co-workers reveal that the morphologies of a microphase-separated triblock copolymer system are exquisitely sensitive to thickness in molecularly thin films. As Russell and co-workers⁴⁰ have shown, environmental factors such as the presence of a solvent vapor can likewise have a pronounced effect on the morphologies of block copolymer thin films. This complication is exacerbated greatly in a binary blend composed of a copolymer in a homopolymer matrix, since either species can selectively migrate to the film surface or the polymer/substrate interface.^{11,26,34} Of particular interest here is the previous study by Wei *et al.*,^{34,41} which confirmed that micelles varying in both size and extent of aggregation develop in thin homopolymer films as the films become unstable and dewet from an immiscible polymer substrate. In a comparable system, Zhu *et al.*⁴² propose that the distribution of block copolymer molecules depends on the balance between the chemical potential of the copolymer to locate at the interface (μ_I) relative to that needed to form micelles (μ_M).

According to their self-consistent field theory (SCFT) predictions, the magnitude of μ_M is anticipated to increase with decreasing film thickness due to the increased entropic penalty needed to squeeze copolymer molecules into smaller aggregates. As a result, copolymer migration to the interface becomes more favorable relative to micellization, which is experimentally observed. While the SCFT approach is not ideally suited for the case of a dynamically-evolving system, such as a polymer thin film undergoing dewetting, it provides guidance into the physics of the present system of interest. Zhu *et al.*⁴² report detecting no PS-*b*-PMMA micelles in apparently stable PS films measuring ≈ 100 nm thick at various copolymer concentrations (above the cmc), whereas Wei *et al.*^{11,26,34} provide evidence to the contrary in dewetting films only ≈ 60 nm thick. Thus, this discrepancy illustrates that such complex systems warrant further systematic investigation.

In the presence of a parent homopolymer, another parameter that becomes critically important is the molecular weight disparity (a) between the homopolymer and the host block of the copolymer ($a = M_{hA}/M_A$).^{29,35,43} If the homopolymer molecular weight is much larger, for example, than that of the corresponding copolymer block, the copolymer brush formed once the copolymer molecules self-organize will remain dry. This chain-penetration effect dictates the extent to which the homopolymer can be incorporated within the copolymer matrix in copolymer-rich blends, as well as the size and shape of copolymer dispersions within the homopolymer matrix in homopolymer-rich blends.

If a block copolymer is distributed between the parent homopolymers, it acts as a surfactant and emulsifies the homopolymers by reducing the interfacial tension.³² In this scenario, the copolymer molecules locate along the interface formed by the macrophase-

separated homopolymers, which generally tend to be thermodynamically immiscible due to a combination of endothermic mixing and a near-negligible entropy of mixing. Bulk polymer processing exposes such ternary systems to high shear fields that permit migration of the copolymer molecules to the dynamically evolving and curved polymer/polymer interface, with the result that the degree of dispersion of one homopolymer in a matrix of the other is vastly improved.²¹ While this strategy has long been adopted in the polymer industry, it is not necessarily *downward* scalable, that is, scalable to nano- or molecular-scale dimensions when confinement effects can no longer be ignored. As an example, we consider the dewetting of a thin polymer film from a flat, immiscible polymer substrate. Incorporation of a block copolymer into the top layer results in a competition for the copolymer molecules to (1) form micelles (energetically favored at concentrations above the *cmc* in the thin film, which may differ from that of the bulk) and (2) stabilize the polymer/polymer interface. Such nanoscale compatibilization is of tremendous technological interest due to the general importance of multilayer polymer films.^{11,17,22,23,26,34}

Block copolymer micelles are thermodynamically stable nanostructures that are capable of molecular reorganization under changing environmental conditions. Changing temperature, for instance, can cause spherical micelles of block copolymers to transform into worm-like (cylindrical) micelles or even nanotubes.⁴⁴⁻⁴⁶ If a micelle contacts a surface, it may break, allowing the copolymer molecules to adopt a more thermodynamically-favored arrangement along the surface. In some cases, such rearrangement may lead to more highly organized morphologies, such as lamellae.³⁵ This "transient" nature of micelles makes it

difficult to assess the role of discrete macromolecular assemblies on morphological development near surfaces and interfaces.

To investigate this phenomenon in detail, we shall use block copolymers composed of poly(styrene-*b*-methyl methacrylate) (PS-*b*-PMMA). Copolymers of this type are known to microphase-separate at experimentally accessible temperatures due to their intrinsically high incompatibility, which is given by the product of the Flory-Huggins interaction parameter (χ) and the number of statistical units along the backbone (N).^{29,30,35,43} Since the glass transition temperatures (T_g) are comparable (100-120°C), experiments will be designed so that both blocks are either molten ($T > T_g$) or glassy ($T < T_g$), which will be important for ex-situ analysis of dynamic processes such as dewetting and molecular self-assembly. Of equal importance, the work proposed here will serve to extend the previous studies^{11,26,34,41} in this vein of research, thereby allowing us to develop a big picture of the multiply occurring phenomena within complex systems composed of a dewetting polymer thin film containing a self-organizing macromolecular species. Thus far, only small parts of this picture have been adequately elucidated, and the area is certainly fertile for further investigative study. System parameters such as film thickness, as well as copolymer composition, architecture, architecture and molecular weight, must be examined thoroughly for accurate and physically meaningful design rules can be established for such systems. It is further anticipated that such rules may benefit bulk compatibilization efforts by promoting an improved understanding of molecular processes that occur within close proximity to developing polymer/polymer interfaces.

1.2.3 Core-shell polymer nanoparticles (CSPNs) in thin-films

An alternative to block copolymer micelles are core-shell polymer nanoparticles (CSPNs) with unique 3D structures, which can be imagined as branched macromolecules.⁵¹ CSPNs generally consist of an organic (A) core surrounded by a dense brush of chemically dissimilar (B) arms⁵² and are of technological interest due to their tailorable chemistry and unique physico-chemical properties.⁵⁵ The desired applications of these particles commonly vary from personal care products to drug delivery vehicles.⁴⁷⁻⁵²

If the B shell is cross-linked chemically, the A core of such nanoparticles can be removed selectively and subsequently used as a hollow compartment for encapsulation.^{53,54} Such particles consist commonly of chemically cross-linked hydrophilic chains that can swell to tunable extents in an aqueous environment. In this regard, they possess many of the stimuli-responsive characteristics (responsive to external stimuli factors as temperature,^{53,54} pH,^{55,56} ionic strength⁵⁴ and solvency⁵⁶) of their hydrogel analogs⁵⁷.

The nanoparticles of interest in this work must, however, resemble chemically the PS-*b*-PMMA block copolymers described previously if similarities and differences are to be established across the two material platforms. CSPNs with two different chemistries have been synthesized for this study. The initial nanoparticles possessed a cross-linked divinylbenzene (DVB) core and PMMA arms via the “arms-first” route by atom transfer radical polymerization approach.^{34,41} The diameter of these particles is ≈ 30 nm, which makes them comparable in size to the scale of conventional block copolymer micelles.

A previous study^{34,41} has demonstrated that addition of these CSPNs to the afore-described dewetting films affords very little improvement in terms of film stability. An unexpected reported in that study suggests that the CSPNs are not permitted to enter the PMMA substrate due to autophobicity, which refers to entropically-driven phase separation of chemically identical species. This non-intuitive phenomenon arises when a densely packed arrangement of grafted polymer chains along a surface (a "brush") prevents free-floating chains of the same type to penetrate and "wet" the brush.³⁴ Instead, the brush remains "dry" and mixing between grafted and free chains is thereby precluded. In this scenario, phase separation of the constituent species may proceed due exclusively to entropic considerations. Autophobic phase separation between the CSPNs possessing a PMMA shell and the PMMA substrate results in surface enrichment of CSPNs and has been demonstrated³⁴ in the limit when the surface tension³⁴ of the PMMA is sufficiently reduced. This reduction is achieved conveniently by adding a sacrificial PS homopolymer layer on top of the PMMA during high-temperature annealing and converting the governing thermodynamic influence from surface tension (for pure PMMA) to interfacial tension (between PMMA and the sacrificial layer). Such surface enrichment has been reproduced and expanded to discern the robustness and applicability of this approach as a means to tunable surface modification. It is important to recognize that this effect could not be ascertained from the block copolymer systems described previously since conventional copolymer micelles would most likely be partially wetted by the PMMA, thereby avoiding an autophobic response. In addition, they would break as they reached the PMMA surface unless their cores were cross-linked.

Inverted CSP nanoparticles with PS arms varying in size and a chemically cross-linked acrylic core have likewise been prepared for this project. The observation that these nanoparticles can extend through a polymer/polymer interface and then submerge below an exposed polymer surface upon thermal treatment demonstrates that the nanoparticles can be responsive to their environmental conditions. Recently, we have explored a variety of systems to obtain a better understanding of how these nanoparticles behave in thin-film polymer laminates. The details of such nanoparticle-added PS/PMMA laminates, including the synthesis procedure (cf. Appendix 3A) are discussed further in Chapters 2 and 3.

In this dissertation, we intend to develop a deeper molecular-level understanding of how the parameters such as copolymer/nanoparticle concentration, copolymer molecular weight, composition, layer concentration, and layer thickness promote lateral interfacial structuring at immiscible polymer/polymer interfaces due to copolymer/nanoparticle segregation. Thus, this Ph.D. Thesis is divided into the following areas and serves the purpose of understanding:

1. Time-temperature conditions that favor the autophobically-driven surface enrichment of CSPNs under different levels of interfacial tension,
2. Migration of discrete nanostructures (CSPNs) to polymer/polymer interfaces where they can form lateral aggregates and form tentacle-like structures at the interface,
3. The transformation from a (A_1B) diblock copolymer to an (A_1BA_2) triblock copolymers varying in molecular asymmetry and its effect on phase behavior predicted by mean-field theory,

4. The self-assembly of diblock copolymers of various compositions at interfaces between two immiscible homopolymers and how lateral interfacial structuring develops. Our results demonstrate that such structuring can be highly heterogeneous and the reason behind the adverse thin-film stability observed. The time-dependent in-plane structure variations of copolymer molecules along the interface experimental evidence of discrete lateral interfacial structuring.

References

1. Redon, C.; Brochard-Wyart, F.; Rondelez, F. Dynamics of Dewetting. *Physical Review Letters* **66**, 715 (1991).
2. Reiter, G. Dewetting of Thin Polymer Films. *Physical Review Letters* **68**, 75-78 (1992).
3. Sferazza, M. ; Xiao, C.; Jones, R.A.L.; Bucknall, D.G.; Webster, J.; Penfold, J. Evidence for Capillary Waves at Immiscible Polymer/Polymer Interfaces. *Physical Review Letters* **78**, 3693 (1997).
4. Limary, R.; Green, P.F. Hierarchical Pattern Formation in Thin Film Diblock Copolymers above the Order-Disorder Transition Temperature. *Macromolecules* **32**, 8167 (1999).
5. Sferazza, M.; Heppenstall-Butler, M.; Cubitt, R.; Bucknall, D.; Webster, J.; Jones, R.A.L. Interfacial Instability Driven by Dispersive Forces: The Early Stages of Spinodal Dewetting of a Thin Polymer Film on a Polymer Substrate. *Physical Review Letters* **81**, 5173–5176 (1998).
6. Xie, R.; Karim, A.; Douglas, J.F.; Han, C.C.; Weiss, R.A. Spinodal Dewetting of Thin Polymer Films. *Physical Review Letters* **81**, 1251-1254 (1998).
7. Sharma, A.; Khanna, R. Pattern Formation in Unstable Thin Liquid Films. *Physical Review Letters* **81**, 3463 (1998).
8. Herminghaus, S.; Jacobs, K.; Mecke, K.; Bischof, J.; Fery, A.; Ibn-Elhaj, M.; Schlagowski, S. Spinodal Dewetting in Liquid Crystal and Liquid Metal Films. *Science* **282**, 916 (1999).
9. Segalman, R.A.; Green, P.F. Dynamics of rims and the onset of spinodal dewetting at liquid/liquid interfaces. *Macromolecules* **32**, 801 (1999).
10. Bollinne, C.; Cuenot, S.; Nysten, B.; Jonas, A.M. Spinodal-like Dewetting of Thermodynamically-Stable Thin Polymer Films. *Eur. Phys. J. E* **12**, 389 (2003).
11. Wei, B.; Lam, P.G.; Braunfeld, M.; Agard, D.A.; Genzer, J; Spontak, R.J. Tunable Instability Mechanisms of Polymer Thin Films by Molecular Self-Assembly. *Langmuir* **22**, 8642-8645 (2006).

12. Bates, F.S.; Fredrickson, G.H. Block Copolymers - Designer Soft Materials. *Physics Today* **52**, 32-38 (1999).
13. Lodge, T.P. Block Copolymers: Past Successes and Future Challenges. *Macromol. Chem. Phys.* **204**, 265 (2003).
14. Hamley, I.W. *Block Copolymers in Solution: Fundamentals and Applications* (John Wiley & Sons, 2005).
15. *Block Copolymers I* (ed. Abertz, V.) (Springer, 2005).
16. *Block Copolymers II* (ed. Abertz, V.) (Springer, 2005).
17. Albrecht, T.T.; Steiner, R.; DeRouchey, J.; Stafford, C.M.; Huang, E.; Bal, M., Tuominen, M.; Hawker, C.J., Russell, T.P. Nanoscopic Templates from Oriented Block Copolymer Films. *Adv. Mater.* **12**, 787-791 (2000).
18. Bates, F.S.; Fredrickson, G.H. Block Copolymer Thermodynamics: Theory and Experiment. *Annu. Rev. Phys. Chem.* **41**, 525-557 (1990).
19. Fredrickson, G.H.; Bates, F.S. Dynamics of Block Copolymers: Theory and Experiment. *Annu. Rev. Mater. Res.* **26**, 501-550 (1996).
20. Parka, C.; Yoonb, J.; Thomas, E.L. Enabling Nanotechnology With Self-Assembled Block Copolymer Patterns. **44**, 6725-6760 (2003).
21. Ruzette, A.V.; Leibler, L. Block Copolymers in Tomorrow's Plastics. *Nature Materials* **4**, 19-31 (2005).
22. Cheng, J.Y.; Mayes, A.M.; Ross, C.A. Nanostructure Engineering by Templated Self-Assembly of Block Copolymers. *Nature Materials* **3**, 823 (2004).
23. Lazzari, M.; López-Quintela, M.A. Block Copolymers as a Tool for Nanomaterial Fabrication. *Adv. Mater.* **15**, 1583-1594 (2003).
24. Jeong, U.; Ryu, D.Y.; Kho, D.H.; Kim, J.K.; Goldbach, J.T.; Kim, D.H.; Russell, T.P. Enhancement in the Orientation of the Microdomain in Block Copolymer Thin Films upon the Addition of Homopolymer. *Adv. Mater.* **16**, 533 (2004).
25. Liu, Y.; Rafailovich, M.H.; Sokolov, J.; Schwarz, S.A.; Zhong, X.; Eisenberg, A.; Kramer, E.J.; Sauer, B.B.; Satija, S. Wetting Behavior of Homopolymer Films on Chemically Similar Block Copolymer Surfaces. *Physical Review Letters* **73**, 440-445 (1994).

26. Wei, B.; Genzer, J.; Spontak, R.J. Dewetting Behavior of a Block Copolymer/Homopolymer Thin Film on an Immiscible Homopolymer Substrate. *Langmuir* **20**, 8659-8667 (2004).
27. Bernard, B.; Brown, H.R.; Hawker, C.J.; Kellock, A.J.; Russell, T.P. Adhesion of Polymer Interfaces Reinforced with Random and Diblock Copolymers as a Function of Geometry. *Macromolecules* **32**, 6254-6260 (1999).
28. Folkes, M.J. *Processing, Structure and Properties of Block Copolymers* (Elsevier Applied Science Publishers, 1985).
29. Hamersky, M.W.; Smith, S.D.; Gozen, A.O.; Spontak, R.J. Phase Behavior of Triblock Copolymers Varying in Molecular Asymmetry. *Physical Review Letters* **95**, 168306 (2005).
30. Matsen, M.W.; Bates, F.S. Conformationally Asymmetric Block Copolymers. *J. Polym. Sci., Part B: Polym. Phys.* **35**, 945 (1997).
31. McGrath, J.E. *Block Copolymers: Overview and Critical Survey* (Academic Press, 1977).
32. Retsos, H.; Margiolaki, I.; Messaritaki, A.; Anastasiadis, S. H. Interfacial Tension in Binary Polymer Blends in the Presence of Block Copolymers: Effects of Additive MW. *Macromolecules* **34**, 5295-5305 (2001).
33. Riess, G. Micellization of Block Copolymers. *Prog. Polym. Sci.* **28**, 1107-1170 (2003).
34. Wei, B. in *Chemical & Biomolecular Engineering* (NC State Univ., 2005).
35. Spontak, R.J.; Patel, N.P. in *Developments in Block Copolymer Science and Technology* (John Wiley & Sons, 2004).
36. Kane, L.; Norman, D.A.; White, S.A.; Matsen, M.W.; Satkowski, M.M.; Smith, S.D.; Spontak, R.J. Molecular, Nanostructural and Mechanical Characteristics of Lamellar Triblock Copolymer Blends: Effects of Molecular Weight and Constraint. *Rapid Communications* **22**, 281 (2001).
37. Banaszak, M.; Wołoszczuk, S.; Pakula, T.; Jurga, S. Computer simulation of structure and microphase separation in model A-B-A triblock copolymers. *Phys. Rev. E* **66**, 031804 (2002).
38. Fasolka, M.J.; Mayes, A.M. Block Copolymer Thin Films: Physics and Applications. *Annu. Rev. Mater. Res.* **31**, 323-355 (2001).

39. Green, P.F.; Limary, R. Block Copolymer Thin Films: Pattern Formation and Phase Behavior. *Advances in Colloid and Interface Science* **94**, 53-81 (2001).
40. Kim, S.H.; Misner, M.J.; Xu, T.; Kimura, M.; Russell, T.P. Highly Oriented and Ordered Arrays from Block Copolymers via Solvent Evaporation. *Adv. Mater.* **16**, 226 (2004).
41. Wei, B.; Gurr, P. A.; Genzer, J.; Qiao, G. G.; Solomon, D. H.; Spontak, R. J. Dewetting of Star Nanogel/Homopolymer Blends from an Immiscible Homopolymer Substrate. *Macromolecules* **37**, 7857-7860 (2004).
42. Zhu, S.; Liu, Y.; Rafailovich, M.H.; Sokolov, J.; Gersappe, D.; Winesett, D.A.; Ade, H. Confinement-Induced Miscibility in Polymer Blends. *Nature* **400**, 49 (1999).
43. Mayes, A.M.; de La Cruz, M.O. Microphase Separation in Multiblock Copolymer Melts. *J. Chem. Phys.* **91** (1989).
44. Castelletto, V.; Caillet, C.; Hamley, I.W. Liquid-Solid Transition in a Model Hard Sphere System of Block Copolymer Micelles. *Physical Review E* **65**, 050601 (2002).
45. Castelletto, V.; Hamley, I.W., Pedersen, J.S. A Small Angle Neutron Scattering Investigation of the Structure of Highly Swollen Block Copolymer Micelles. *J. Chem. Phys.* **117**, 8124-8129 (2002).
46. Connell, S.D.; Collins, S.; Fundin, J.; Yang, Z., Hamley, I.W. In Situ Atomic Force Microscopy Imaging of Block Copolymer Micelles Adsorbed on a Solid Substrate. *Langmuir* **19**, 10449-10453 (2003).
47. Das, M.; Zhang, H.; Kumacheva, E. Microgels: Old Materials with New Applications. *Annu. Rev. Mater. Res.* **36** (2006).
48. Becker, M.L.; Remsen, E.E.; Pan, D.; Wooley, K.L. Peptide-Derivatized Shell-Cross-Linked Nanoparticles. 1. Synthesis and Characterization. *Bioconjugate Chem.* (2004).
49. Cheng, C.; Qi, K.; Khoshdel, E.; Wooley, K.L. Tandem Synthesis of Core-Shell Brush Copolymers and Their Transformation to Peripherally Cross-Linked and HOLLOWED Nanostructures. *J. Am. Chem. Soc.* **128**, 6808-6809 (2006).
50. Joralemon, M.J.; Murthy, K.S.; Remsen, E.E.; Becker, M.L.; Wooley, K.L. Synthesis, Characterization, and Bioavailability of Mannosylated Shell Cross-Linked Nanoparticles. *Biomacromolecules* **5**, 903-913 (2004).

51. Ma, Q.; Remsen, E.E.; Kowalewski, T.; Schaefer, J.; Wooley, K.L. Environmentally-Responsive, Entirely Hydrophilic, Shell Cross-linked (SCK) Nanoparticles. **1**, 651-655 (2001).
52. Sun, X.; Rossin, R.; Turner, J.L.; Becker, M.L.; Joralemon, M.J.; Welch, M.J.; Wooley, K.L. An Assessment of the Effects of Shell Cross-Linked Nanoparticle Size, Core Composition, and Surface PEGylation on in Vivo Biodistribution. **6**, 2541-2554 (2005).
53. Berndt, I.; Pedersen, J.S.; Richtering, W. Temperature-Sensitive Core–Shell Microgel Particles with Dense Shell. *Angew. Chem. Int. Ed.* **45**, 1737-1741 (2006).
54. Snowden, M.J.; Chowdhry, B.Z.; Vincent, B.; Morris, G.E. Colloidal Copolymer Microgels of N-isopropylacrylamide and Acrylic acid: pH, Ionic Strength and Temperature Effects. *J. Chem Soc., Faraday Trans.* **92**, 5013-5016 (1996).
55. Atkin, R.; Bradley, M.; Vincent, B. Core-Shell Particles Having Silica Cores and pH-Responsive Poly(Vinylpyridine) Shells. *Soft Matter* **1**, 160-165 (2005).
56. Saunders, B.R.; Crowther, H.M.; Vincent, B. Poly[(Methyl Methacrylate)-co-(methacrylic acid)] Microgel Particles: Swelling Control Using pH, Cononsolvency and Osmotic Dewelling. *Macromolecules* **30**, 482-487 (1997).
57. Bouillot, P.; Vincent, B. A Comparison of the Swelling Behavior of Copolymer and Interpenetrating Network Particles. *Colloid Polym. Sci.* **278**, 74-79 (2000).

CHAPTER 2: Autophobicity-driven surface segregation of core-shell polymer nanogel particles (CSNGs)

2.1 Motivation

Organic nanogel (NG) particles are of great research interest due to their three-dimensional structure and characteristics. NGs represent polymeric materials comprising macromolecular networks from nanometers to micron size. Due to their network-induced structural integrity, NGs behave as discrete colloidal particles in a variety of aspects such as the hydrodynamic, electrophoretic, and rheological behavior of dispersions. Having been heavily used as fillers in paint and coating industries due to their highly viscous nature at high molecular weights, the NG particles have attracted tremendous interest in many other technological applications such as controlled drug delivery, designing new-generation of sensors, advance coatings and biomaterial supports/vehicles. When composed of cross-linked macromolecules, they become capable of swelling and contracting, due to changes in surrounding media such as temperature, pH, ionic strength, and solvency, while maintaining their structural integrity. Developments in synthetic techniques have facilitated the customized design of these particles, one of which is of our interest in their use (core-shell structures with controlled chemical/cross-linking) for our application. Technological applications, with variations in chemical compositions tuned by synthesis resulting in vast opportunities of macromolecular structures, are endless with the utilization of these nanogel particles.

2.2 General concepts on core-shell nanogel particles

NG particles of interest in this study are the core-shell type systems, which can be envisaged as permanently cross-linked block copolymer micelles. They can be also modified in the same fashion as block copolymers,¹⁻¹¹ changing their physical structure,^{12,13} which provides opportunities to tailor their end applications, in addition to altering their chemical composition. As physical models of permanent diblock copolymer micelles^{14,15} and alternatives to organically-modified metal or metal oxide nanoparticles,¹⁶⁻¹⁹ core-shell nanoparticles are of technological interest due to their tunable chemistry and physico-chemical properties.^{20,21}

The common structure consists of an organic (A) core surrounded by a dense brush of chemically dissimilar (B) arms (corona).²²⁻²⁴ If the B shell is chemically cross-linked, the A core of such nanoparticles can be removed selectively and used subsequently as a hollow compartment for encapsulation.²⁵⁻²⁸ For instance, if the corona is composed of a stimuli-(e.g., pH,²⁹ temperature³⁰ or ionic strength³¹) responsive polyelectrolyte, it could facilitate encapsulation and release of drugs or enzymes in a controlled manner.³² Studies^{33,34} have also demonstrated that cross-linking the micellar corona which allows the selective-removal of the cores, produces hollow particles. The size of such hollow polymer nanocapsules can be tuned by changing the properties of the copolymer, such as the block size. Altering the cross-link density of the core,³⁰ thus changing the swell-ability of these nanoscale capsules³⁴ in good solvents has also been of great interest for controlled drug delivery.

Unlike block copolymer micelles formed by molecular self-assembly to minimize A-B repulsive interaction, the core-shell morphology of these nanoparticles remains locked-in

by synthesis allowing us to explore them in environments where micelles break and transform.

In this work, we investigate core-shell nanoparticles (denoted as CSNGs in the text) dispersed in a molten thin film of a poly(methyl methacrylate) (PMMA) homopolymer that is identical chemically to, but of substantially higher molecular weight than, the arms forming the shell of the CSNG, which can interact freely with the homopolymer. Due to autophobicity between the densely packed, short PMMA arms of the CSNGs and the long PMMA chains in the matrix, the nanoparticles segregate to the film surface. They cannot, however, break through the surface because of the high surface energy of PMMA. Similar thermal treatment of CSNG-containing PMMA thin films with a polystyrene (PS) capping layer replaces surface energy at the PMMA/air interface by interfacial energy at the PMMA/PS interface, which reduces the energy barrier by an order of magnitude, thereby permitting the nanoparticles to emerge out of the PMMA bulk. This nanoscale process is reversible and can be captured at intermediate degrees of completion.

2.3 Experimental

2.3.1 Materials

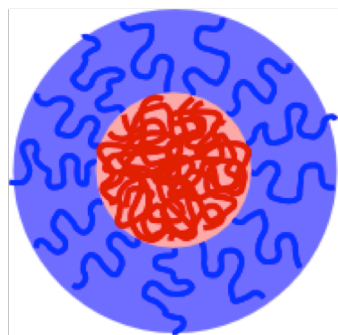
Three polystyrene (PS) homopolymers ($M_w = 50, 216$ with $M_w/M_n = 1.06$ and $M_w = 900$ kDa with $M_w/M_n = 1.10$) were purchased from Pressure Chemical, Inc. (Pittsburgh, PA), and Polymer Source Co., respectively. The PMMA homopolymer ($M_w = 243$ kDa, $M_w/M_n = 1.06$) was supplied by Polymer Source, Inc. (Dorval, Canada). All materials were used as-received.

Solvent-grade toluene was supplied by Fisher Scientific (Fairlawn, NJ) and was used without further purification. CSNGs were synthesized by Dr. Greg Qiao of University of Melbourne, Australia and used as-received.

2.3.2 Particle synthesis and characterization

2.3.2.1 Divinyl benzene-core (DVB)/PMMA-arm particles (CSNGs)

CSNGs were synthesized by Gurr *et al.*³⁵ by the “arms-first” method. The PMMA arms were synthesized first by atom-transfer radical polymerization (ATRP) and then cross-linked with DVB to form discrete particles also under ATRP conditions.



Core:
X-linked divinyl benzene

Shell:
Poly(methyl methacrylate)

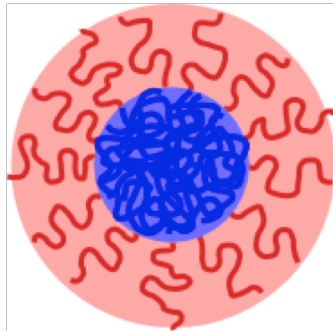
Figure 2.1 Schematic illustration of CSNGs. Structural properties: gyration diameter ($D_g = 26$ nm), number of PMMA arms attached to the core ($\#_{\text{PMMA}} = 28$), molecular weight of each PMMA arm ($M_{\text{PMMA}} = 11$ kDa) and grafting density of the PMMA arms ($\sigma_{\text{PMMA}} = 0.013$ arms/nm²).

Size exclusion chromatography (SEC) measurements were performed in THF using a Waters 717 Plus Autosampler operated in series with a Wyatt Dawn F laser photometer operated at 90° and in parallel with a Waters 410 differential refractometer and a Viscotek T50A differential viscometer. Results from the Viscotek TriSEC[®] software package

calibrated with PMMA standards yielded a number-average molecular weight (M_n) and polydispersity index (PI) of 335 kDa and 1.10, respectively, and a gyration diameter (D_g) of 26 nm. The number of PMMA arms (each with $M_n \approx 11$ kDa and $PI < 1.10$) on a single CSNG was 28.

2.3.2.2 PEGDMA-core/PS-arm particles (CSNG-Rs)

The second type of particles (CSNG-Rs) with poly(ethylene glycol dimethacrylate) (PEGDMA) cores and PS arms were also synthesized by the same method mention above (Please refer to Appendix 2A for more detail in synthesis and characterization).



Core:
Poly(methyl methacrylate)

Shell:
X-linked EG dimethacrylate

Figure 2.2 Schematic illustration of CSNG-R# particles (R# denotes the weight-average molecular weight. Structural properties: gyration diameter ($D_g = 13.1-14.5$ nm), number of PS arms attached to the core ($\#_{PMMA} = 22-32$), molecular weight of each PS arm ($M_{PS} = 11$ kDa) and grafting density of the PS arms ($\sigma_{PMMA} = 0.010-0.012$ arms/nm²).

2.3.3 Thin-film preparation and characterization

The CSNG nanoparticles were mixed (concentration 20% w/w) with PMMA243 (the suffix denotes the molecular weight in kDa) in toluene to form a 2.5 wt% polymer solution, which

was spin-coated onto Si wafer to yield films measuring ≈ 110 nm thick, as discerned from ellipsometry. PS50 (the suffix denotes the molecular weight in kDa) was similarly dissolved in toluene (2% w/w) and spin-coated on glass slides to produce films measuring ≈ 65 nm thick. Each PS film was floated on the surface of DI water and then transferred to the top of a PMMA243/CSNG film in such fashion that half of the PMMA/CSNG film was covered by PS while the other half remained exposed permitting the effect of the PS film to be directly discerned under a given set of treatment conditions. After drying for at least 24 h in air at ambient temperature, each layered specimen was annealed in a Mettler-Toledo hot stage at 180°C for different time intervals under continuous N_2 flow. Visual observation of the post-annealed specimens was performed with an Olympus BX60 optical microscope, whereas atomic force microscopy (AFM) of the PMMA/CSNG surfaces after selective-removal of the top PS50 layer with cyclohexane was conducted with a Digital Instruments 3000 instrument operated in tapping mode.

CSMG-Rs were used for transmission electron microscopy (TEM) samples of the double-layer assemblies. The CSMG-R nanoparticles were incorporated into a thin, spin-coated film of PS216, welded between two thick solvent-cast films of high-molecular-weight PS900. The sample was annealed at 180°C for 24 h and cross-sectioning with a microtome, and, then were exposed to the vapor of 0.5% RuO_4 (aq) for 7 min and examined on a Zeiss EM902 electron spectroscopic microscope operated at 80 kV.

2.4 Results and discussion

2.4.1 Autophobicity-driven segregation of CSNG

According to optical microscopy, the top PS50 layer dewets from the PMMA243/CSNG substrate via nucleation and growth mechanism and forms discrete islands of PS50 under the conditions examined here. This observation is consistent with the previous work by Wei *et al.*,²³ where the particles were embedded in the PS50 layer (cf. Fig. 2.3b).³⁶ Results from that study indicate that bare PMMA regions from which PS fully dewets appear smooth, whereas regions below PS-rich islands become rough due to CSNG presence along the PS/PMMA interface, as depicted in Fig. 2.3c.

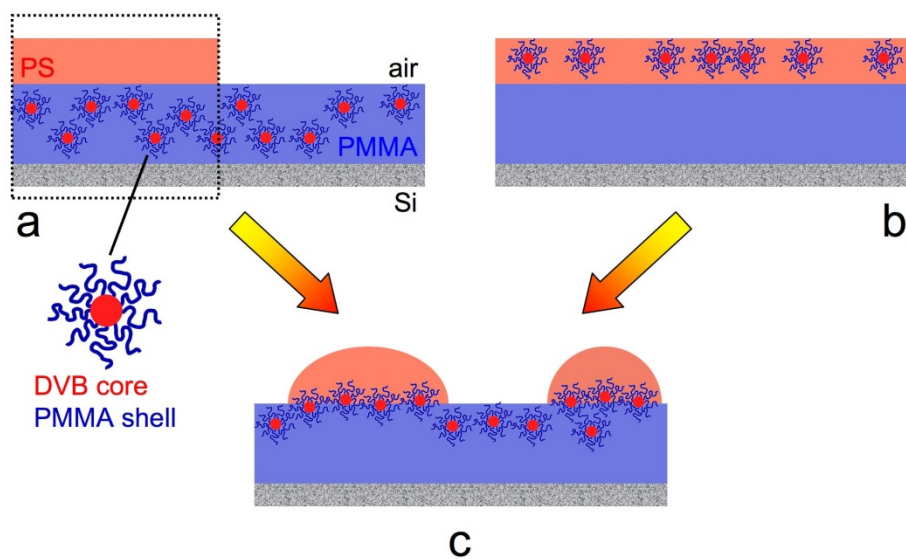


Figure 2.3 Schematic illustrations showing the distribution of CSNGs in (a) PMMA bottom layer and (b) the PS top layer²³ in PS50/PMMA243 bilayer arrangements prior to annealing. Redistribution of the CSMG nanoparticles after annealing at 180°C is portrayed in (c), wherein the PS layer dewets into discrete islands. Irrespective of the starting point (a or b), the CSMG nanoparticles and their aggregates protrude from the PMMA surface under the PS islands, whereas the exposed PMMA surface remains relatively smooth.

In the present study, we have incorporated the CSNG nanoparticles into the PMMA243 homopolymer. PMMA243/CSNG film without the top PS layer remains smooth, with a measured root-mean-square roughness (*RMS*) of 0.78 nm, after annealing for 80 hours. Fig. 2.4a confirms that the dry regions from which the PS layer dewetted are likewise featureless ($R = 0.83$ nm). In both cases, no evidence indicates that CSNGs locate atop the PMMA layer.

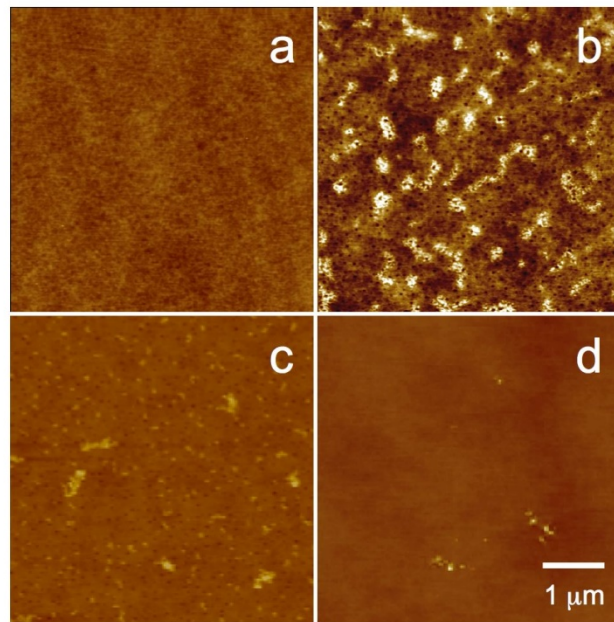


Figure 2.4 Series of AFM height images showing the PMMA surface after different exposure conditions at 180°C: (a) complete dewetting of the PS capping layer after 80 h; formation, and subsequent solvent-removal, of PS islands after (b) 80 and (c) 20 h; and (d) further annealing of (b) without the PS capping layer for 40 h.

In order to image the PMMA243/CSNG/PS50 interface after annealing the bilayer for 80 hours at 180°C, PS50 top layer was removed selectively by cyclohexane. AFM topography scans demonstrated that PMMA/CSNG surface directly below the dewetted PS

islands was significantly roughened ($R = 3.51$ nm), as shown in Fig. 2.4b. Bright features measuring ≈ 30 nm in height are attributed to protruding aggregates of CSNG nanoparticles, which not only segregated from the PMMA homopolymer matrix but also emerged from the PMMA matrix along the PMMA/PS interface. Our experiments have also shown that a CSNG-free PMMA/PS interface is smooth with RMS equal to 0.57 nm.

At shorter annealing times (≈ 20 hours), fewer, discrete features measuring on the order of a few tens of nanometers laterally and ≈ 25 nm in height become evident along the PMMA/CSNG surface below the dewetted PS islands (cf. Fig. 2.4c), revealing that the occurrence, as well as extent, of CSNG protrusion is a time-dependent process. Further annealing of the PS-capped PMMA/CSNG layer heated for 80 hours at 180°C for 40 hours after the PS layer was removed results in total disappearance of the CSNG nanoparticles confirming that emergence of the nanoparticles along the PMMA/PS interface is reversible.

The mechanism by which the nanoparticles sink back into the PMMA homopolymer in the absence of PS capping is illustrated in Fig. 2.5a; the figure shows the boundary of a PS as it slowly dewets from the bottom PMMA₂₄₃/CSNG substrate. Numerous CSNG aggregates are observed clearly where PS contacted the PMMA/CSNG substrate after 6 hours at 180°C . Just outside this region, CSNGs at different levels of submersion are evident, which can be explained by the dynamic nature of the experiment. As depicted schematically in Fig. 2.5b, the CSNGs emerge as before along the PMMA/PS interface, but the front of the PS island recedes as dewetting proceeds.

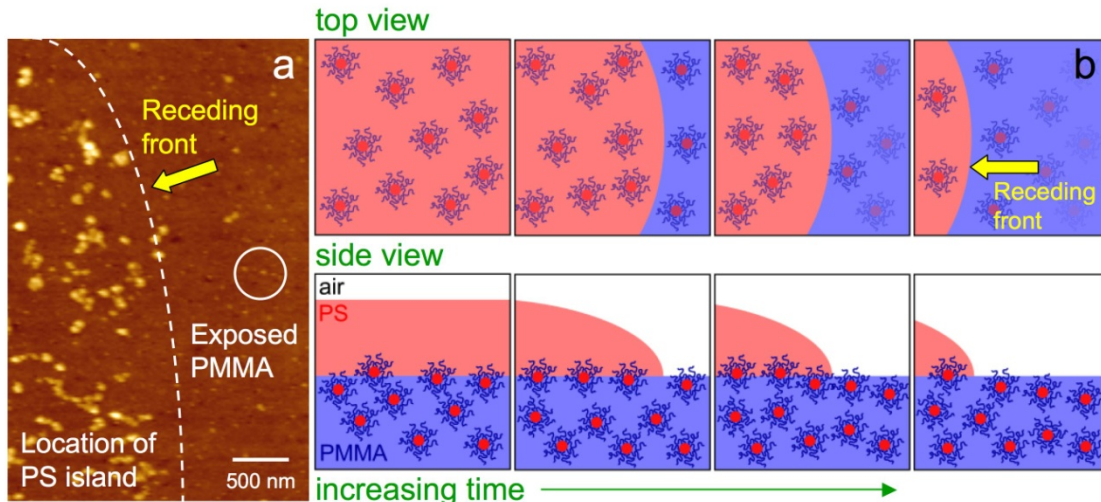


Figure 2.5 (a) AFM height image showing the PMMA surface after annealing for 6 h at 180°C. The dashed line marks the periphery where a dewetted PS island resided prior to selective dissolution, and the circle identifies several partially protruding CSMG nanoparticles that have begun to sink back into the PMMA matrix upon dewetting-induced surface exposure. A schematic series of top and side views are provided in (b) to illustrate this mechanism of surface energy-induced CSMG submersion as a function of annealing (PS dewetting) time.

This sequence of events of the surface segregation and emergence of CSNG nanoparticles from the PMMA matrix depends on the subtle interplay between entropically-driven autophobicity and enthalpically-governed surface/interfacial energy. While autophobicity between the PMMA arms and the PMMA homopolymer drives the nanoparticles to segregate from the PMMA matrix and form protruding aggregates along the surface, the surface energy due solely to PMMA (γ_{PMMA}) serves to suppress the particles, as evidenced by the absence (or disappearance) of nanoscale surface features.

Two structural aspects contribute to autophobicity between free (i.e., homopolymer film) and surface-grafted (i.e., present on the NGs) chains. The first is the high grafting

density of the brush, which comprises the outer layer of the CSNG as discussed above. The second factor is the disparity in chain length between the grafted brush and free homopolymer chains. In the present case, the CSNG arms are much shorter ($N = 110$) than the PMMA homopolymer (with a degree of polymerization, P , of 2260 repeat units). Pioneering the concept of wet and dry polymer brushes, Leibler have proposed a scaling model to predict the onset of autophobicity. According to the model of Leibler and co-workers,^{37,38} free homopolymer chains that are longer than a critical value (P^*) given by $(Na^2/\sigma)^{2/3}$, where N is the number of monomer units in the PMMA homopolymer, a is the statistical length of a single MMA repeat unit (in nm) and σ is the graft density of the PMMA arms (in arms/nm²). If $P \gg P^*$, the long homopolymer chains are unable to wet a chemically identical brush composed of chains wherein the repeat units are of size a . If the statistical length of a single MMA repeat unit is taken as 0.67 nm, $P^* \approx 708$ in the present PMMA/CSNG system so that $P \gg P^*$. In addition, the PMMA chains are also sufficiently long to satisfy the condition of $P > 5N$ required by Liu *et al.*³⁹ for autophobic segregation to occur. The high grafting density of PMMA arms and long PMMA homopolymer promote autophobic segregation of the nanoparticles from the PMMA matrix. The results presented here indicate that for CSNG nanoparticles to emerge alone or as aggregates from the PMMA matrix due to autophobic segregation is regulated by surface (γ_{PMMA}) or interfacial ($\gamma_{\text{PMMA/PS}}$) energy. Segregation to and subsequent emergence along the PMMA surface would induce surface roughening and incur an energy penalty (ΔF_{surf}) on the order of $k_B T/a^2$, assuming that γ_{PMMA} is unaffected by the presence of CSNG nanoparticles with chemically identical arms. Addition of the PS capping layer reduces the energy barrier from γ_{PMMA} to $\gamma_{\text{PMMA/PS}}$, which is

about an order of magnitude smaller (at $\approx 2 \text{ mJ/m}^2$) than γ_{PMMA} , again assuming that the presence of CSNGs again has negligible influence. When the specimens with an exposed PMMA surface are further annealed, the energetics is governed again by γ_{PMMA} , which explains the submersion of CSNGs back into the PMMA matrix when the PS islands are removed.

Autophobicity-driven segregation of CSNG illustrated in Fig. 2.5 could be confirmed directly by cross-sectional transmission electron microscopy (TEM) in Fig. 2.6 by using, a new species-reversed nanoparticle, hereafter designated CSMG-R, with an acrylic core derived from ethylene glycol dimethacrylate (EGDMA) and PS arms. In this case, the PS arms could be selectively stained, thereby permitting direct visualization of the unstained CSMG-R cores. A series of energy-filtered TEM images of stained cross-sections of the annealed trilayered assembly is presented in Fig. 2.6 and reveals several key morphological characteristics. The first such feature evident in Fig. 2.6a is the presence of light dispersions, attributed to the unstained acrylic cores of the CSMG-R nanoparticles, uniformly distributed in an electron-dense (stained) PS matrix. The smallest dispersions measure about 5-15 nm in diameter, whereas the average dispersion size is closer to 20-25 nm, although these and larger dispersions (such as the circled one in Fig. 2.5a) most likely represent nanoparticle aggregates and not individual nanoparticles. Note that the image width exceeds greatly the thickness of the thin film, which implies that the sectioning/viewing direction is not orthogonal to the polymer/polymer interfaces.

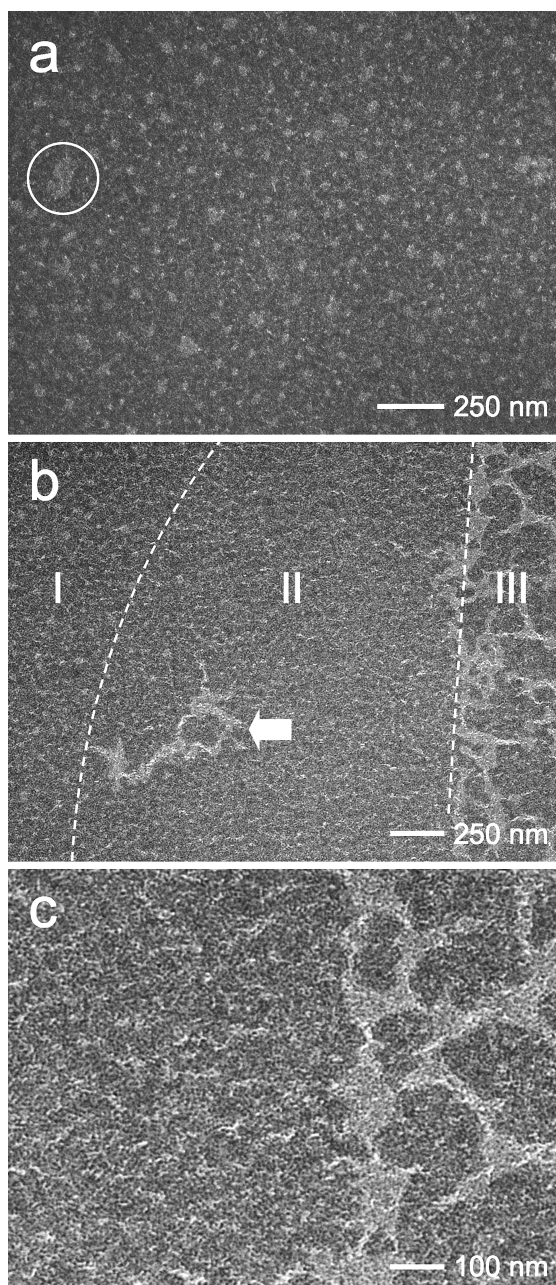


Figure 2.6 Energy-filtered TEM images of CSMG-R nanoparticles acquired from (a) the interior of a thin PS film and (b, c) the interface between 216 kDa PS and 900 kDa PS after annealing at 180°C for 24 h. The PS homopolymer matrices and arms of the CSMG-R nanoparticles are selectively stained and the light features correspond to the unstained acrylic cores of the nanoparticles. The regions separated by dashed lines in (b) are discussed in the text. The circled feature in (a) and the arrow in (b) highlight examples of large nanoparticle aggregates.

In Fig. 2.6b, discrete dispersions are visible in the left-hand region (I) of the image, but disappear for the most part in the region labeled II. This apparent lack of dispersions in Fig. 2.6b and the enlargement in Fig. 2.6c may reflect a reduction in CSMG-R nanoparticles in region II, which is unlikely due to the uniform distribution seen in images such as the one displayed in Fig. 2.6a. Conversely, it may be a consequence of a substantial increase in nanoparticles concentration, which would explain why the diffuse features in Fig. 2.6a are absent, while large, irregularly shaped aggregates (cf. Fig. 2.6b) exist.

It is also important to recognize that such nanoparticle extension from the host film into an immiscible polymer, such as PMMA, is expected to be considerably less pronounced due to enthalpically repulsive interactions. These observations of a similar, but not identical, layered assembly containing species-reversed CSNG-Rs is generally consistent with the postulated picture of nanoparticle enrichment/emergence along the polymer/polymer interface.

2.4.2 Time-dependence of the autophobicity-driven segregation of CSNG

Patterning of polymer surfaces, by utilizing the observed autophobic-segregation phenomenon investigated above, in a controllable fashion is of our interest in order to design surfaces with tailorable properties. The protrusion/elevation of the CSNGs, triggered by surface/interfacial energy interplay, and the simultaneous capability of organized in-plane structure make such systems candidates for active reflective surfaces and smart tags. We have also observed that the annealing time, at which the CSNG-added film is exposed to elevated temperatures, also plays a role in the system kinetics as seen in Fig. 2.7.

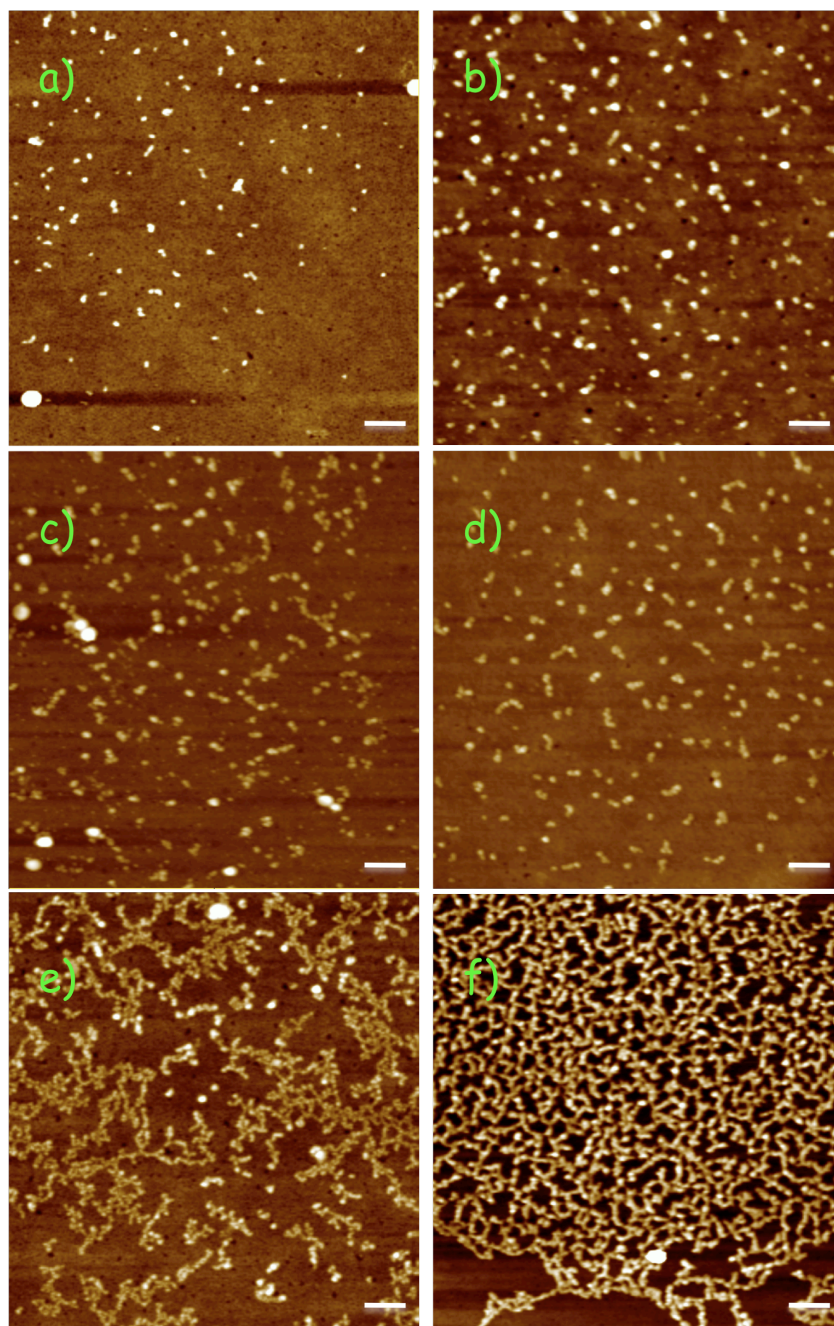


Figure 2.7 AFM height images showing the time-dependence of CSNG aggregation on PMMA243 surface after PMMA243/CSNG/PS50 was annealed for (a) 1 h, (b) 3 h, (c) 6 h, (d) 9 h, (e) 12 h and (f) 84 h at 180°C. PS50 was selectively removed prior to AFM imaging.

2.4.3 Image analysis of CSNG

The images collected with the AFM were analyzed with Scion image analysis software to understand how dense the particles and aggregates pattern on the PS/PMMA interface at different time intervals.

According to the image analysis, particle clusters in size of 90-150 nm (4-6 individual particles considering the diameter of an individual particle, 26 nm) form network-like structures after 24 hrs and 80 hrs of annealing time intervals. The chains can be up to 150-200 clusters. Random distribution of particle clusters (no network-like structures) can be observed at early times (6 hrs of annealing). There are three important parameters in the analysis: (i) the number of particles with respect to total area density of the particles, (ii) total number of particles and (iii) average aggregate size. Area and number density calculations of the particles were performed in Scion Image Analysis software. Threshold values were optimized accordingly. Increasing the threshold value decreases the total particle area, hence the total # of particles except for the images in which the particles form long chains. It affects both the area and number density.

Figure 2.8 represents the total number of particles in the system with respect to various annealing times. According to the plot, the total number of the MG particles segregated from the PMMA matrix to the PS/PMMA interface increases as the annealing time increases. PMMA homopolymer relaxes as annealing time is increased, thereby permitting CSNGs to diffuse to the interface.

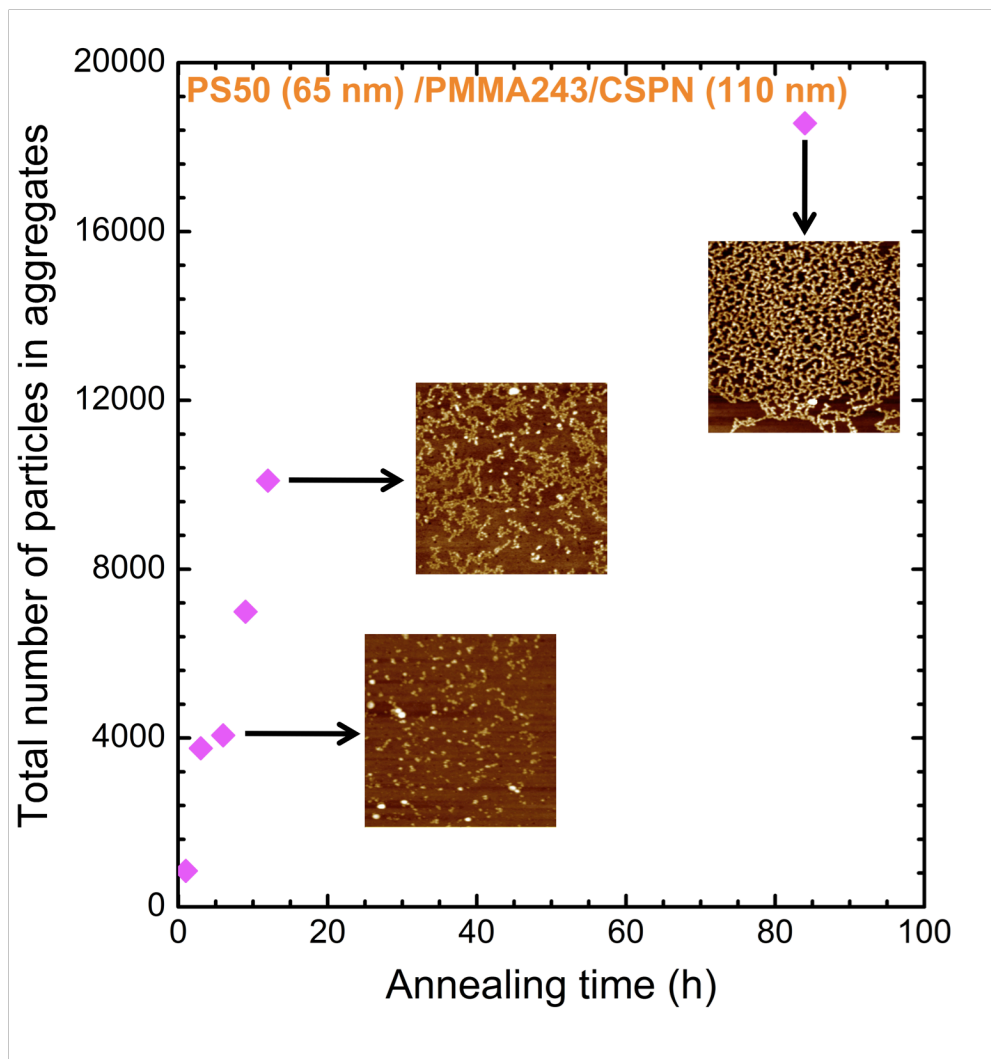


Figure 2.8 Total number of particles in aggregates vs. annealing time.

2.4.4 Electric field-driven segregation of CSNG

The mechanism and length scale of the process of dewetting of a thin liquid film from a non-wettable substrate depend on the film thickness, viscosity, and surface tension of the film, and van der Waals forces affecting the liquid-substrate interface.^{40,41} Earlier in this chapter, we mentioned the segregation of CSNG particles from a large PMMA matrix and by

changing the energy of the surface; we could pattern these particles at PS/PMMA interfaces. Moreover, by using a simple elastomeric stamp to selectively contact the PMMA/CSMG film, we have demonstrated that CSNGs can be patterned on surfaces in a controllable fashion and this process is thermally reversible.⁴²

Another promising approach to pattern surfaces in a controlled fashion in thin polymer films is by applying an electric field. Similarly, electric fields can be used to induce an instability that depends on parameters such as the conductivity of the polymer film in the viscoelastic regime (above T_g) and the strength of the applied field. External electric fields were used to amplify interfacial fluctuations in the air/polymer/polymer system where one polymer dewets the other.⁴³ The principle involved here uses the destabilizing effect of electric fields on dielectric interfaces. An electric field applied normal to an interface between two dielectric materials with different polarizabilities causes an interfacial electrostatic pressure arising from the uncompensated displacement charges.⁴⁴ Along with the electrostatic forces, the dewetting forces at two of the interfaces played a major role in the type of structures obtained. Russell and his coworkers have shown that PS/PMMA interface could be destabilized by applying a high electric field, leading to the formation of novel structures such as pillars across the electrodes, having a PS core with a PMMA sheath.⁴⁵ Steiner demonstrated that strong field gradients could produce forces that can overcome the surface tension in thin liquid films, inducing an instability that features a characteristic hexagonal order.⁴⁶

Considering the effect of applying an electric field on thin-film geometries, we have designed a new system, where we have tried to pattern CSNGs, segregating from large

PMMA homopolymer. Our new design is identical to the system, where CSNGs segregated from a PMMA homopolymer to the PMMA/PS interface, except we apply a high electric field on the PMMA243/CSNG layer instead of covering it with a sacrificial PS layer to switch the interplay between surface tension and interfacial tension to pattern the particles (cf. Fig. 2.9)

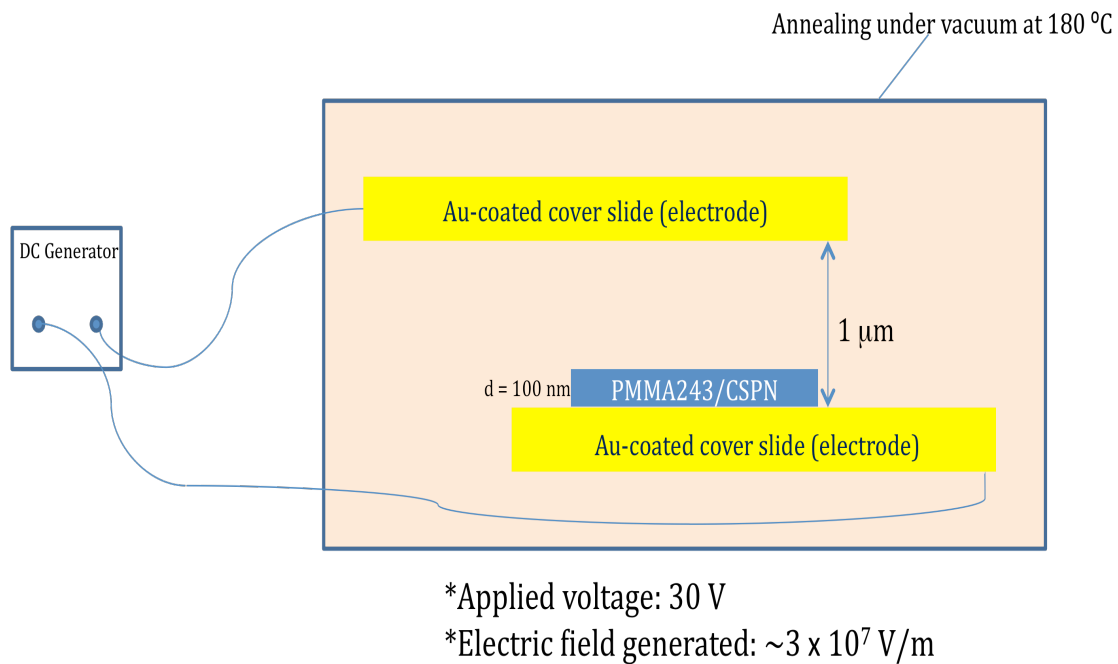


Figure 2.9 Schematic illustration of the electric field experimental setup.

In this experimental setup, two glass slides were coated with Au to be used as electrodes. A 100nm thick PMMA243/CSNG (20 wt% loading) was sun-cast on a glass slide and floated on one of the Au electrodes. After the sample was dried at room temperature

overnight, the gap between the electrodes was set by fumed silica particles with a diameter of 1 micron. A DC generator with 30 V was used to generate a high electric field of 3×10^7 V/m between the electrodes at 1-micron gap. The sample was annealed for 24 hours at 180°C under vacuum.

Optical micrographs of Au-coated electrodes show defects on the electrodes (cf. Fig 2.10a) and this fact affects the quality of the floated-PMMA/CSNG layer (cf. Fig 2.10b). These heterogeneities, as clearly seen in Fig. 2.9c, force the PMMA/CSNG layer to dewet from the Au-coated surface, possibly acting as nucleation sites, when the film is in liquid state. The film continues dewetting as the sample is at 180°C under electric field for an additional 24 hours.

AFM images of PMMA/CSNG layer on Au electrode after floating show an RMS value of 2 nm (cf. Fig. 2.11a). The surface of PMMA/CSNG smoothens (RMS = 0.8 nm) after 27 h at 180°C showing no presence of the particles. When the electric field is applied, the topographical scan of AFM height images of PMMA/CSNG layer on the dewetted areas (cf. Fig. 2.10c-d) after 24 h at 180°C exhibit features on the order of 30nm in height, indicating (as seen previously in the earlier systems) particle aggregates can be patterned on the surface.

Our preliminary results have shown that PMMA-arm particles can be patterned on PMMA homopolymer surfaces via electric field without the need of a sacrificial PS layer. Although the Au substrate brings heterogeneities to the PMMA/CSNG layers, the findings are very promising. (Please refer to Chapter 7 for recommended future work on this project).

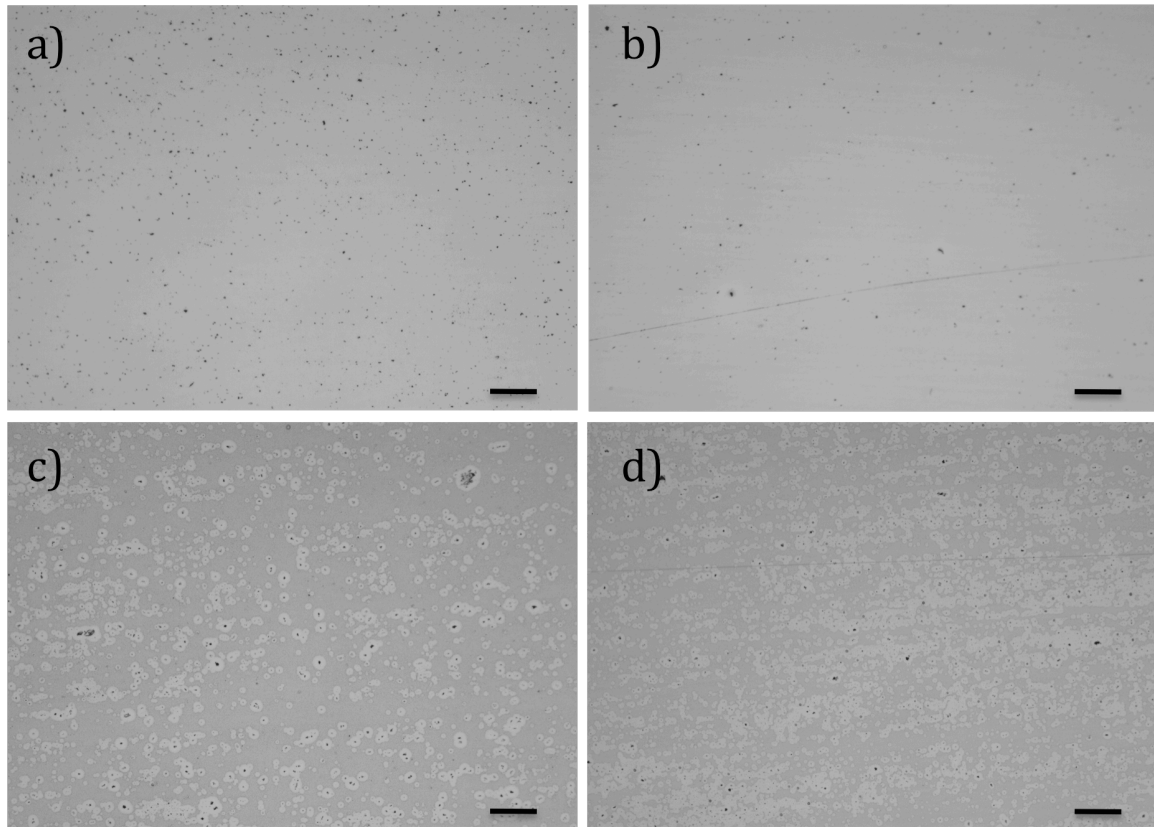


Figure 2.10 Optical microscopy images of (a) Au-coated glass surface, (b) PMMA/CSNG layer on Au electrode after floating, (c) PMMA/CSNG after on Au-electrode after 27 h at 180°C, and (d) PMMA/CSNG on Au, after 24 h electric field applied at 180°C. Scale marker is 50 microns.

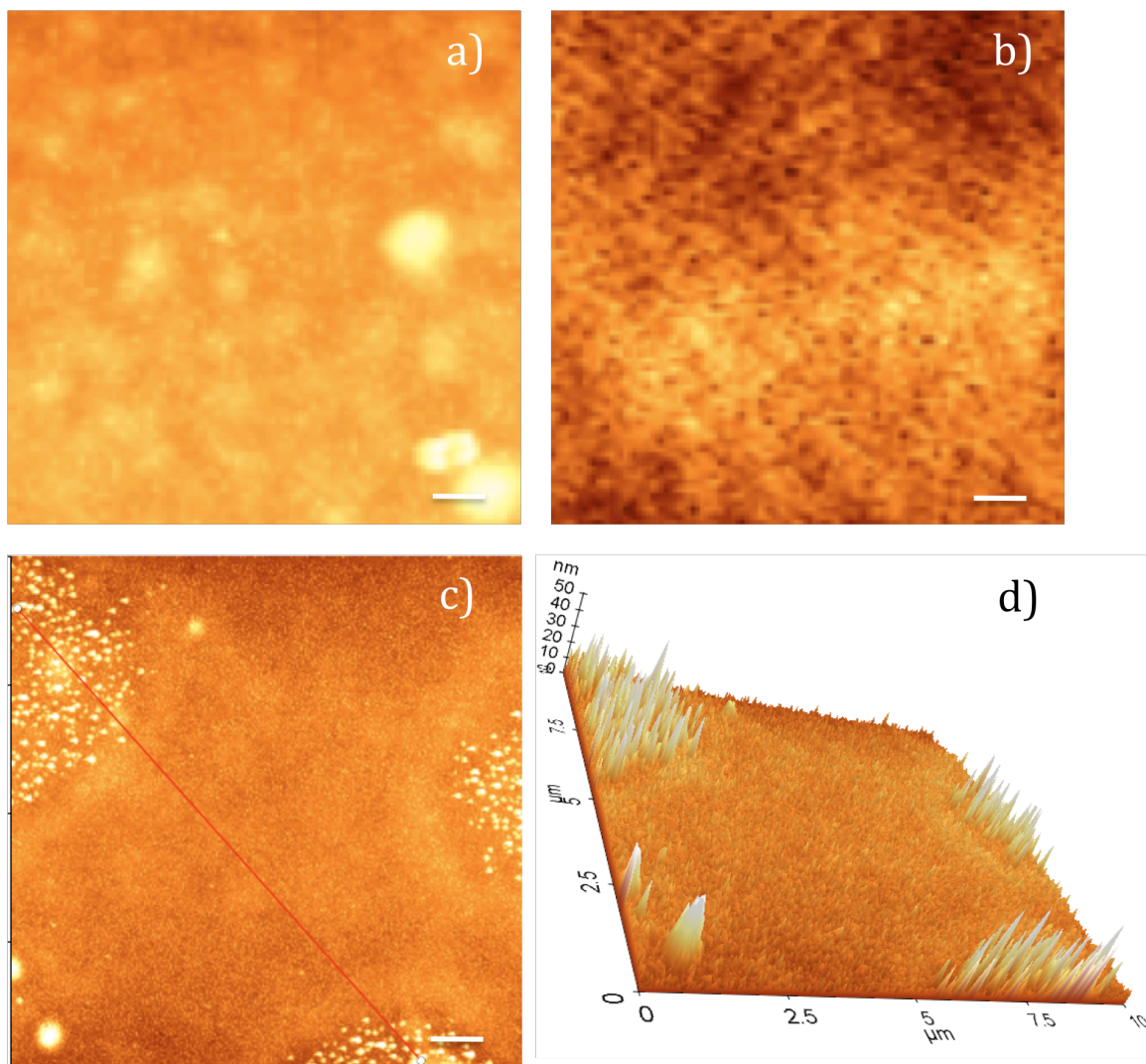


Figure 2.11 AFM images of (a) PMMA/CSNG layer on Au electrode after floating, (b) PMMA/CSNG after on Au-electrode after 27 h at 180°C, (c) PMMA/CSNG (dewetted areas corresponding to cf. Fig. 2.9c) on Au after 24 h at 180°C electric field applied and (d) 3D image of the structuring in part c. Scale marker is 1 micron.

In this work, we investigated the thermal response of CSNGs composed of a cross-linked divinylbenzene core and poly(methyl methacrylate) (PMMA) arms as they segregate from PMMA homopolymer due to autophobicity. When in contact with a free surface, the particles migrate to the PMMA surface but remain inside the PMMA. When a thin film of polystyrene (PS) is placed on top of a PMMA/CSNG film, the particles segregate to and thus roughen the PMMA/PS interface, as evidenced by AFM imaging. We attribute this behavior to a change in surface vs. interfacial energetics. Specifically, while the high surface energy of the native PMMA film keeps the particles inside the bulk PMMA, placing a thin PS layer on top of the PMMA/CSNG film decreases the PMMA/PS interfacial tension by about an order of magnitude, which consequently permits segregation of the μ GPs to penetrate the PMMA/PS interface.

In order to fully comprehend the kinetics of the particle elevation from/protrusion to PMMA homopolymer, we have systematically varied the annealing time of the particle-added PS/PMMA laminates. Even at relatively short annealing times, PS/PMMA interface roughens due to particle presence in forms of aggregates and as the annealing time is further increased, aggregates increase in number and size as well.

Our efforts in patterning the CSNGs via electric field, without the need of a capping PS layer, have demonstrated that parameters such as the type of the electrode, voltage applied play an important role in this behavior.

References

1. Jones, C. D.; McGrath, J. G. & Lyon, L. A. Characterization of cyanine dye-labeled poly(N-isopropylacrylamide) core/shell microgels using fluorescence resonance energy transfer. *Journal of Physical Chemistry B* **108**, 12652-12657 (2004).
2. Jones, C. D. & Lyon, L. A. Dependence of shell thickness on core compression in acrylic acid modified poly(N-isopropylacrylamide) core/shell microgels. *Langmuir* **19**, 4544-4547 (2003).
3. Jones, C. D. & Lyon, L. A. Shell-restricted swelling and core compression in poly(N-isopropylacrylamide) core-shell microgels. *Macromolecules* **36**, 1988-1993 (2003).
4. Hazot, P.; Pichot, C. & Maazouz, A. Synthesis of hairy acrylic core-shell particles as toughening agents for epoxy networks. *Macromolecular Chemistry and Physics* **201**, 632-641 (2000).
5. Matsuoka, H.; Fujimoto, K. & Kawaguchi, H. Stimuli-response of microsphere having poly(N-isopropylacrylamide) shell. *Polymer Journal* **31**, 1139-1144 (1999).
6. Senff, H.; Richtering, W.; Norhausen, C.; Weiss, A. & Ballauff, M. Rheology of a temperature sensitive core-shell latex. *Langmuir* **15**, 102-106 (1999).
7. Zhou, G.; Elaissari, A.; Delair, T. & Pichot, C. Synthesis and characterization of surface-cyanofunctionalized poly(N-isopropylacrylamide) latexes. *Colloid and Polymer Science* **276**, 1131-1139 (1998).
8. Duracher, D.; Sauzedde, F.; Elaissari, A.; Pichot, C. & Nabzar, L. Cationic amino-containing N-isopropyl-acrylamide-styrene copolymer particles: 2-surface and colloidal characteristics. *Colloid and Polymer Science* **276**, 920-929 (1998).
9. Duracher, D.; Sauzedde, F.; Elaissari, A.; Perrin, A. & Pichot, C. Cationic amino-containing N-isopropylacrylamide-styrene copolymer latex particles: 1 - Particle size and morphology vs. polymerization process. *Colloid and Polymer Science* **276**, 219-231 (1998).
10. Kato, T.; Fujimoto, K. & Kawaguchi, H. Permeation Control by Thermosensitive Shell Layer of Submicron Microspheres. *Polymer Gels and Networks* **2**, 307-313 (1994).
11. Leung, M. F.; Zhu, J. M.; Harris, F. W. & Li, P. New route to smart core-shell polymeric microgels: Synthesis and properties. *Macromolecular Rapid Communications* **25**, 1819-1823 (2004).

12. Jones, C. D.; Lyon, L. A. Synthesis and characterization of multiresponsive core-shell microgels. *Macromolecules* **33**, 8301-8306 (2000).
13. Gan, D. J. & Lyon, L. A. Tunable swelling kinetics in core-shell hydrogel nanoparticles. *Journal of the American Chemical Society* **123**, 7511-7517 (2001).
14. Riess, G. Micellization of block copolymers *Prog. Polym. Sci.* **28**, 1107-1170 (2003).
15. Joralemon, M. J.; O'Reilly, R. K.; Hawker, C. J.; Wooley, K. L. . Shell Click-crosslinked (SCC) nanoparticles: A new methodology for synthesis and orthogonal functionalization *J. Am. Chem. Soc.* **127**, 16892-16899 (2005).
16. Caruso, F. 2001, 13, 11. Nanoengineering of particle surfaces *Adv. Mater.* **13**, 11 (2001).
17. Bockstaller, M. R.; Mickiewicz, R. A.; Thomas, E. L. . Block copolymer nanocomposites: Perspectives for tailored functional materials *Adv. Mater.* **17**, 1331-1349 (2005).
18. Kim, B. J.; Chiu, J. J.; Yi, G. R.; Pine, D. J.; Kramer E. J. Nanoparticle-induced phase transitions in diblock-copolymer films *Adv. Mater.* **17**, 2618 (2005).
19. Spontak, R. J.; Shankar, R.; Bowman, M. K.; Krishnan, A. S.; Hamersky, M. W.; Samseth, J.; Bockstaller, M. R.; Rasmussen, K. Ø. . Selectivity- and size-induced segregation of molecular and nanoscale species in microphase-ordered triblock copolymers *Nano Lett.* **6**, 2115 (2006).
20. Ho, A. K.; Iin, I.; Gurr, P. A.; Mills, M. F.; Qiao, G. G. Synthesis and characterization of star-like microgels by one-pot free radical polymerization *Polymer* **46**, 6727-6735 (2005).
21. Connal, L. A.; Qiao, G. G. Preparation of porous poly(dimethylsiloxane)-based honeycomb materials with hierarchal surface features and their use as soft-lithography templates *Adv. Mater.* **18**, 3024 (2006).
22. Connal, L. A.; Gurr, P. A.; Qiao, G. G.; Solomon, D. H. From well defined star-microgels to highly ordered honeycomb films *J. Mater. Chem.* **15**, 1286 (2005).
23. Wei, B.; Gurr, P. A.; Genzer, J.; Qiao, G. G.; Solomon, D. H.; Spontak, R. J. . Dewetting of star nanogel/homopolymer blends from an immiscible homopolymer substrate *Macromolecules* **37**, 7857 (2004).

24. Wiltshire, J. T.; Qiao, G. G. . Degradable core cross-linked star polymers via ring-opening polymerization *Macromolecules* **39**, 9018 (2006).
25. Zhang, Q.; Remsen, E. E.; Wooley, K. L. Shell cross-linked nanoparticles containing hydrolytically degradable, crystalline core domains *J. Am. Chem. Soc.* **122**, 3642 (2000).
26. Wooley, K. L. Shell crosslinked polymer assemblies: Nanoscale constructs inspired from biological systems *J. Polym. Sci. A: Polym. Chem.* **38**, 1397 (2000).
27. Sauer, M.; Streich, D.; Meier, W. pH-sensitive nanocontainers *Adv. Matr.* **13**, 1649-1651 (2001).
28. Kaneda, I.; Vincent, B. J. Swelling behavior of PMMA-g-PEO microgel particles by organic solvents *Colloid Interface Sci.* **274**, 49-54 (2004).
29. Sauer, M.; Streich, D. & Meier, W. pH-sensitive nanocontainers *Advanced Materials* **13**, 1649-1651 (2001).
30. Zha, L.; Zhang, Y.; Yang, W.; Fu, S. Monodisperse temperature-sensitive microcontainers *Advanced Materials* **14**, 1090-1092 (2002).
31. Ibarz, G.; Dahne, L.; Donath, E.; Mohwald, H. *Advanced Materials* **13**, 1324 (2001).
32. Sauer, M. & Meier, W. Responsive nanocapsules *Chemical Communications*, 55-56 (2001).
33. Zhang, Q.; Remsen, E. E. & Wooley, K. L. Shell cross-linked nanoparticles containing hydrolytically degradable, crystalline core domains. *Journal of the American Chemical Society* **122**, 3642-3651 (2000).
34. Huang, H. Y.; Remsen, E. E.; Kowalewski, T. & Wooley, K. L. Nanocages derived from shell cross-linked micelle templates. *Journal of the American Chemical Society* **121**, 3805-3806 (1999).
35. Gurr, P. A.; Qiao, G. G.; Solomon, D. H.; Harton, S. E. & Spontak, R. J. Synthesis, characterization, and direct observation of star microgels. *Macromolecules* **36**, 5650-5654 (2003).
36. Wei, B.; Gurr, P. A.; Genzer, J.; Qiao, G. G.; Solomon, D. H.; Spontak, R. J. Dewetting of Star Nanogel/Homopolymer Blends from an Immiscible Homopolymer Substrate. *Macromolecules* **37**, 7857-7860 (2004).

37. Leibler, L. Block Copolymers At Interfaces *Physica A* **172**, 258-268 (1991).
38. Leibler, Ludwik; Orland, Henri & Wheeler, John C. Theory of critical micelle concentration for solutions of block copolymers *The Journal of Chemical Physics* **79**, 3550-3557 (1983).
39. Liu, Y.; Rafailovich, M. H.; Sokolov, J.; Schwarz, S. A.; Zhong, X.; Eisenberg, A.; Kramer, E. J.; Sauer, B. B. & Satija, S. Wetting Behavior of Homopolymer Films on Chemically Similar Block Copolymer Surfaces. *Physical Review Letters* **73**, 440-443 (1994).
40. Lambooy, P.; Phelan, K.C.; O. Haugg, O Dewetting at the liquid-liquid interface. *Phys. Rev. Lett.* **76**, 1110-1113 (1996).
41. Sferrazza, M.; Heppenstall-Butler, M.; Cubitt, R. Interfacial instability driven by dispersive forces: The early stages of spinodal dewetting of a thin polymer film on a polymer substrate. *ibid.* **81**, 5173–5176 (1998).
42. Wei, B.; Gurr, P.A.; Gozen, A.O.; Blencowe, A.; Solomon, D.H.; Qiao, G.G.; Spontak, R.J.; Genzer, J. Autophobicity-driven surface segregation and patterning of core-shell microgel nanoparticles *Nano Letters* **8**, 3010-3016 (2008).
43. Lin, Z.; Kerle, T.; Russell, T.P.; Schaffer, E.; Steiner, U. Electric Field Induced Dewetting at Polymer/Polymer Interfaces. *Macromolecules* **35**, 6255-6262 (2002).
44. Morariu, M.D.; Voicu, N.E.; Schaffer, E. Lin, Z.; Russell, T.P.; Steiner, U. Hierarchical structure formation and pattern replication induced by an electric field *Nature* **2**, 48-52 (2003).
45. Leach, K.A.; Gupta, S.; Dickey, M.D.; Willson, C.G., Russell, T.P. Electric field and dewetting induced hierarchical structure formation in polymer/polymer/air trilayers *CHAOS* **15**, 047506 (2005).
46. Schaffer, E.; Thurn-Albrecht, T.; Russell, T.P.; Steiner, U. Electrically induced structure formation and pattern transfer. *Nature* **403**, 874-877 (2000).

Appendix

Appendix A. Synthesis and characterization of CSNG-Rs

Chemical reagents were purchased from Ajax, BDH, Scharlau or Sigma-Aldrich, and were used without further purification, unless stated otherwise. Styrene monomer (>99 %) was purified by passing it twice through basic alumina. The EGDMA monomer (>98 %) was purified by passing it through a sinter bed loaded with hydroquinone (HQ) and monomethyl ether hydroquinone (MEHQ) inhibitor remover (Aldrich), on top of basic alumina.

Synthesis of the linear PS macroinitiator: 1-Bromoethylbenzene (0.083 mL, 0.606 mmol), styrene (10.0 mL, 87.3 mmol), CuBr (0.085 g, 0.593 mmol) and PMDETA (0.253 g, 1.21 mmol) were added to a dry Schlenk tube containing a stir bar and agitated vigorously for 5 min. The mixture was degassed via 4 freeze-pump-thaw cycles and back-filled with Ar. After heating at 110°C for 3.33 h (the conversion of styrene according to GCMS was 69%), the mixture was cooled to ambient temperature, diluted with THF (*ca.* 100 mL) and filtered through a sinter bed loaded with basic alumina on top of filter aid. The filtrate was concentrated *in vacuo* and the residue was re-dissolved in THF (*ca.* 40 mL) prior to precipitation into methanol (*ca.* 400 mL). The resulting precipitate was collected by filtration and dried *in vacuo* (0.05 mmHg) for 12 h to obtain the desired linear PS macroinitiator as a white solid, 5.88 g (64%). According to SEC-MALLS analysis ($dn/dc = 0.181$), $M_n = 10.6$ kDa and $PI = 1.01$.

Synthesis of CSMG-R nanoparticles: The PS macroinitiator (2.00 g, 0.187 mmol), CuBr (0.026 g, 0.183 mmol), PMDETA (0.078 mL, 0.375 mmol), EGDMA (15 equiv., 0.531 mL, 2.81 mmol) and anhydrous anisole (13.8 mL) were added to a dry Schlenk tube

containing a stir bar. The tube was sealed and stirred until the macroinitiator completely dissolved. The mixture was then subjected to 4 freeze-pump-thaw cycles and back filled with Ar. After heating at 100°C for 40 h (the conversion of EGDMA according to GCMS was 96%), the mixture was cooled to ambient temperature, diluted with THF (*ca.* 100 mL) and filtered through a sinter bed loaded with basic alumina on top of a layer of filter aid. The filtrate was concentrated *in vacuo* and the crude CSMG-R nanoparticles was re-dissolved in THF (*ca.* 20 mL) prior to precipitation into methanol (*ca.* 200 mL). The resulting solid was re-precipitated into methanol two additional times, and the precipitate thus formed was removed by filtration and further purified via fractional precipitation (in THF/methanol) and drying *in vacuo* (0.05 mmHg) to yield the desired CSMG-R nanoparticles as a white solid, 1.41 g (maximum yield = 2.553 g). According to SEC-MALLS analysis ($dn/dc = 0.181$), $M_n = 376$ kDa and $PI = 1.16$.

The SEC was performed using a Shimadzu size exclusion chromatogram with a Wyatt DAWN EOS multi-angle laser light scattering (MALLS) detector ($\lambda = 638$ nm), a Wyatt OPTILAB DSP interferometric refractometer ($\lambda = 638$ nm) and a Shimadzu SPD-10A UV-Vis detector, using three phenogel columns (50, 10^3 and 10^5 nm) and SEC-grade THF (conducted at 30°C and a flow rate of 1 ml/min). Gas chromatography/mass spectrometry (GCMS) was performed using a Shimadzu GC-17A gas chromatograph with a Shimadzu GCMS-QP5000 electron ionization mass spectrometer and Zebron ZB-5 capillary column (solid phase 5%-phenyl/95%-dimethylpolysiloxane), measuring 30 m x 0.25 mm x 0.25 μm .

Microscopy of CSMG-R nanoparticles: After the trilayered assembly described in the text was fabricated, it was subjected to cross-sectional ultramicrotomy conducted at ambient

temperature, and resultant electron-transparent sections were exposed to the vapor of 0.5% RuO₄(aq) for 7 min to promote selective staining of the phenyl rings on PS. Energy-filtered TEM was performed on a Zeiss EM902 electron spectroscopic microscope operated at an accelerating voltage of 80 kV and an energy loss of 50 eV. Images were acquired on plate film and subsequently digitized at a resolution of 1000 dpi prior to analysis with the Gatan Digitalmicrograph software suite and presentation.

Chapter 3: Lateral structuring at immiscible polymer/polymer interfaces induced by aggregation and adsorption of core-shell polymer nanoparticles

3.1 Motivation

In our previous work,¹ we have demonstrated that by varying the interfacial energy between the matrix poly(methyl methacrylate (PMMA) film and the surrounding medium, core-shell nanogel particles (CSNGs), which consist of a cross-linked polystyrene (PS) core and a PMMA corona could be triggered to either emerge from or submerge into the PMMA substrate in a reversible fashion. The ability of these nanoparticles to extend through a polymer/polymer interface and then submerge below an exposed polymer surface upon thermal treatment provides opportunities for “active” and reversible patterning of materials surfaces.

As mentioned in the previous chapter, core-shell nanogel particles of interest can be imaged as permanent block copolymer micelles. While block copolymers and inorganic nanoparticles are employed routinely in fundamental studies and commercial technologies as compatibilizing agents in polymer blends, this study seeks to establish the type and extent of in-plane interfacial structuring that proceeds upon annealing thin-film laminates containing organic nanogel particles in the melt.

In this work, we extend our previous study to explore the effect of reverse core-shell nanogel particles (denoted as CSNG-R), made of a cross-linked acrylic core, poly(ethylene glycol dimethacrylate) (PEGDMA) and PS arms, on interfacial activity and lateral structuring at PMMA/PS contacts. The experimental variables we explore in this study include the

concentration and molecular weight of CSNG-R, as well as, the molecular weight of PS so that the spatiotemporal evolution of lateral interfacial structuring can be better understood.

3.2 Experimental

3.2.1 Materials

CSNG-R with two different molecular weights were synthesized by Dr. Greg G. Qiao of the University of Melbourne, Australia, with a cross-linked acrylic core derived from ethylene glycol dimethacrylate (EGDMA) and PS arms via the "arms-first" route.² Low-molecular-weight CSNG-R, denoted as CSNG-R263, possess a number-average molecular weight (M_n) and polydispersity index (PDI) of 263 kDa and 1.14, respectively, and a gyration diameter (D_g) of 13 nm. The M_n and PDI of the high-molecular-weight CSNG-R, denoted as CSNG-R378 is 378 kDa and 1.16, respectively, and a gyration diameter (D_g) of 15 nm. The numbers of PS arms (each with $M_n \approx 11$ kDa and $PDI < 1.10$) on CSNG-R263 and CSNG-R378 were 22 and 32 arms/particle, respectively. The properties of these CSNP-Rs are listed in Table 3.1.

Table 3.1 Properties of CSNG-R(w). (“w” denotes the molecular weight in kg/mol)

Particles	Total M_n (kDa)	PDI	# of PS arms	MW of each PS arm (kDa)	Grafting density (PS arms/nm ²)
CSNG-R263	263	1.14	22	10.7	0.010
CSNG-R378	378	1.16	32	10.7	0.012

Grafting density (σ) values of the PS arms in the CSNG-R can be estimated conservatively as 0.010 and 0.012 PS arms/nm² for CSNG-R263 and CSNG-R378, respectively, based on the outer CSNG-R surface area given by πD_g^2 . With these molecular parameters known, the PS arms comprising the shell are analogous to a PS brush.

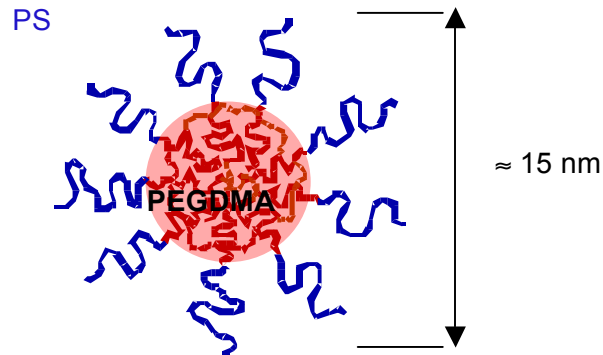


Figure 3.1 Illustration of CSNG-R378.

The equivalent value of σN for CSNG-R263 and CSNG-R378, where N is the number of repeat units per chain in the brush, are estimated to be ≈ 1.03 and ≈ 1.23 , respectively. Since σN exceeds unity, a high PS brush density can be reasonably presumed wherein the PS arms compact laterally and stretch outward, normal to the core-shell interface, in similar fashion to brushes grafted to a flat surface.

3.2.2 Methods

CSNG-R263 and CSNG-R378 were mixed separately in concentrations varying from 1 to 20% w/w with PS of two different molecular weights of $M_n = 204$ kDa, PDI = 1.06 (denoted as PS204) and 849 kDa, PDI = 1.06 (denoted as PS849) and dissolved in toluene (2 wt%) and spin-coated onto silicon wafer to produce films measuring ≈ 95 -105 nm thick. PMMA films ($M_n = 51$ kDa, PDI = 1.06, denoted as PMMA51) were spin-casted from 1.55 wt% in toluene solution onto glass slides measuring ≈ 55 -65 nm thick, as discerned from ellipsometry. Each PMMA film was floated on the surface of deionized water and subsequently transferred to the top of a PS+CSNG-R film in such fashion that a half of the PS/CSNG-R film was covered by PMMA while the other half remained exposed, thereby permitting the effect of the PMMA film to be directly observed under a given set of treatment conditions. After drying for at least 24 h in air at ambient conditions, each layered specimen was annealed in a Mettler-Toledo hot stage at two different temperatures, 180°C and 190°C for various times under continuous flow of N_2 . Visual observation of the post-annealed specimens was performed with an Olympus BX60 optical microscope (under DIC optics unless specified as either Bright-field or RGB on the figures) before and after top PMMA layer washed off with acetic acid (in order to selectively remove PMMA as required). Optical micrographs were taken at 20x magnification unless specified otherwise. Surface topologies of the PS surface and PS/PMMA interface (after dewetting and/or selective solvent removal of PMMA) were examined by atomic force microscopy (AFM) in tapping mode on Digital Instruments 3000 and PSIA XE-100 instruments, respectively.

3.3 Results and discussion

3.3.1 CSNG as stabilizers

The CSNG architecture and concentration can influence the wetting property, hence, the stability of thin polymer films. Krishnan et al.³ have shown that the addition of PS nanoparticles into a thin PS homopolymer layer inhibits, and in some cases eliminates, dewetting because an enriched layer of PS nanoparticles is present on the substrate surface. The difference in the particle architecture can lead to dividing their blend film into two-enriched layers. The instability phenomenon is driven by the effective molecular interactions acting between all the interfaces that separate the substrate, bottom layer, top layer and free top layer/air interface.

In the discussion that follows we will present data from samples utilizing both CSNG-R263 and CSNG-R378 interchangeably. While the general behavior in both systems is qualitatively the same, some differences exist. When appropriate, we will stress those dissimilarities. **Figure 3.1** shows optical micrographs of pure PS204 and PS204/CSNG-R378 as cast films on silicon wafers.

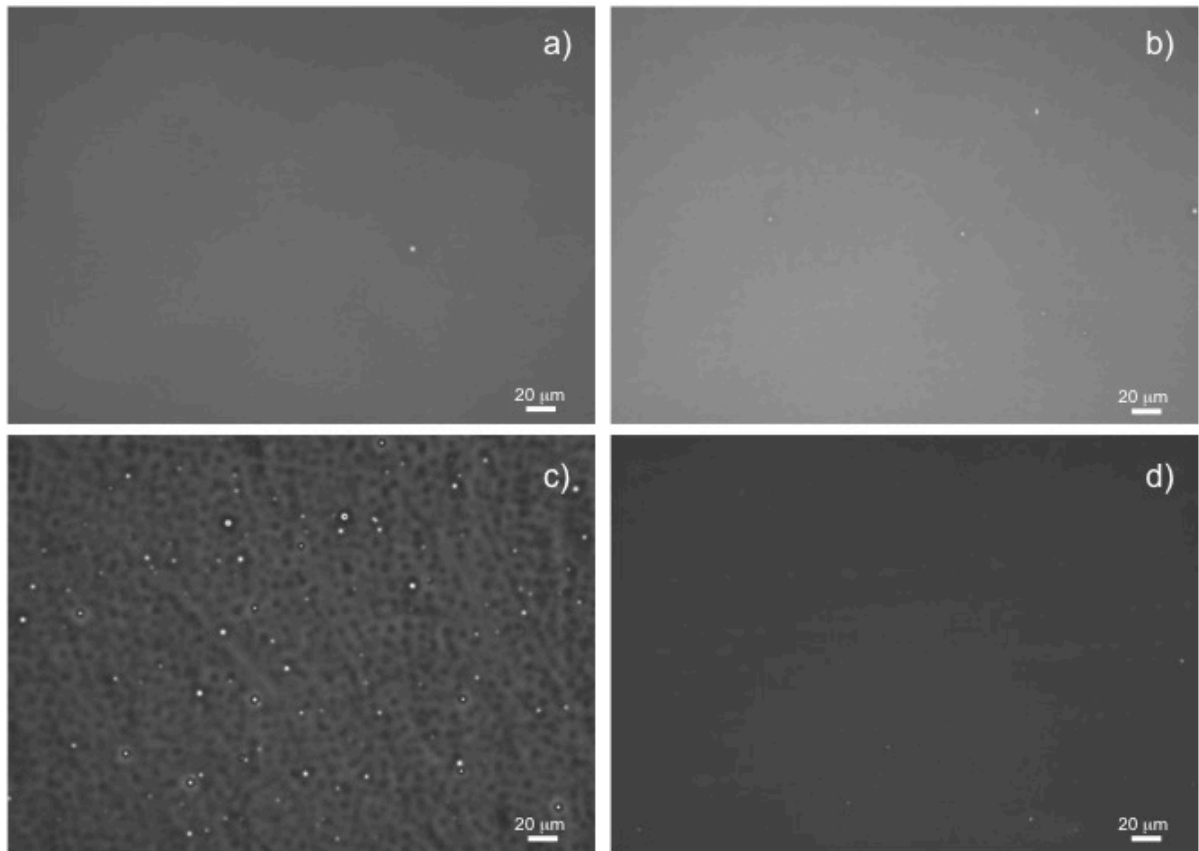


Figure 3.2 Optical micrographs of (a) pure PS204, (b) PS204/CSNG-R378 as cast films on silicon wafers, (c) pure PS204 at 180°C for 80 h, and (d) PS204/CSNG-R378 at 180°C for 80 h. Scale marker is 20 microns.

As seen in Fig. 3.2a-b, according to the optical micrographs of as-cast thin-films of particle-free PS204 and PS204/CSNG-R378 are featureless. Upon annealing to 180°C, particle-free PS204 layer dewets from the substrate (cf. Fig. 3.2c), in agreement with previous studies.⁴ Incorporation of CSNG-R378 into PS204 (20% w/w) enhances the stability of the layer on the silicon wafer significantly(cf. Fig. 3.2d).

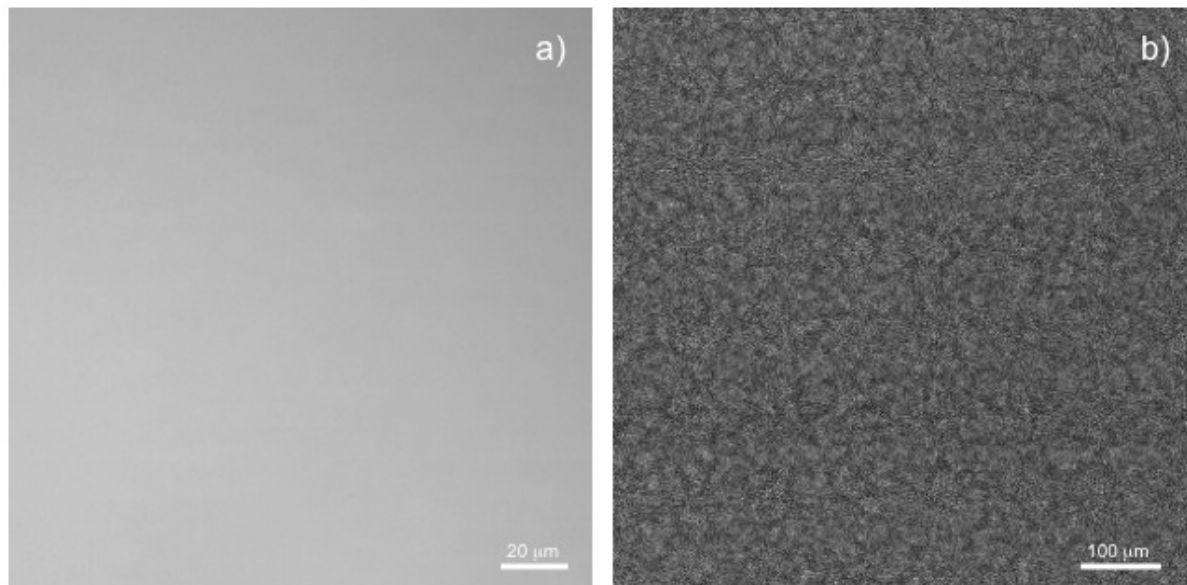


Figure 3.3 48 nm thick pure CSNP-R378 at 180°C for 80 h on silicon wafer (a) optical micrograph at 20x with DIC optics, (b) by scanning electron microscopy in field emission mode, 5 kV at 100,000x.

Optical micrographs of a 48 nm thick CSNG film on silicon wafer shows no evidence of dewetting at 180°C for 80 h (cf. Fig. 3.3a). Field emission scanning electron microscopy imaging of the same sample exhibits a contiguous layer formation (cf. Fig. 3.3b). Preliminary experiments to study the stabilization effect of the CSNGs were performed by another member of the Spontak/Genzer groups, Mr. Xiaojing Cai. The results have demonstrated that after spin-casting, a nearly-monolayer (≈ 10 nm thick, considering the nanoparticle diameter is 13 nm) can be floated onto DI water and remains stable. If the as-spun monolayer is annealed, it cannot be removed easily from the glass slide using a neutral (toluene) or PMMA-selective solvent (acetic acid), indicating a possible interaction of the acrylic core of the particles with the silicon substrate. Continuous efforts have been carried on to fully comprehend this behavior.

In order to study the effect of CSNG structuring at immiscible polymer/polymer interfaces we have switched our attention from single layer systems of PS and PS/CSNG to laminates of PS/PMMA51. Images in Fig. 3.4a-b demonstrate that the surface of silica/PS204/PMMA51 and silica/PS204/CSNG-R/PMMA51 samples are smooth as spun-cast films with a root-mean-square value of 0.216 nm, in agreement with our previous study. Upon annealing above the T_g of the polymers, the sample morphology changes dramatically. The optical micrograph in Fig. 3.4c depicts the topographical patterns generated upon annealing the silica/PS204/PMMA51 bilayer for 80 h at 180°C. The image reveals a complex dewetting pattern, involving significant roughening of the interface, as ascertain by selectively washing off the top PMMA51 layer with acetic acid in order to reveal the underlying topography of the PS204 substrate (cf. Fig. 3.4d). Upon further annealing, the interfacial tension at the PS204/vacuum interface tends to smoothen the rough PS204 surface topographies.

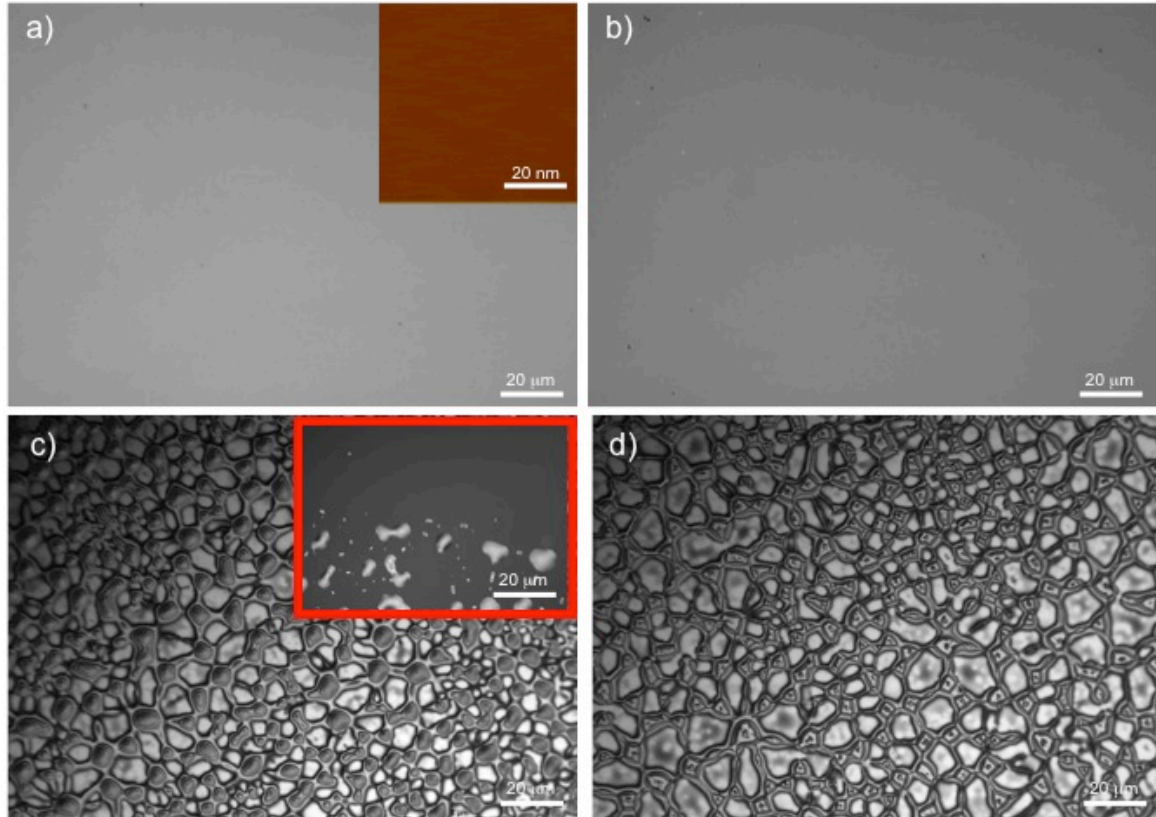


Figure 3.4 Optical micrographs of (a) as-cast film of PS204/PMMA51 on silicon substrate (the inset image is the surface topography scan showing a roughness value of 0.216 nm), (b) as-cast film of PS204/CSNG-R378/PMMA51 on silicon substrate, (c) PS204/CSNG-R378/PMMA51 bilayer at 180°C for 80 h (the inset shows a PS layer dewetting from a PMMA substrate with the evidence of PS islands), and (d) PS204/CSNG-R378/PMMA51 bilayer at 180°C for 80 h after PMMA51 layer was selectively removed with acetic acid.

As a consequence, many topographical features tend to coalesce and the edges of the existing substrate protrusions become more round as the bilayers are further annealed. It is prudent to note that the dewetting in silica/PS204/PMMA51 system differs from that present in silica/PMMA243/PS50 bilayers annealing under identical conditions (cf. inset of Fig. 3.4c). In the latter case the PS50 film seems to dewet selectively from the PMMA substrate without causing any roughening to the PMMA243 substrate. While detailed study of this

behavior is outside the main scope of this study, one can speculate that the “conventional” dewetting behavior seen in silica/PMMA243/PS50 may be associated with a higher stability of the PMMA243 layer on the substrate due to well-documented strong interactions between PMMA and silica.⁵

3.3.2 Effect of CSNG concentration

Xu et al.⁶ have shown that when a four-arm poly(4-vinylbenzyl chloride) (pVBC) star polymer was added into a linear PS film, PS can slip on the substrate. Since the dewetting rate of the linear PS film is faster than that of the four-arm pVBC film on the substrate, the rupture of the films was induced by heterogeneous nucleation and the surface structuring was governed by the concentration of the pVBC in the PS layer. Another study⁷ from the same group has also demonstrated that the star comb-like polymers can increase the resistant force of dewetting with hole growth and inhibit the dewetting process of the thin polymer film by enrichment in the rim. In the literature, polymer-brush coated spheres in polymer matrices have also been studied and it has been demonstrated that the homopolymer molecular weight, as well as that of the brush and grafting density of the brush play an important role in dewetting mechanism and patterns.⁸⁻¹⁶

According to our results, when 1 wt% of low-molecular-weight nanoparticle (CSNG-R263) is added into the homopolymer PS204, the dewetting pattern changes dramatically from that in a nanoparticle-free PS204/PMMA51 bilayer (cf. Fig 3.5a).

After two hours of annealing at 190°C (chosen to accelerate the kinetics relative to that at 180°C), the PMMA51 layer dewets from the PS204/CSNG-R263 support via

nucleation and growth mechanism. The shape of the holes as PMMA51 destabilizes is perfectly circular. The PMMA51-free areas on the sample (i.e., bare PS204/CSNG-R263) remain stable and smooth.

Upon increasing the concentration of CSNG-R263 in the PS204 layer to 10 wt% the dewetting mechanism remains the same; however, interfacial structuring due to nanoparticle aggregation at the PS204/PMMA51 interface affects the hole formation, e.g. the shape of the holes is no longer circular (cf. Fig. 3.5b). Even the PMMA51-free areas exhibit some surface roughness due to either destabilization or nanoparticle presence. Keeping the particle concentration at 10 wt% but changing the particle molecular weight from 263 to 378 kg/mol alters the morphology drastically as seen in Fig. 3.5c. Surface topography imaging of these features, seen in Fig. 3.5c, exhibit the aggregation of the particles and how the structuring develop as the PMMA51 top layer dewets from the PS204/CSPN-R378. The RMS value is 28 nm.

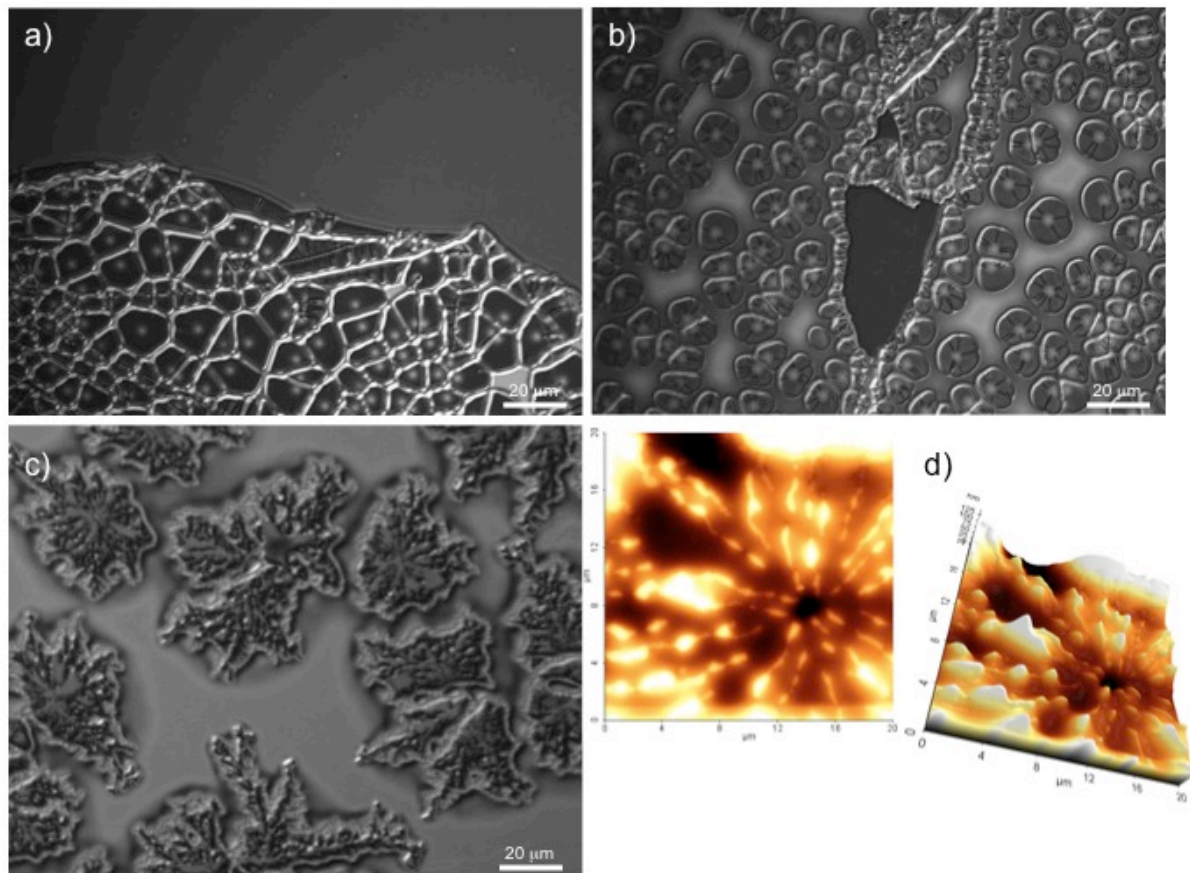


Figure 3.5 Optical micrographs of (a) PS204/CSNG-R263(1wt%)/PMMA51 at 190°C for 2 h, and (b) PS204/CSNG-R263(10 wt%)/PMMA51 bilayer at 190°C for 4 h, (c) (b) PS204/CSNG-R378 (10 wt%)/PMMA51 at 190°C for 16 h and (d) AFM of topography and 3D views of the features displayed in part (c).

Increasing the CSNG-R concentration to 15 wt% results in an intriguing morphology due to dewetting the PMMA51 film (cf. Fig. 3.6a). While the break-up of the PMMA layer commences as a nucleation event, as the hole diameter reaches a certain size “cracks” start propagating from the core with increasing the annealing time. At around 16 hours of annealing, the length of the “cracks” saturates. These final morphologies resemble spider- or octopus-like objects, albeit more complex. A chain-like structure of nanoparticle aggregates

in PMMA51-free areas (cf. Fig. 3.6b) suggests that interfacial structuring might be responsible for intriguing morphologies seen in sample areas coated with PMMA51.

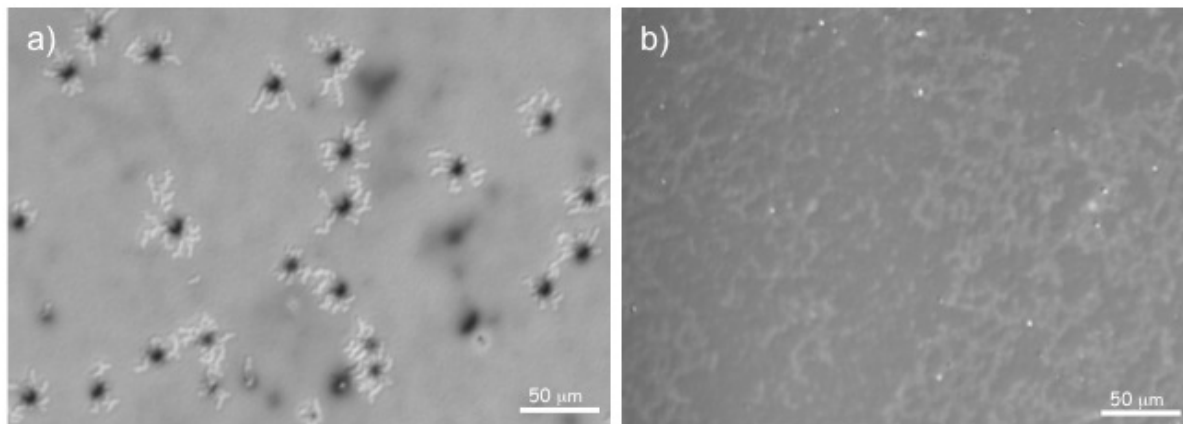


Figure 3.6 Optical micrographs of (a) PS204/CSNG-R263(15wt%)/PMMA51 at 180°C for 39 h and (b) PMMA51-free areas of the PS204/CSNG-R263 substrate at 180°C for 39 h and the sample was treated in acetic acid for 4.5 h.

Figure 3.6 depicts a few examples of optical micrographs collected from samples after stripping the top PMMA51 film with acetic acid, illustrating the presence of “tentacle-like” protrusions that originate from a central point and develop in fractal-like fashion into the plane of the interface. As shown by the image in Figure 3.6b, this interfacial structuring is quite pronounced in areas of a discontinuity in the PMMA51 layer.

As seen in Fig. 3.7d, the tentacle-like structures represent protrusions present on the top PS204/CSNG film. The roughness increases from 27 to 34 nm as the particle loading is increased from 10 to 15 wt%. We believe that as the particles form aggregates and lateral structures occur in-plane as the top PMMA layer dewets from the substrate. Koneripalli et al.¹⁷ have also observed similar fractal patterns in their studies on strained block copolymer films. Other studies on hole-growth instability in dewetting of thin films¹⁸ in which rapidly

growing holes became unstable and formed non-equilibrium patterns resembling fingering patterns, called Hele-Shaw,¹⁹ that arise when injecting air into a liquid between two closely spaced plates.

At around 20 wt% concentration, the particle loading is sufficient enough to stabilize the top layer.

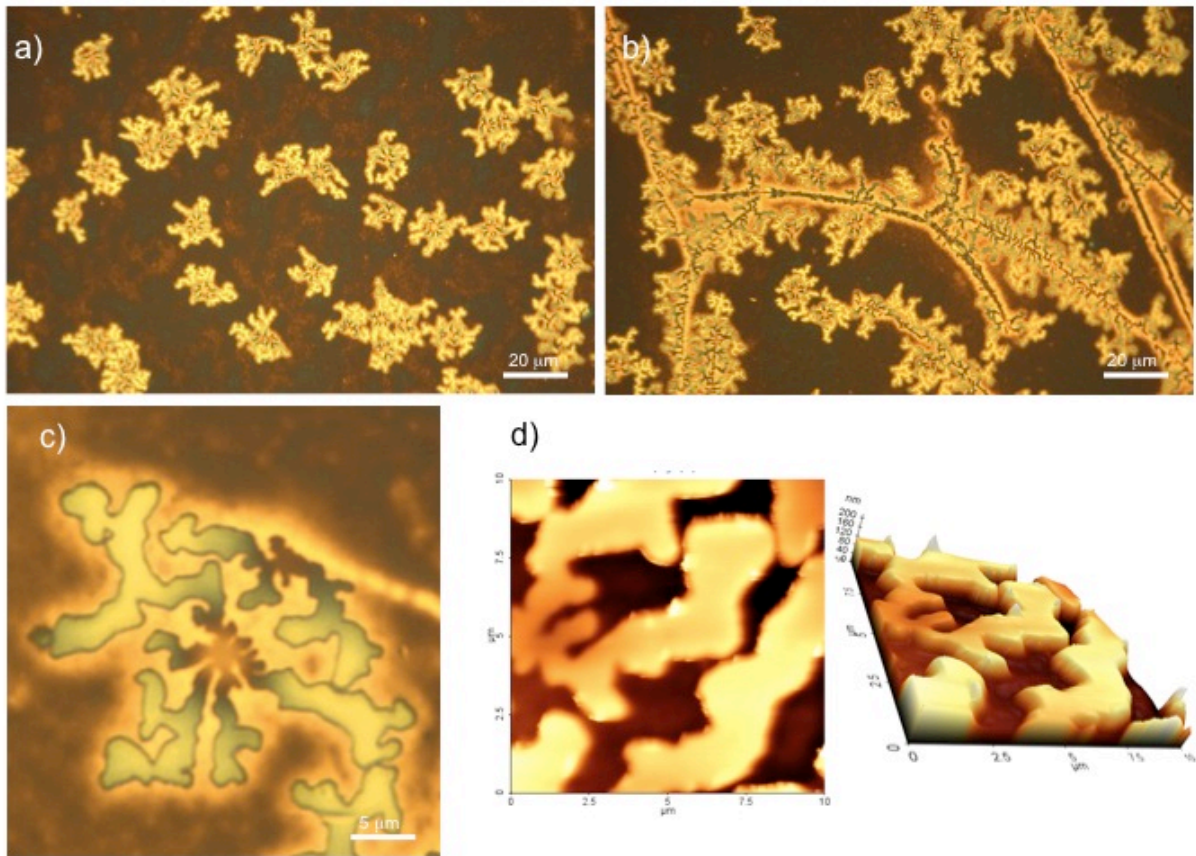


Figure 3.7 Optical micrographs of PS204/CSNG-R263(15wt%)/PMMA51 taken at 50x magnification with RGB optics. The sample was treated at 180°C for 39 h, and, then was immersed in acetic acid for 27 h to remove the PMMA51 top layer. (d) AFM of topography and 3D views of the tentacle-like structures displayed in part (c).

While the data presented in Fig. 3.7 represented morphologies observed in specimens with CSNG-R263, in the following discussion we concentrate on samples that employed CSNG-R378. Generally speaking, the types of behavior seen in both sets of samples are similar. However, some subtle differences do exist. For instance, as seen in Figure 3.8a, interconnected chains of microsize “octopi” cover the entire area of the sample as the concentration of CSNG-R378 is increased to 20wt%. PMMA51 layers with parallel imperfections (introduced presumably during the floating process) result in organized “octopus troops” lined-up in a well-defined direction. At 16 hours of annealing the sizes of the “tentacles” observed in silica/PS204/CSNG-R378/PMMA51 samples was longer than that in silica/PS204/CSNG-R263/PMMA51 (cf. Fig. 3.7b).

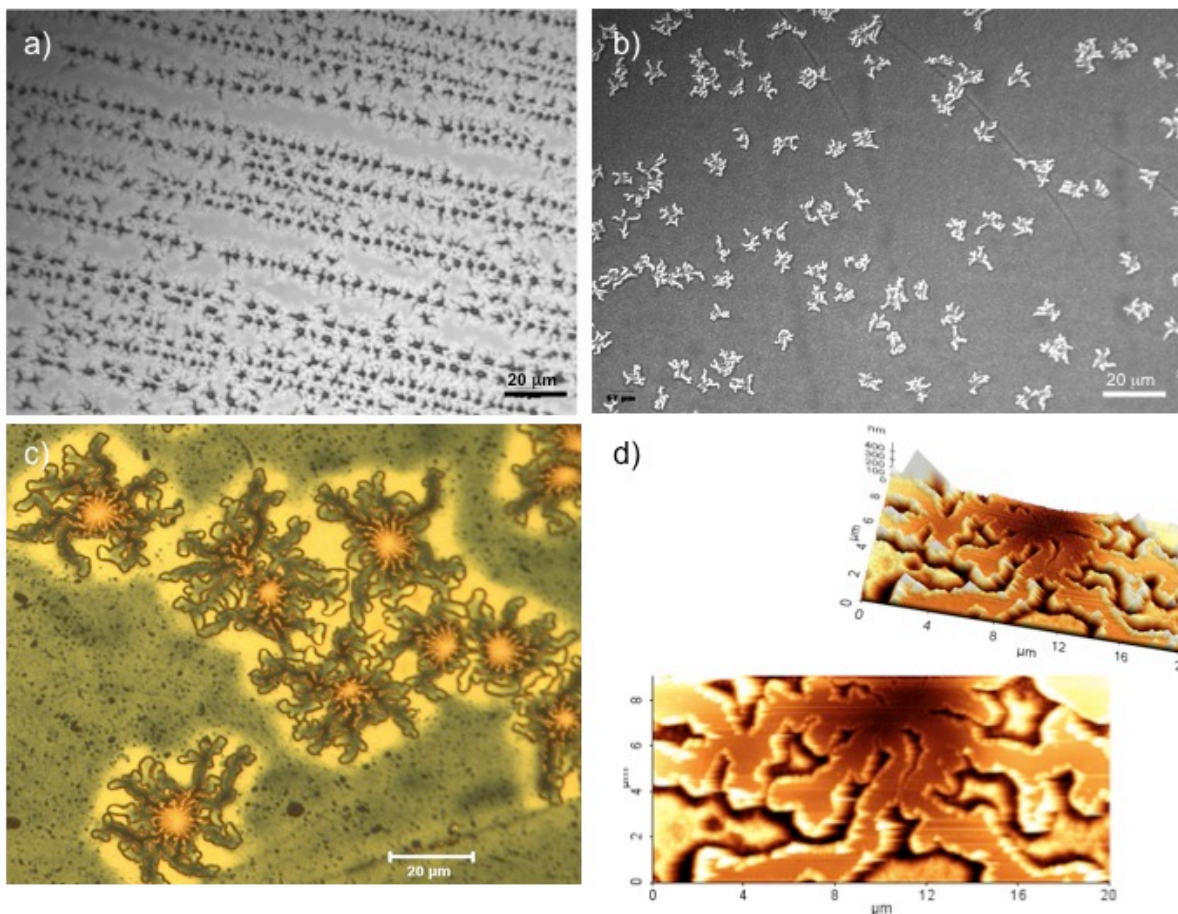


Figure 3.8 Optical micrographs of PS204/CSNG-R378 (15wt%)/PMMA51 at 190°C for 16 h taken at 20x magnification with DIC optics, and, then was immersed in acetic acid for (b) 1 h and (c) 27 h, to remove the PMMA51 top layer. AFM topography imaging was performed on the tentacle-like structures as shown in part (d).

As seen in Fig. 3.8d, the tentacle-like structures are protrusions on the top PS204/CSNG film. AFM images confirm that these features consist of 3D ridges and valleys. We believe that as the particles form aggregates and lateral structures occur at the interface as the top PMMA layer dewets from the substrate.

In addition, unlike for the CSNG-R263 specimens, where visible presence of the “octopus-like” morphologies saturated after 16 hours of annealing, samples with CSNG-

R378 exhibited additional growth of the “tentacles” at longer annealing times and eventually filled the area of the PS204 substrate (cf. Fig. 3.9).

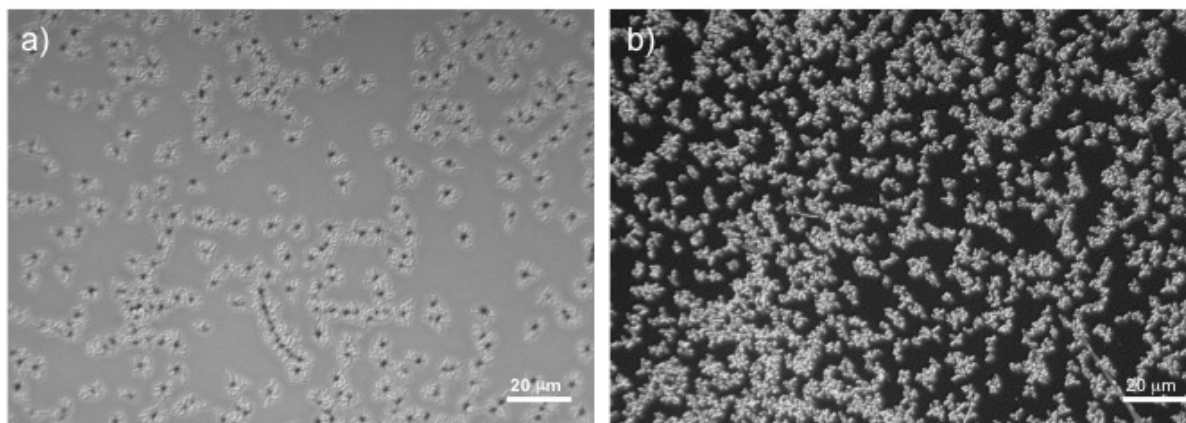


Figure 3.9 Optical micrographs of PS204/CSNG-R378(20wt%)/PMMA51 at 180°C for 80 h taken at 20x magnification with DIC optics, and, then (b) was immersed in acetic acid for 24 h to remove the PMMA51 top layer.

3.3.3 Effect of PS homopolymer molecular weight

In order to explore the effect of matrix molecular weight on interfacial structuring, homopolymer PS849 was utilized as the matrix for both CSNG-R263 and CSNG-R378. Varying the molecular weight of the matrix material was expected to influence both the dynamics of the system and the tendency of the CSNG-R to segregate towards the PS/PMMA interfaces. Due to the difference in viscosities (more than 2 orders of magnitude), the PS204 chains are more mobile relative to those of PS849; this allows the CSNG-Rs to migrate to the PS204/PMMA51 interface much faster relative to the PS849/PMMA51 system. Concurrently, raising the molecular weight of the matrix polymer increases the

driving force for the CSNG-Rs to segregate from the high molecular weight matrix towards the PS/PMMA interface due to entropy-driven autophobicity.

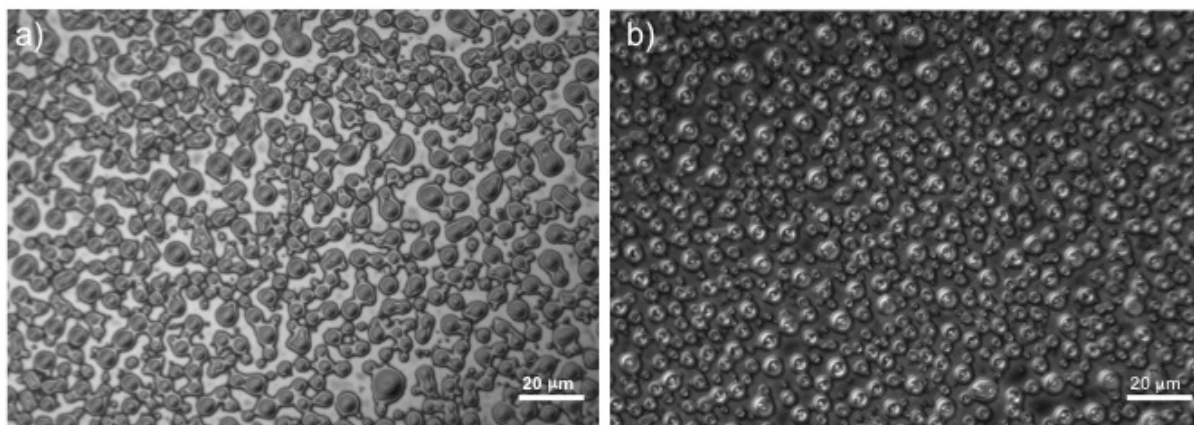


Figure 3.10 Optical micrographs of PMMA51 dewetting from PS879 at 180°C for 80 h taken at 20x magnification with DIC optics, and, then (b) was immersed in acetic acid for 4 h to remove the PMMA51 top layer.

As cast PS849/PMMA51 samples are smooth. Upon annealing at 180°C for 80 hours, the top PMMA51 layer dewets leaving the bottom PS849 substrate flat (cf. Fig. 3.10). Recall that this behavior is different from that seen when PS206 was used as a “substrate”, where complex interfacial roughening was observed (cf. Fig. 3.4c). It is also clear that PMMA51 dewets from the PS879 substrate by the nucleation and growth dewetting mechanism.

When only 1 wt% low-molecular-weight CSNG-R263 is added to the PS879 matrix, the hole formation is disturbed by interfacial structuring; the evidence is profound after 2 hours of annealing at 180°C (cf. Fig. 3.11).

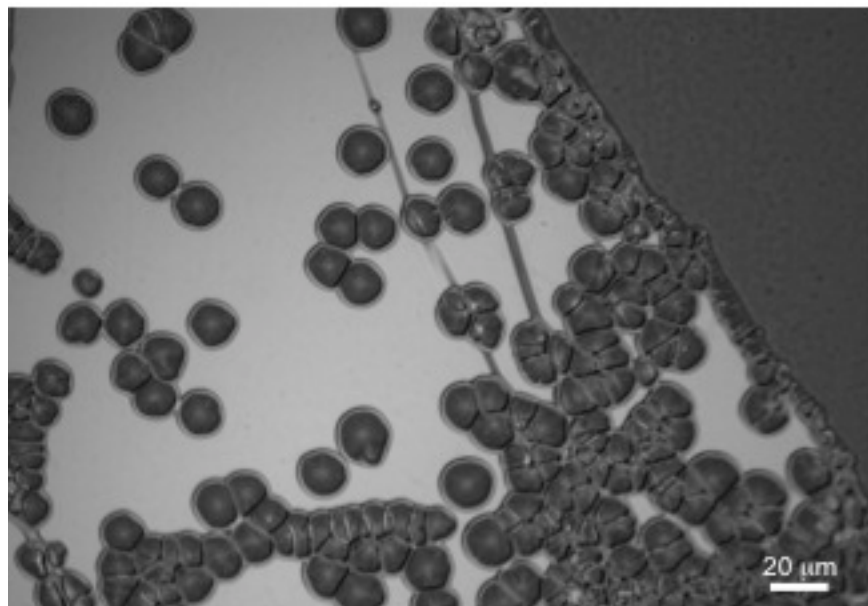


Figure 3.11 Optical micrograph of PS879/CSNG-R263(1wt%)/PMMA51 at 190°C for 2 h.

Recalling a similar type of hole formation (clover-leaf-like) from Fig 3.5b; these two systems differ in particle concentration and PS homopolymer molecular weight that are incorporated into. In the earlier system (cf. Fig. 3.5b), 10 wt% CSNG-R263 was added in PS204, whereas, very similar interfacial structures are achieved by adding only 1 wt% of the same particles in PS879. While quantitative interpretation of this effect needs to be performed, the trends are clear. On the one hand, adding CSNG-R into high molecular weight matrices increases the particle propensity to segregate from the matrix relative to lower molecular weight matrix. On the other hand, the segregation kinetics also slows down considerably due to the increase in the molecular weight of the matrix polymer. Clearly, the interplay between the molecular weight and the concentration of CSNG-R on the segregation kinetics involves complex molecular phenomena. The presence of CSNG-R263 in the PS849 matrix also results in instability even at very low concentrations of CSNG-R in PS849. Note

that in our previous study¹ have shown that the particles cannot break through the layer surface due to the high surface energy barrier at the surface even though the particle arms are autophobic with the parent homopolymer.

Upon increasing the concentration of CSNG-R263 in the PS849 matrix from 1 to 5 wt%, we observe the previously seen dewetting mechanism - namely, the nucleation and growth driven instability (cf. Fig 3.12a-b). Once the CSNG-R particle concentration exceeds 15 wt%, the dewetting mechanism changes dramatically. With CSNG-R378 we start seeing the same spider- or octopus-like structures we have observed previously with the PS204/CSNG-R263 systems at 15wt% of particle concentration. RGB optics with 100x magnification reveals these particle aggregates, as shown in Fig. 3.12c. After 40 hours of annealing at 190°C, the structures measure around 40 microns in diameter.

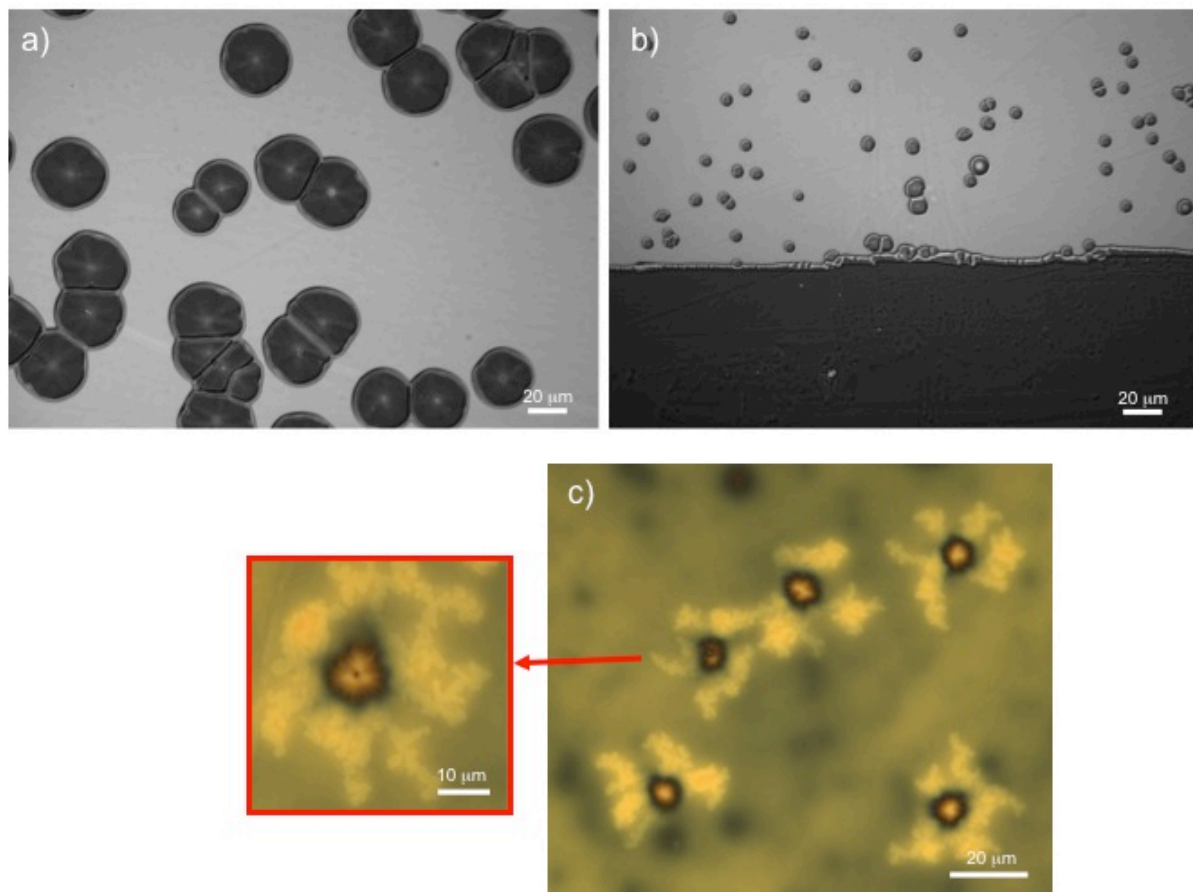


Figure 3.12 Optical micrographs of PS879/CSNG-R378/PMMA51: (a) 1wt% CSNG-R378 loading at 190°C for 2 h, (b) 5wt% CSNG-R378 loading at 190°C for 3.5 h (c) 15wt% CSNG-R378 loading at 190°C for 40 h.

3.4 Summary

In conclusion, our results have demonstrated the stabilization effect of CSNGs with 20 wt% loading on PS homopolymer layers at long annealing times at 180°C. As the particle concentration increases lateral structuring of the particles at the interface develops as evidenced by non-spherical shapes of the rims of dewetted holes. Both particle concentration and particle molecular weight have an effect on interfacial structuring. Annealing of a

laminate with ≈ 15 wt% particle concentration, tentacular structures occur in-plane and dewetting rate slows down substantially. Optical microscopy images of the interface of a PMMA51/PS204 +15 wt% CSNG laminate (with the PMMA top layer removed by acetic acid) after long-time annealing at 190°C exhibit the tentacular features. AFM images confirm that these features consist of ridges and valleys. We attribute this behavior to the intra-molecular organization and lateral structuring of CSNG-R aggregates at the PMMA/PS interface. Nanoparticle aggregates, not individual nanoparticles, could be clearly seen to migrate to the PS/PMMA interface, forming network-like aggregates. This behavior not only supports our earlier findings on segregation with reverse-type nanoparticles (CSNGs) but also can be attributed to the intra-molecular interactions between particle arms.

References

1. Wei, B.; Gurr, P.A.; Gozen, A.O., Blencowe, A., Solomon, D.H., Qiao, G.G.; Spontak, R.J.; Genzer, J. Autophobicity-driven surface segregation and patterning of core-shell microgel nanoparticles *Nano Letters* **8**, 3010-3016 (2008).
2. Ho, A. K.; Iin, I.; Gurr, P. A.; Mills, M. F.; Qiao, G. G. . Synthesis and characterization of star-like microgels by one-pot free radical polymerization *Polymer* **46**, 6727-6735 (2005).
3. Krishnan, R. S.; Mackay, M. E.; Hawker, C. J.; Horn, B. V. Langmuir. Influence of molecular architecture on the dewetting of thin polystyrene films. *Langmuir* **21**, 5770-5776 (2005).
4. Reiter, G. Dewetting of thin polymer films. *Phys. Rev. Lett.* **68**, 75-78 (1992).
5. Coulon, G.; Russell, T.P.; Deline, V.R.; Green, P.F. Surface-Induced Orientation of Symmetric, Diblock Copolymers: A Secondary Ion Mass Spectrometry Study. *Macromolecules*, 2581-2589 (1989).
6. Xu, L.; Yu, X. F.; Shi, T. F.; An, L. J. Dewetting of linear polymer/star polymer blend film. *Macromolecules* **41**, 21-24 (2008).
7. Xu, L.; Yu, X. F.; Shi, T. F. & An, L. J. Investigation of the dewetting inhibition mechanism of thin polymer films. *SOFT MATTER* **5**, 2109-2116 (2009).
8. Harton, S. E.; Kumar, S. K. Mean-field theoretical analysis of brush-coated nanoparticle dispersion in polymer matrices. *Journal of Polymer Science Part B-Polymer Physics* **46**, 351-358 (2008).
9. Lan, Q.; Francis, L. F.; Bates, F. S. Silica nanoparticle dispersions in homopolymer versus block copolymer. *Journal Of Polymer Science Part B-Polymer Physics* **45**, 2284-2299 (2007).
10. Matsen, M. W.; Gardiner, J. M. Autophobic dewetting of homopolymer on a brush and entropic attraction between opposing brushes in a homopolymer matrix. *Journal Of Chemical Physics* **115**, 2794-2804 (2001).
11. Ohno, K.; Morinaga, T.; Koh, K.; Tsujii, Y.; Fukuda, T. Synthesis of monodisperse silica particles coated with well-defined, high-density polymer brushes by surface-initiated atom transfer radical polymerization. *Macromolecules* **38**, 2137-2142 (2005).

12. Smith, G. D.; Bedrov, D. Dispersing Nanoparticles in a Polymer Matrix: Are Long, Dense Polymer Tethers Really Necessary? *Langmuir* **25**, 11239-11243 (2009).
13. Wang, X. R.; Foltz, V. J.; Rackaitis, M.; Bohm, G. G. A. Dispersing hairy nanoparticles in polymer melts. *Polymer* **49**, 5683-5691 (2008).
14. Xu, C.; Ohno, K.; Ladmiral, V.; Composto, R. J. Dispersion of polymer-grafted magnetic nanoparticles in homopolymers and block copolymers. *Polymer* **49**, 3568-3577 (2008).
15. Xu, J. J.; Qiu, F.; Zhang, H. D.; Yang, Y. L. Morphology and interactions of polymer brush-coated spheres in a polymer matrix. *Journal of Polymer Science Part B-Polymer Physics* **44**, 2811-2820 (2006).
16. Corbierre, M. K.; Cameron, N. S.; Sutton, M.; Laaziri, K.; Lennox, R. B. Gold nanoparticle/polymer nanocomposites: Dispersion of nanoparticles as a function of capping agent molecular weight and grafting density. *Langmuir* **21**, 6063-6072 (2005).
17. Koneripalli, N.; Bates, F. S.; Fredrickson, G. H. Fractal hole growth in strained block copolymer films. *Physical Review Letters* **81**, 1861-1864 (1998).
18. Gu, X.; Raghavan, D.; Douglas, J. F.; Karim, A. Hole-growth instability in the dewetting of evaporating polymer solution films. *Journal of Polymer Science Part B-Polymer Physics* **40**, 2825-2832 (2002).
19. Benjacob, E.; Garik, P. The Formation Of Patterns In Nonequilibrium Growth. *Nature* **343**, 523-530 (1990).

CHAPTER 4: Mean-field phase behavior of triblock copolymers varying in molecular asymmetry

4.1 Introduction

While immiscible homopolymers commonly undergo phase separation at macroscopic length scales, incorporation of a covalent linkage between two such homopolymers to form a diblock copolymer can have dramatic consequences at significantly reduced length scales. In the case of block copolymers composed of A and B repeat units, the *classical* equilibrium morphologies observed to date include A(B) spheres positioned on a body-centered cubic (bcc) lattice in a B(A) matrix, A(B) cylinders arranged on a hexagonal lattice in a B(A) matrix (H) and co-alternating lamellae.¹ Examples of non-classical, or complex morphologies reported for neat bicomponent (AB or ABA) block copolymers include the gyroid,²⁻⁶ perforated lamellar⁷⁻¹¹ and "Plumber's Nightmare"^{12,13} morphologies. Such tunable morphological variation is of keen interest in emerging nanotechnologies^{14,15} and reflects entropic differences associated with interfacial chain packing,¹⁶ which can be systematically altered by synthesizing block copolymer molecules differing in composition, repeat unit asymmetry.¹⁷

Another strategy developed to increase the versatility of diblock copolymers is the addition of a third block to a diblock copolymer, forming a triblock copolymer. Incorporation of a chemically dissimilar third (C) block results to a (AB) diblock copolymer can increase the accessible morphologies by varying relative block lengths and interblock incompatibility.¹⁸⁻²¹ If the third block is chemically identical to the first, the result in an ABA triblock copolymer, which exhibits the same morphologies as its parent AB diblock^{22,23} but

markedly different mechanical and flow properties.²⁴ The primary reason for these differences is that the third block may locate in either the same microdomain as the first so that the B midblock forms a loop or in a different microdomain so that the midblock forms a bridge. Several experimental²⁵⁻²⁷ and theoretical^{23,28,29} studies have examined the consequences of midblock bridging (and network formation) in ABA triblock copolymer systems, but, to the best of our knowledge, a systematic analysis of molecularly asymmetric A_1BA_2 triblock copolymers has yet to be reported in the literature. The pioneering studies on A_1BA_2 triblock copolymers in the weak-segregation limit by Mayes and Olvera de la Cruz^{30,31} and, later, by Dobrynin and Erukhimovich³² have provided evidence that molecular asymmetry can have a profound effect on both order-disorder and order-order transitions. More recently, Matsen³³ has used self-consistent field theory (SCFT) to show that such molecular asymmetry can alter microdomain dimensions and order-order transitions due to the presence of short A_2 blocks that remain mixed upon microphase-ordering of the A_1 and B blocks.

The objective of the present work is to investigate the influence of molecular asymmetry on the order-disorder transition temperature (T_{ODT}) in two series of copolymers in which the A_2 block is progressively grown from parent A_1B diblock copolymers differing in composition and molecular weight.

4.2 Experimental

4.2.1 Materials

Two poly(styrene-*b*-isoprene) A₁B diblock copolymers were independently synthesized via living anionic polymerization in cyclohexane at 60°C with *sec*-butyllithium as the initiator. The molecular characteristics of the diblock copolymers and triblock copolymers chemically grown from the diblocks by subsequent living anionic polymerization were measured by ¹H NMR and GPC. The first copolymer series, designated 9-46-A₂, was generated from a diblock copolymer with block masses of 9400 (styrene, A₁) and 46000 (isoprene, B), whereas the second series, denoted 9-17-A₂, employed a parent diblock copolymer with block masses of 8800 (A₁) and 17000 (B). The maximum polydispersity index measured in both triblock copolymer series was determined from GPC to be 1.04.

4.2.2 Methods

4.2.2.1 Rheological characterization

Specimens for rheometry were prepared by compression molding a platen approximately 1.2 mm thick of each copolymer. Discs measuring 30 mm in diameter were punched from each platen and heated to 170°C under vacuum for 2 h. The materials, then, were cooled to ambient temperature under vacuum. Dynamic shear measurements were conducted using an ARES strain-controlled rheometer equipped with 25 mm parallel plates separated by a 1 mm gap. Linear viscoelastic regime for each series (LVE) was determined by dynamic strain sweeps and occurred to be occurred at up to 2-5% strain amplitude at 160°C. All subsequent

measurements used lower strain levels to ensure that linear viscoelasticity was maintained. The T_{ODT} of each copolymer under investigation was established from precipitous reductions in the dynamic elastic (G') and viscous (G'') moduli during isochronal temperature sweeps performed at heating rates of 1 and 5°C/min at a frequency of 1 rad/s. Dynamic frequency sweeps were performed from 10^{-1} to 10^2 rad/s at 2% strain at selected temperatures for additional validation of the G' vs. G'' crossplots.

4.2.2.2 Mean-field phase behavior

Molecular asymmetry in an A_1BA_2 triblock copolymer can be taken into account by introducing an asymmetry parameter (τ), defined as the fraction of A units comprising the A_1 block. The number of A units in the A_1 block (N_{A1}) is written as

$$\tau f_A N \quad (1)$$

where f_A is the total number fraction of A units in the A_1BA_2 triblock. Conversely, the number of A units in the A_2 block (N_{A2}) is given by

$$(1 - \tau) f_A N \quad (2)$$

so that τ can be alternatively expressed as

$$f_{A1}/f_A \quad (3)$$

where f_{A1} is the number fraction of A units in the A_1 block. When $\tau = 1$, the triblock copolymer reduces to a diblock copolymer. When, on the other hand, $\tau = 1/2$, the triblock copolymer possesses endblocks of equal mass and becomes molecularly (although not necessarily compositionally) symmetric.

In order to fully comprehend the direct relationship between the experimental measurements and the theoretical predictions, first, we needed to consider the difference between A and B mass density in describing the molecular characteristics of each copolymer (i.e., N , f_A and τ), putting the number of A and B repeat units on a common density basis. It immediately follows that N_i ($i = A_1, B$ or A_2) is given by

$$(M_i/m_i)(\rho_i/\rho_0) \quad (4)$$

where m_i is the molecular mass of repeat unit i , ρ_i is the mass density of i (taken as 1.04 and 0.913 g/cm³ for polystyrene and polyisoprene, respectively), and ρ_0 is the geometric-mean reference density. The second requisite relationship is an expression for $\chi(T)$. For this purpose, we use the result reported by Lodge et al.³⁴ for poly(styrene-*b*-isoprene) diblock copolymers in which $\chi = 33.0/T - 0.0228$. Interblock incompatibility is expressed in terms of χN , where χ is the temperature-dependent Flory-Huggins interaction parameter and N is the number of statistical units along the copolymer backbone).

Since values of T_{ODT} determined from the predicted $(\chi N)_{ODT}$ in Fig. 4.2b are sensitive to the coefficients used to describe $\chi(T)$ and since we are primarily interested in determining whether mean-field theory accurately predicts the minimum observed in $T_{ODT}(\tau)$, we have elected to normalize $T_{ODT}(\tau)$ with respect to $T_{ODT}(\tau = 1)$. Reduced T_{ODT} (denoted $T_{ODT,r}$) values obtained in this fashion are presented as functions of τ and f_A in Figs. 4.3a and 4.3b, respectively (Appendix 4: Fortran code for mean-field phase behavior algorithm).

4.3 Results and discussion

Values of T_{ODT} are presented as a function of the growing A_2 block mass (M_{A_2}) for both copolymer series in Fig. 4.1. While T_{ODT} is anticipated to increase with increasing copolymer molecular weight due to greater interblock incompatibility (expressed in terms of χN , where χ is the temperature-dependent Flory-Huggins interaction parameter and N is the number of statistical units along the copolymer backbone), this expected trend does not become evident in Fig. 4.1 until the A_2 block is of comparable size to or larger than the A_1 block.

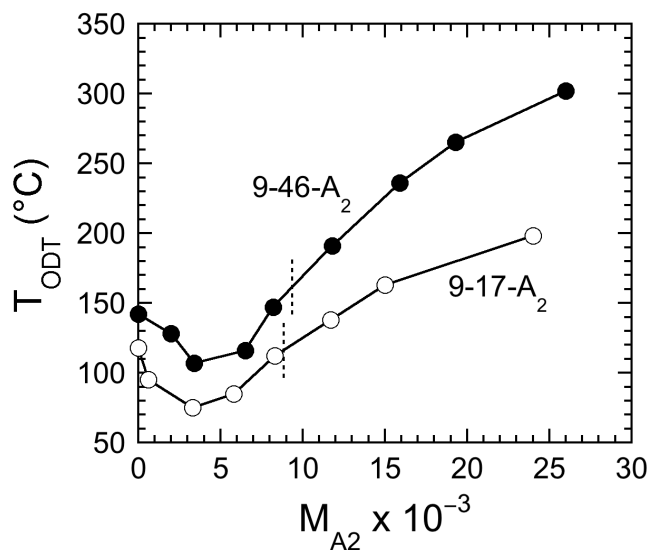


Figure 4.1. Dependence of the order-disorder transition temperature (T_{ODT}) measured by dynamic rheology on the mass of the growing A_2 endblock (M_{A_2}) in the 9-46- A_2 (●) and 9-17- A_2 (○) triblock copolymer series (see the text for details). The solid lines connect the data, and the dotted vertical lines identify the conditions corresponding to molecularly symmetric triblock copolymers wherein $M_{A_1} = M_{A_2}$.

At shorter A_2 block lengths, however, T_{ODT} is depressed, exhibiting a clearly discernible minimum in both copolymer series. The measured reduction in T_{ODT} relative to the parent diblock copolymer is nontrivial: 35°C in the 9-46- A_2 series and 43°C in the 9-17- A_2 series. This signature feature in both copolymer series must also be considered in light of the A_2 -induced change in copolymer composition. That is, an increase in the composition of the minority block in an ordered block copolymer (f_A) is generally accompanied by a net decrease in χN and, consequently, an increase in T_{ODT} . Thus, the concurrent increases in M_{A_2} and f_A in the two copolymer series displayed in Fig. 4.1 would naïvely favor monotonic increases in T_{ODT} . To explain the observed minimum in T_{ODT} , we turn our attention to the mean-field theory proposed by Mayes and Olvera de la Cruz^{30,31}, in which $(\chi N)_{ODT}$ is presented as a function of t for copolymers differing in molecular composition (f_A). The values of $(\chi N)_{ODT}$ provided in Fig. 4.2a correspond to the lowest order-disorder transition condition identified for the lamellar, hexagonal cylindrical and body-centered-cubic spherical morphologies. In all the cases examined, $(\chi N)_{ODT}$ is observed to decrease with increasing τ from $\tau = 1/2$ to $\tau = 1$. This predicted behavior is symmetric around $\tau = 1/2$, and the extent of reduction in $(\chi N)_{ODT}$ with increasing τ is more pronounced for compositionally asymmetric copolymers. It is important to recognize that, for f_A to remain constant with varying τ , N_{A_1} must decrease commensurate with an increase in N_{A_2} . Although this scenario differs from the present experimental study, the predictions shown in Fig. 4.2a can be compared with the SCFT predictions of Matsen³³ and demonstrate that the ODT in molecularly asymmetric triblock copolymers is sensitive to both τ and f_A . Predictions of $(\chi N)_{ODT}(\tau)$ for the two copolymer series investigated here are displayed in Fig. 4.2b and reveal a more complex

dependence on t since f_A increases with decreasing τ . In both cases, however, a maximum in $(\chi N)_{ODT}$ is apparent, which indicates that T_{ODT} is predicted to exhibit a minimum, in accord with the experimental findings provided in Fig. 4.1.

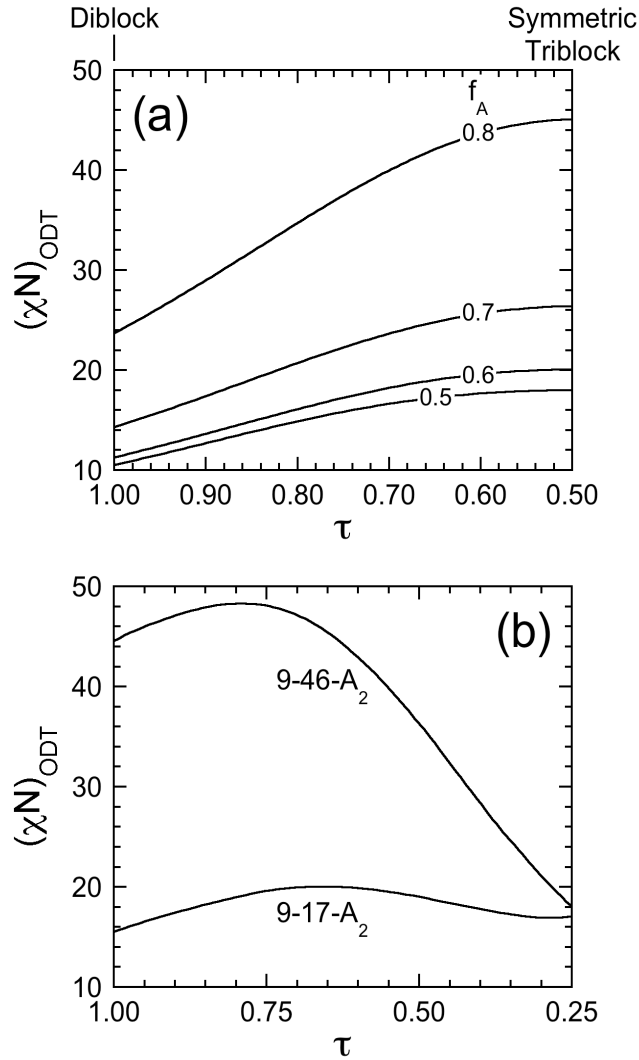


Figure 4.2. Values of $(\chi N)_{ODT}$ presented as a function of molecular asymmetry (τ) as predicted from the mean-field theory of Mayes and Olvera de la Cruz^{30,31} for two asymmetric triblock copolymer designs: (a) fixed molecular composition (f_A) and (b) variable molecular composition. Corresponding values of f_A are listed in (a), and the two copolymer systems under investigation (see the text for details) are labeled in (b).

In Fig. 4.3a, the normalized ODT measurements from both copolymer series are consistent, and mean-field theory predictions for the 9-17-A₂ series are observed to be in generally favorable agreement with the experimental data.

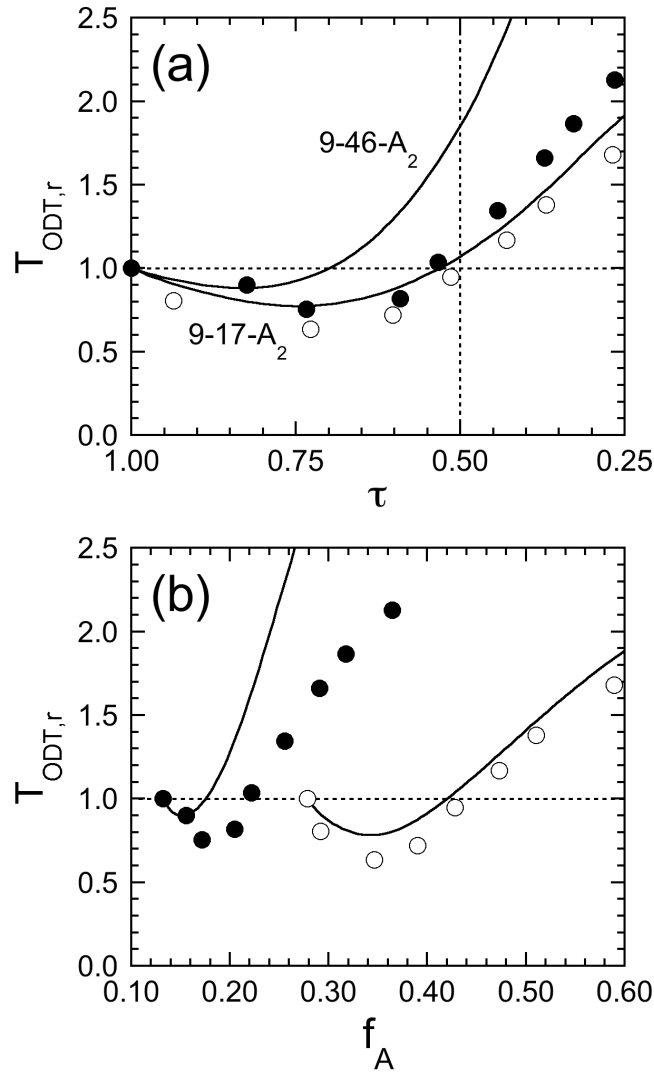


Figure 4.3. Values of T_{ODT} for the 9-46-A₂ (●) and 9-17-A₂ (○) triblock copolymer series normalized with respect to T_{ODT} for the parent diblock copolymer ($\tau = 1$) in each series and presented as functions of (a) molecular asymmetry (τ) and (b) molecular composition (f_A). The solid lines are mean-field theory predictions used in conjunction with $\chi(T)$ reported by Lodge et al.³⁴ The dotted lines identify the conditions corresponding to $\tau = 0.5$ (a) and $T_{ODT,r} = 1$ (a and b).

Similar agreement between theory and experiment is evident in Fig. 4.3b. Predictions for the more compositionally asymmetric 9-46-A₂ series tend to overpredict $T_{ODT,r}$ (due to the normalization scheme adopted here), but nonetheless exhibit a discernible minimum in $T_{ODT,r}$. Regressions of the mean-field $(\chi N)_{ODT}$ predictions displayed in Fig. 4.2b to the non-normalized $T_{ODT}(\tau)$ values measured from both copolymer series are included for comparison in Fig. 4.4. The fitted curves accurately describe the two datasets and yield the following expressions for $\chi(T)$: $52.6/T - 0.0739$ for the 9-46-A₂ series and $35.0/T - 0.0445$ for the 9-17-A₂ series.

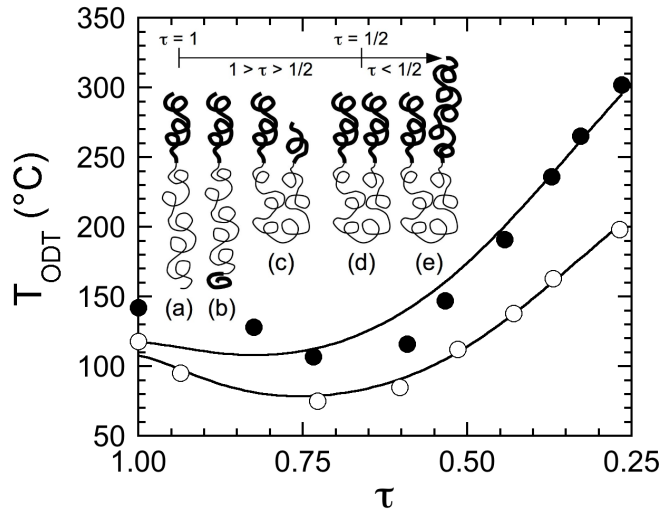


Figure 4.4 Dependence of T_{ODT} on t for the 9-46-A₂ (●) and 9-17-A₂ (○) triblock copolymer series. The solid lines represent fits of the mean-field predictions displayed in Fig. 2.2b to both datasets. The inset is a schematic illustration depicting the chain conformations associated with the transformation of an A₁B diblock copolymer (a) to an A₁BA₂ triblock copolymer (b-e). A relatively short A₂ block initially remains mixed with the B midblock (b). As the length of the A₂ block is further increased, it microphase-separates to form a bidisperse brush with the A₁ block (c). When $\tau = 1/2$, the triblock copolymer becomes molecularly symmetric in which case the lengths of the A₁ and A₂ endblocks are identical (d). A further increase in the length of the A₂ block ($\tau < 1/2$) is accompanied by a bidisperse brush and an order-disorder transition governed by the A₂ block (e).

While previous studies have reported that c can be composition-dependent and we implicitly neglect fluctuation corrections, it is comforting that the $\chi(T)$ coefficients determined from Fig. 4.4 are comparable to those reported by Lodge et al.³⁴

The unequivocal agreement between mean-field theory and experimental data evident in Figs. 4.3 and 4.4 provides confidence that T_{ODT} initially decreases as the A_2 block is grown onto a diblock copolymer. This reduction can be explained in terms of block segregation and stretching, following the arguments of Matsen³³ and schematically depicted in the inset of Fig. 4.4. Upon microphase-ordering, the constituent blocks of a diblock copolymer (at $\tau = 1$) become stretched to relieve unfavorable interactions and promote chain packing along the A/B interface (Fig. 4.4a). Incorporation of a short A_2 block results in mixing between the A_2 and B blocks, which permits the stretched B midblock to relax (Fig. 4.4b), thereby lowering T_{ODT} . As the length of the A_2 block is increased further, it eventually reaches a point where it also microphase-separates from the B block and joins the A_1 block to form a bidisperse brush composed of long A_1 blocks and short A_2 blocks (Fig. 4.4c). Milner and Witten³⁵ have shown that the stretching energy of a bidisperse brush is less than that of its monodisperse analog, and so T_{ODT} of a molecularly asymmetric A_1BA_2 triblock copolymer with $\tau > 1/2$ remains less than that of the parent A_1B diblock copolymer. This effect systematically diminishes as the length of the A_2 block approaches that of the A_1 block at $\tau = 1/2$ (Fig. 4.4d). Once the A_2 block is longer than the A_1 block (and $\tau < 1/2$), T_{ODT} is dictated by the longer A_2 block comprising the bidisperse A_1+A_2 brush so that $T_{ODT,t}$ exceeds unity in Fig. 4.3. The ability of molecularly asymmetric A_1BA_2 triblock copolymers to modify phase stability (e.g., T_{ODT}) and generate bidisperse polymer brushes in tunable

fashion through synthetic means provides a single-molecule alternative to investigating the benefit of constrained chain mixing in confined nanoscale environments,³⁶ as well as an improved molecular-level understanding of the difference between microphase-ordered diblock and triblock copolymers.³⁷

Acknowledgments

This work was supported, in part, by the Research Council of Norway under the NANOMAT Program. We are indebted to Professor M. Olvera de la Cruz of Northwestern University for providing the computer algorithm used to generate the mean-field predictions reported herein, and we thank Dr. K.Ø. Rasmussen of Los Alamos National Laboratory for valuable advice.

References

1. Geoghegan, M.; Krausch, G. Wetting at polymer surfaces and interfaces. *Prog. Polym. Sci.* **28**, 261-302 (2003).
2. Avgeropoulos, A.; Dair, B.J.; Hadjichristidis, N.; Thomas, E.L. Tricontinuous double gyroid cubic phase in triblock copolymers of the ABA type. *Macromolecules* **30**, 5634-5642 (1997).
3. Hadjuk, D.A.; Harper, P.E.; Gruner, S.M.; Honeker, C.C.; Kim, G.; Thomas, E.L.; Fetters, L.J. . "The gyroid - A new equilibrium morphology in weakly segregated diblock copolymers" *Macromolecules* **27**, 4063-4075 (1994).
4. Laurer, J.H.; Hajduk, D.A.; Fung, J.C.; Sedat, J.W.; Smith, S.D.; Gruner, S.M.; Agard, D.A.; Spontak, R.J. Microstructural analysis of a cubic bicontinuous morphology in a neat SIS triblock copolymer. *Macromolecules* **30**, 3938-3941 (1997).
5. Schick, M. . Avatars of gyroid. *Physica A* **251**, 1-11 (1998).
6. Schulz, M.F.; Bates, F.S.; Almdal, K.; Mortensen, K. . Epitaxial relationship for hexagonal-to-cubic phase-transition in a block-copolymer mixture. *PRL* **73**, 83-86 (1994).
7. Burger, C.; Micha, M.A.; Oestreich, S.; Förster, S.; Antonietti, M. . Characterization of two new stable block copolymer mesophases by synchrotron small-angle scattering. *Europhys. Lett.* **42**, 425-429 (1998).
8. Disko, M.M.; Liang, K.S.; Behal, S.K.; Roe, R.J.; Jeon, K.J. . Catenoid-lamellar phase in blends of styrene-butadiene diblock copolymer and homopolymer. *Macromoles* **26**, 2983-2986 (1993).
9. Förster, S.; Khandpur, A.K.; Zhao, J.; Bates, F.S.; Hamley, I.W.; Ryan, A.J.; Bras, W. Complex phase-behavior of polyisoprene-polystyrene diblock copolymers near the order-disorder transition. *Macromolecules* **27**, 6922-6935 (1994).
10. Spontak, R.J.; Smith, S.D.; Ashraf, A. . Morphologies of diblock copolymer homopolymer blends near the order-disorder transition. *Polymer* **34**, 2233-2236 (1993).
11. Zhu, L.; Huang, P.; Cheng, S.Z.D.; Ge, Q.; Quirk, R.P.; Thomas, E.L.; Lotz, B.; Wittmann, J.-C.; Hsiao, B.S.; Yeh, F.J.; Liu, L.Z. Dislocation-controlled perforated layer phase in a PEO-b-PS diblock copolymer. *Phys. Rev. Lett.* **86**, 6030-6033 (2001).

12. Finnefrock, A.C.; Ulrich, R.; Toombes, G.E.S.; Gruner, S.M.; Wiesner, U. The plumber's nightmare: A new morphology in block copolymer-ceramic nanocomposites and mesoporous aluminosilicates. *J. Am. Chem. Soc.* **125**, 13084-13093 (2003).
13. Jain, A.; Toombes, G.E.S.; Hall, L.M.; Mahajan, S.; Garcia, C.B.W.; Probst, W.; Gruner, S.M.; Wiesner, U. Direct access to bicontinuous skeletal inorganic plumber's nightmare networks from block copolymers. *Ang. Chem. Int. Ed.* **44**, 1226-1229 (2005).
14. Hamley, I.W. Nanotechnology with Soft Materials. *Angewandte Chemie International Edition* **42**, 1692 (2003).
15. Park, C.; Yoon, J. and Thomas, E.L. . Enabling Nanotechnology with Self Assembled Block Copolymer Patterns. *Polymer* **44**, 6725 (2003).
16. Matsen, M.W.; Bates, F.S. Block copolymer microstructures in the intermediate-segregation regime. *J. Chem. Phys.* **106**, 2436 (1997).
17. Matsen, M.W. and Bates, F.S. Conformationally asymmetric block copolymers. *J. Polym. Sci. B: Polym. Phys.* **35**, 945 (1998).
18. Abetz, V. . in *Encyclopedia of Polymer Science and Technology*, 3rd ed. (ed. Kroschwitz, J.I. ed.) 482-523 (Wiley, Hoboken, NJ, 2003).
19. Bates, F.S.; Fredrickson, G.H. . Block copolymers-designer soft materials. *Phys. Today*, 32 (1999).
20. Stadler, R.; Auschra, C.; Beckmann, J.; Krappe, U.; Voigtmartin, i., Leibler, L. *Macromolecules* **28**, 3080 (1995).
21. Tyler, C.A.; Morse, D.C. . Orthorhombic Fddd network in triblock and diblock copolymer melts. *Physical Review Letters* **94**, 208302 (2005).
22. Laurer, J. H.; Hajduk, D. A.; Fung, J. C.; Sedat, J. W.; Smith, S. D.; Gruner, S. M.; Agard, D. A.; Spontak, R. J. Microstructural analysis of a cubic bicontinuous morphology in a neat SIS triblock copolymer. *Macromolecules* **30**, 3938-3941 (1997).
23. Matsen, M.W.; Thompson, R.B. Equilibrium behavior of symmetric ABA triblock copolymer melts. *J. Chem. Phys.* **111**, 7139 (1999).

24. Ryu, C.Y.; Lee, M.S.; Hajduk, D.A.; Lodge, T.P. Structure and viscoelasticity of matched asymmetric diblock and triblock copolymers in the cylinder and sphere microstructures. *J. Polym. Sci. B: Polym. Phys.* **35**, 2811-2823 (1998).
25. Kane, L.; Norman, D.A.; White, S.A.; Matsen, M.W.; Satkowski, M.M.; Smith, S.D.; Spontak, R.J. Molecular, Nanostructural and Mechanical Characteristics of Lamellar Triblock Copolymer Blends: Effects of Molecular Weight and Constraint. *Macromol. Rapid Commun.* **22**, 281 (2001).
26. Watanabe, H. ; Sato, T.; Osaki, K.; Yao, M.L.; Yamagishi, A. Rheological and dielectric behavior of a styrene-isoprene-styrene triblock copolymer in selective solvents .2. Contribution of loop-type middle blocks to elasticity and plasticity. *Macromolecules* **30** (1997).
27. Watanabe, H.; Sato, T.; Osaki, K. Concentration dependence of loop fraction in styrene-isoprene-styrene triblock copolymer solutions and corresponding changes in equilibrium elasticity. *Macromolecules* **33** (2000).
28. Banaszak, M.; Wołoszczuk, S.; Pakula, T.; Jurga, S. Computer simulation of structure and microphase separation in model A-B-A triblock copolymers. *Phys. Rev. E* **66**, 031804 (2002).
29. Matsen, M.W.; Schick, M. . Lamellar phase of a symmetric triblock copolymer. *Macromolecules* **27**, 187 (1994).
30. Mayes, A.M.; de la Cruz, M.O. Microphase Separation in Multiblock Copolymer Melts. *J. Chem. Phys.* **91**, 7228 (1989).
31. Mayes, A.M.; de la Cruz, M.O. Concentration Fluctuation Effects on Disorder-Order-Transitions in Block Copolymer Melts. *J. Chem. Phys.* **95**, 4670 (1991).
32. Dobrynin, A.V.; Erukhimovich, I.Y. Computer-aided comparative investigation of architecture influence on block copolymer phase-diagrams. *Macromolecules* **26**, 276-281 (1993).
33. Matsen, M.W. Equilibrium behavior of asymmetric ABA triblock copolymer melts. *J. Chem. Phys.* **113**, 5539 (2000).
34. Lodge, T.P.; Pan, C.; Jin, X.; Liu, Z.; Zhao, J.; Maurer, W.W.; Bates F.S. failure of the dilution approximation in block-copolymer solutions. *J. Polym. Sci. B: Polym. Phys.* **33**, 2289 (1995).

35. Milner, S.T.; Witten, T.A. Bending moduli of polymeric surfactant interfaces *J. Phys.* **49**, 1951 (1988).
36. Thompson, R.B.; Matsen, M.W. Improving polymeric microemulsions with block copolymer polydispersity. *PRL* **85**, 670 (2000).
37. Bailey, T.S.; Pham, H.D.; Bates, F.S. Morphological behavior bridging the symmetric AB and ABC states in the poly(styrene-b-isoprene-b-ethylene oxide) triblock copolymer system. *Macromolecules* **34**, 6994 (2001).

Appendix

Appendix A. Fortran algorithm of mean-field phase behavior

PROGRAM TRIBLOCKS

C PROGRAM TO CALCULATE THE PHASE DIAGRAM FOR A TRIBLOCK

C COPOLYMER OF ANY LENGTH BLOCKS, A1-B-A2

DOUBLE PRECISION F1,F2,FB,N,DF1,DF2,DFB,

1

FF1,FF2,FFB,SF,INV,TST,GAA,GBB,GAB,F,X,LAM4,HEX3,HEX4,BCC3,BCC4,SPIN

DOUBLE PRECISION RGAAA,RGBBA,RGBAB,RGABB,RGAAB,

1 RGABA,RGBAA,RG111,RG222,RGBBB,RG121,

2 RG212,RG11B,RG22B,RG12B,

3 RBBB2,RBBB1,THIRD,LAMA,LAMB

DOUBLE PRECISION

H1,H2,H3,H(3),GAAA(3),GBBA(3),GBAB(3),GABB(3),GAAB(3),

1 GABA(3),GBAA(3),G111(3),G222(3),GBBB(3),G121(3),G112(3),

2 G212(3),G221(3),G11B(3),G1B1(3),G22B(3),G2B2(3),G1B2(3),

3 G2B1(3),GBB2(3),GB2B(3),GBB1(3),GB1B(3),Y(3),GAM1,GAM2,

4 GAM4,GAM5,GAM6,GAM7,GAM8,GAM9,GAM10,GAM11,GAM12,GAM13,

5 GAM15,GAM16,GAM(16),S11(3),S22(3),S12(3),HDF1,HDF2,HDFB,

6 HFF1,HFF2,HFFB,GAM3,GAM14,H1VAL(4),H2VAL(4),TRANS1,

7 FOURTH(4),TRANS2

DOUBLE PRECISION G1111(3),G2222(3),GBBBB(3),G1112(3),
1 G2221(3),G222B(3),GBBB2(3),GBBB1(3),G1122(3),G11BB(3),
2 G22BB(3),G11B2(3),GBB12(3),GAMMA4(16),GIJKL(16),
3 LAM(16),GAAAA,RBBBBB,GBBBA,GBBAA,GBAAB,GBABA,GAAAB,
4 GB12B(3),G22B1(3),G1212(3),G1B1B(3),G2B2B(3),
5 G1B12(3),G2B21(3),G1221(3),G1BB1(3),G2BB2(3),G2B12(3),
6 G1B21(3),G111B(3),TAU

DOUBLE PRECISION N1, N2, NB

COMMON LAM4,HEX3,HEX4,BCC3,BCC4,SPIN,TRANS1,F

INTEGER I,J,K,A,B,P

Print *, 'Enter Block Masses of A1, B and A2'

Read *, M1,M2,M3

Print *, 'Enter Repeat Unit Masses of Species A and B'

Read *, MA,MB

! In our calculations, we used molecular weight of 104 for A type of polymer and 68 for B
type polymer

! MA=104

! MB=68

C Determine molecular characteristics from block sizes (calculates how many units there are in each block)

$$N1 = \text{DFLOAT}(M1)/\text{DFLOAT}(MA)$$

$$N2 = \text{DFLOAT}(M3)/\text{DFLOAT}(MA)$$

$$NB = \text{DFLOAT}(M2)/\text{DFLOAT}(MB)$$

$$N = N1+N2+NB$$

$$F1 = N1/N$$

$$F2 = N2/N$$

$$F = F1+F2$$

$$FB = NB/N$$

$$\text{TAU} = F1/F$$

```
WRITE(4,*) 'N1',N1,'N2',N2,'NB',NB,'N',N,'F1',F1,'F2',F2,'F',F
```

```
WRITE(4,*) 'FB',FB,'TAU',TAU
```

```
! WRITE(7,*) 'DIS/HEX AND BCC/LAM'
```

```
WRITE(2,*) 'BCC/HEX,HEX/LAM,F'
```

```
WRITE(3,*) 'DIS/BCC,SPINODAL,X'
```

```
WRITE(4,*) 'X* AND f'
```

```
! WRITE(11,*)'TAU,fc,(XN)c'
```

```
! You can find the results in Fort.2, Fort.3 and Fort.4 files. Fort.7 and Fort.11 are useless
```

```
TST = 0.0
```

X = 3.

300 DF2 = 2.*(F2*X + EXP(-F2*X)-1.)/X**2

DF1 = 2.*(F1*X + EXP(-F1*X)-1.)/X**2

DFB = 2.*(FB*X + EXP(-FB*X)-1.)/X**2

FF2 = (1.-EXP(-F2*X))/X

FF1 = (1.-EXP(-F1*X))/X

FFB = (1.-EXP(-FB*X))/X

GAA = N*(DF1+DF2+2.*FF1*FF2*EXP(-FB*X))

GBB = N*DFB

GAB = N*FFB*(FF1+FF2)

INV = (GAA+GBB+2.*GAB)/(GAA*GBB-GAB**2)

SF = 1./INV

IF(SF.LT.TST)THEN

SF=TST

SPIN = N/(2.*TST)

SPIN = N/(2.*SF)

X = X - 0.001

GO TO 100

```

ELSE
TST = SF
    X = X + 0.001
GOTO 300
ENDIF
    WRITE(2,*) 'f,F,(XN)s',SPIN,'x*',X
100 CONTINUE

DF2 = 2.*(F2*X + EXP(-F2*X)-1.)
DF1 = 2.*(F1*X + EXP(-F1*X)-1.)
DFB = 2.*(FB*X + EXP(-FB*X)-1.)

FF2 = 1.-EXP(-F2*X)
FF1 = 1.-EXP(-F1*X)
FFB = 1.-EXP(-FB*X)

GAA = DF1+DF2+2.*FF1*FF2*EXP(-FB*X)
GAB = FFB*(FF1+FF2)
GAB = FFB*(FF1+FF2)

C CALCULATE THE FREE ENERGY
C THIRD ORDER TERM

```

C CALCULATE GAMMA 3 USING H = 1

C ALL TERMS HAVE BEEN MULTIPLIED BY (X/N)^3

$$RG111 = F1*X + 2.*EXP(-F1*X) -2. + F1*X*EXP(-F1*X)$$

$$RG222 = F2*X + 2.*EXP(-F2*X) -2. + F2*X*EXP(-F2*X)$$

$$RG121 = EXP(-FB*X)*FF2*(1.-EXP(-F1*X)-F1*X*EXP(-F1*X))$$

$$RG212 = EXP(-FB*X)*FF1*(1.-EXP(-F2*X)-F2*X*EXP(-F2*X))$$

$$RBBB2 = FF2*(1.-FB*X*EXP(-FB*X)-EXP(-FB*X))$$

$$RBBBB = FB*X + 2.*EXP(-FB*X) -2. + FB*X*EXP(-FB*X)$$

$$RG11B = FFB*(1.-F1*X*EXP(-F1*X)-EXP(-F1*X))$$

$$RG22B = FFB*(1.-F2*X*EXP(-F2*X)-EXP(-F2*X))$$

$$RBBB1 = FF1*(1.-FB*X*EXP(-FB*X)-EXP(-FB*X))$$

$$RG12B = FB*X*EXP(-FB*X)*FF1*FF2$$

C EQUIVALENTS FOR H = 1

$$C \ G112 = G211 = G121$$

$$C \ G221 = G122 = G212$$

$$C \ G1B1 = G11B = GB11$$

$$C \ G2B2 = G22B = GB22$$

$$C \ G2B1 = G12B = G1B2 = G2B1 = G21B = GB12$$

$$C \ GB2B = GBB2 = G2BB$$

$$C \ G1BB = GBB1 = GB1B$$

C EQUIVALENTS FOR ANY H VALUE

C GB11 = G1B1

C G211 = G121

C G122 = G212

C GB22 = G2B2

C GB12 = G1B2

C GB21 = G2B1

C G2BB = GB2B

C G1BB = GB1B

C CALCULATE THE GAMMA 3 TERM

C NOTE THAT 'THIRD' IS ALREADY MULT BY N

$$RGAAA = 6. * (RG111 + RG222 + RG121 + RG212)$$

$$RGBBA = 2. * (RBBB1 + RBBB2)$$

$$RGBAB = RGBBA$$

$$RGABB = RGBBA$$

$$RGAAB = 2. * (RG11B + RG22B) + 2. * RG12B$$

$$RGABA = RGAAB$$

$$RGBAA = RGAAB$$

$$LAMA = (GBB + GAB) / (GBB * GAA - GAB ** 2)$$

$$LAMB = -(GAA + GAB) / (GBB * GAA - GAB ** 2)$$

$$THIRD = -X ** 3 * (RGAAA * LAMA ** 3 + 3. * RGAAB * LAMA ** 2 * LAMB +$$

1 6.*RGBBB*LAMB**3 + 3.*RGBAB*LAMA*LAMB**2)

C WRITE(5,*) THIRD

C WRITE(5,*)'ENTER H1,H2'

C READ *, H1,H2

H1VAL(1) = 0.

H1VAL(2) = 0.

H1VAL(3) = 0.

H1VAL(4) = 1.

H2VAL(1) = 0.

H2VAL(2) = 1.

H2VAL(3) = 2.

H2VAL(4) = 2.

FOURTH(1) = 0.

FOURTH(2) = 0.

FOURTH(3) = 0.

FOURTH(4) = 0.

DO 2500 A=1,4

$$H1 = H1VAL(A)$$

$$H2 = H2VAL(A)$$

$$H3 = 4.-H1-H2$$

$$GAM(1) = 0.$$

$$GAM(2) = 0.$$

$$GAM(3) = 0.$$

$$GAM(4) = 0.$$

$$GAM(5) = 0.$$

$$GAM(6) = 0.$$

$$GAM(7) = 0.$$

$$GAM(8) = 0.$$

$$GAM(9) = 0.$$

$$GAM(10) = 0.$$

$$GAM(11) = 0.$$

$$GAM(12) = 0.$$

$$GAM(13) = 0.$$

$$GAM(14) = 0.$$

$$GAM(15) = 0.$$

$$GAM(16) = 0.$$

$$H(1) = H1$$

$$H(2) = H2$$

$$H(3) = H3$$

DO 700 J=1,3

IF(H(J).EQ.1.0.OR.H(J).EQ.3.0)THEN

$$GAAA(J) = RGAAA$$

$$GBBA(J) = RGBBA$$

$$GBAB(J) = RGBAB$$

$$GABB(J) = RGABB$$

$$GAAB(J) = RGAAB$$

$$GABA(J) = RGABA$$

$$GBAA(J) = RGBAA$$

$$GBBB(J) = 6.*RGBBB$$

ELSE IF(H(J).EQ.0.0.OR.H(J).EQ.4.0)THEN

C THIRD ORDER H = 0 TERMS

$$G111(J) = (F1*X)**2/2. + 1. - EXP(-F1*X) - F1*X$$

$$G222(J) = (F2*X)**2/2. + 1. - EXP(-F2*X) - F2*X$$

$$G121(J) = EXP(-FB*X)*FF2*DF1/2.$$

$$G112(J) = F2*X*DF1/2.$$

$$G212(J) = EXP(-FB*X)*FF1*DF2/2.$$

$$G221(J) = F1*X*DF2/2.$$

$$G_{BBB}(J) = (FB \cdot X)^{2/2} + 1 - \exp(-FB \cdot X) - FB \cdot X$$

$$G_{11B}(J) = FB \cdot X \cdot DF1/2.$$

$$G_{1B1}(J) = FF1 \cdot DF1/2.$$

$$G_{22B}(J) = FB \cdot X \cdot DF2/2.$$

$$G_{2B2}(J) = FF2 \cdot DF2/2.$$

$$G_{1B2}(J) = F2 \cdot X \cdot FF1 \cdot FF2$$

$$G_{2B1}(J) = F1 \cdot X \cdot FF2 \cdot FF1$$

$$G_{BB2}(J) = F2 \cdot X \cdot DFB/2.$$

$$G_{B2B}(J) = FF2 \cdot DFB/2.$$

$$G_{BB1}(J) = F1 \cdot X \cdot DFB/2.$$

$$G_{B1B}(J) = FF1 \cdot DFB/2.$$

C THIRD ORDER TERMS FOR H NOT EQUAL TO 1

$$900 \quad G_{AAA}(J) = 4 \cdot (G_{111}(J) + G_{222}(J)) + 2 \cdot (RG_{111} + RG_{222} +$$

$$1 \quad G_{112}(J) + G_{221}(J) + G_{121}(J) + G_{212}(J) +$$

$$2 \quad RG_{121} + RG_{212})$$

$$G_{AAB}(J) = 2 \cdot (G_{11B}(J) + G_{22B}(J)) + 2 \cdot RG_{12B}$$

$$G_{ABA}(J) = G_{1B1}(J) + G_{2B2}(J) + G_{1B2}(J) + G_{2B1}(J) + RG_{11B}$$

$$1 \quad + RG_{22B}$$

$$GBAA(J) = GABA(J)$$

$$GBBA(J) = 2.*(GBB1(J) + GBB2(J))$$

$$GBAB(J) = GB1B(J) + GB2B(J) + RGBB1 + RGBB2$$

$$GABB(J) = GBAB(J)$$

$$GBBB(J) = 4.*GBBB(J) + 2.*RGBBB$$

GO TO 1000

ELSE

C THIRD ORDER TERMS WITH H(J)

$$G111(J) = (F1*X - 1. - 1./H(J) + H(J)*EXP(-F1*X)/(H(J)-1.) -$$

$$1 \quad \text{EXP}(-H(J)*F1*X)/(H(J)**2 - H(J)))/H(J)$$

$$G222(J) = (F2*X - 1. - 1./H(J) + H(J)*EXP(-F2*X)/(H(J)-1.) -$$

$$1 \quad \text{EXP}(-H(J)*F2*X)/(H(J)**2 - H(J)))/H(J)$$

$$G121(J) = \text{EXP}(-FB*X)*FF2*(1. + H(J)*EXP(-F1*X)/(1.-H(J)) +$$

$$1 \quad \text{EXP}(-H(J)*F1*X)/(H(J)-1.))/H(J)$$

$$G112(J) = \text{EXP}(-FB*H(J)*X)*(1.-\text{EXP}(-F2*H(J)*X))*$$

$$1 \quad (1.-H(J)*\text{EXP}(-F1*X)/(H(J)-1.)$$

$$2 \quad + \text{EXP}(-H(J)*F1*X)/(H(J)-1.))/H(J)**2$$

$$G212(J) = \text{EXP}(-\text{FB} * \text{X}) * \text{FF1} * (1. + \text{H}(J) * \text{EXP}(-\text{F2} * \text{X}) / (1. - \text{H}(J)) +$$

$$1 \quad \text{EXP}(-\text{H}(J) * \text{F2} * \text{X}) / (\text{H}(J) - 1.)) / \text{H}(J)$$

$$G221(J) = \text{EXP}(-\text{FB} * \text{H}(J) * \text{X}) * (1. - \text{EXP}(-\text{F1} * \text{H}(J) * \text{X})) *$$

$$1 \quad (1. - \text{H}(J) * \text{EXP}(-\text{F2} * \text{X}) / (\text{H}(J) - 1.))$$

$$2 \quad + \text{EXP}(-\text{H}(J) * \text{F2} * \text{X}) / (\text{H}(J) - 1.) / \text{H}(J) ** 2$$

$$G222(J) = (\text{FB} * \text{X} - 1. - 1. / \text{H}(J) + \text{H}(J) * \text{EXP}(-\text{FB} * \text{X}) / (\text{H}(J) - 1.)) -$$

$$1 \quad \text{EXP}(-\text{H}(J) * \text{FB} * \text{X}) / (\text{H}(J) ** 2 - \text{H}(J))) / \text{H}(J)$$

$$G11B(J) = (1. - \text{EXP}(-\text{H}(J) * \text{FB} * \text{X})) * (1. - \text{H}(J) * \text{EXP}(-\text{F1} * \text{X}) /$$

$$1 \quad (\text{H}(J) - 1.) + \text{EXP}(-\text{H}(J) * \text{F1} * \text{X}) / (\text{H}(J) - 1.)) / \text{H}(J) ** 2$$

$$G1B1(J) = \text{FFB} * (1. + \text{H}(J) * \text{EXP}(-\text{F1} * \text{X}) / (1. - \text{H}(J)) +$$

$$1 \quad \text{EXP}(-\text{H}(J) * \text{F1} * \text{X}) / (\text{H}(J) - 1.)) / \text{H}(J)$$

$$G22B(J) = (1. - \text{EXP}(-\text{H}(J) * \text{FB} * \text{X})) * (1. - \text{H}(J) * \text{EXP}(-\text{F2} * \text{X}) / (\text{H}(J) - 1.))$$

$$1 \quad + \text{EXP}(-\text{H}(J) * \text{F2} * \text{X}) / (\text{H}(J) - 1.) / \text{H}(J) ** 2$$

$$G2B2(J) = \text{FFB} * (1. + \text{H}(J) * \text{EXP}(-\text{F2} * \text{X}) / (1. - \text{H}(J)) +$$

$$1 \quad \text{EXP}(-\text{H}(J) * \text{F2} * \text{X}) / (\text{H}(J) - 1.)) / \text{H}(J)$$

$$G1B2(J) = \text{FF1} * (1. - \text{EXP}(-\text{H}(J) * \text{F2} * \text{X})) * (\text{EXP}(-\text{H}(J) * \text{FB} * \text{X}) -$$

1 EXP(-FB*X)/(H(J)-H(J)**2)

G2B1(J) = FF2*(1.-EXP(-H(J)*F1*X))*(EXP(-H(J)*FB*X) -

1 EXP(-FB*X)/(H(J)-H(J)**2)

GBB2(J) = (1.-EXP(-H(J)*F2*X))*(1.-H(J)*EXP(-FB*X)/(H(J)-1.)

1 + EXP(-H(J)*FB*X)/(H(J)-1.))/H(J)**2

GB2B(J) = FF2*(1.+H(J)*EXP(-FB*X)/(1.-H(J))

1 + EXP(-H(J)*FB*X)/(H(J)-1.))/H(J)

GBB1(J) = (1.-EXP(-H(J)*F1*X))*(1.-H(J)*EXP(-FB*X)/(H(J)-1.)

1 + EXP(-H(J)*FB*X)/(H(J)-1.))/H(J)**2

GB1B(J) = FF1*(1.+H(J)*EXP(-FB*X)/(1.-H(J))

1 + EXP(-H(J)*FB*X)/(H(J)-1.))/H(J)

GO TO 900

ENDIF

C Gijm * Gkln matrix terms

$$1000 \quad Y(1) = H1 * X$$

$$Y(2) = H2 * X$$

$$Y(3) = H3 * X$$

IF(H(J).EQ.0.0.OR.H(J).EQ.4.0)THEN

$$S11(J) = 1./X**2$$

$$S22(J) = 1./X**2$$

$$S12(J) = 1./X**2$$

ELSE IF(H(J).EQ.3.0)THEN

$$Y(J) = X$$

$$H(J) = 1.$$

$$1300 \quad HDF2 = 2.*(F2*Y(J) + EXP(-F2*Y(J)) - 1.)/H(J)**2$$

$$HDF1 = 2.*(F1*Y(J) + EXP(-F1*Y(J)) - 1.)/H(J)**2$$

$$HDFB = 2.*(FB*Y(J) + EXP(-FB*Y(J)) - 1.)/H(J)**2$$

$$HFF2 = (1.-EXP(-F2*Y(J)))/H(J)$$

$$HFF1 = (1.-EXP(-F1*Y(J)))/H(J)$$

$$HFFB = (1.-EXP(-FB*Y(J)))/H(J)$$

$$GAA = HDF1 + HDF2 + 2.*HFF1*HFF2*EXP(-FB*Y(J))$$

$$GBB = HDFB$$

$$GAB = HFFB*(HFF1 + HFF2)$$

C ELEMENTS OF INVERSE MATRIX FOR 4TH ORDER TERMS

$$S11(J) = GBB/(GAA*GBB - GAB**2)$$

$$S12(J) = -GAB/(GAA*GBB - GAB**2)$$

$$S22(J) = GAA/(GAA*GBB - GAB**2)$$

ELSE

GOTO 1300

ENDIF

$$GAM1 = GAAA(J)**2*S11(J) + 2.*GAAA(J)*GAAB(J)*S12(J) + \\ 1 \quad GAAB(J)**2*S22(J)$$

$$GAM2 = GAAA(J)*GABA(J)*S11(J) + (GAAA(J)*GABB(J) + \\ 1 \quad GAAB(J)*GABA(J))*S12(J) + GAAB(J)*GABB(J)*S22(J)$$

$$GAM3 = GAAA(J)*GBAA(J)*S11(J) + (GAAA(J)*GBAB(J) + \\ 1 \quad GAAB(J)*GBAA(J))*S12(J) + GAAB(J)*GBAB(J)*S22(J)$$

$$GAM4 = GAAA(J)*GBBA(J)*S11(J) + (GAAA(J)*G BBB(J) + \\ 1 \quad GAAB(J)*GBBA(J))*S12(J) + GAAB(J)*G BBB(J)*S22(J)$$

$$GAM5 = GABA(J)*GAAA(J)*S11(J) + (GABA(J)*GAAB(J) + \\ 1 \quad GABB(J)*GAAA(J))*S12(J) + GABB(J)*GAAB(J)*S22(J)$$

$$\text{GAM6} = \text{GABA(J)**2*S11(J)} + 2.*\text{GABA(J)*GABB(J)*S12(J)} +$$

$$1 \quad \text{GABB(J)**2*S22(J)}$$

$$\text{GAM7} = \text{GABA(J)*GBAA(J)*S11(J)} + (\text{GABA(J)*GBAB(J)} +$$

$$1 \quad \text{GABB(J)*GBAA(J))*S12(J)} + \text{GABB(J)*GBAB(J)*S22(J)}$$

$$\text{GAM8} = \text{GABA(J)*GBBA(J)*S11(J)} + (\text{GABA(J)*GBBB(J)} +$$

$$1 \quad \text{GABB(J)*GBBA(J))*S12(J)} + \text{GABB(J)*GBBB(J)*S22(J)}$$

$$\text{GAM9} = \text{GBAA(J)*GAAA(J)*S11(J)} + (\text{GBAA(J)*GAAB(J)} +$$

$$1 \quad \text{GBAB(J)*GAAA(J))*S12(J)} + \text{GBAB(J)*GAAB(J)*S22(J)}$$

$$\text{GAM10} = \text{GBAA(J)*GABA(J)*S11(J)} + (\text{GBAA(J)*GABB(J)} +$$

$$1 \quad \text{GBAB(J)*GABA(J))*S12(J)} + \text{GBAB(J)*GABB(J)*S22(J)}$$

$$\text{GAM11} = \text{GBAA(J)**2*S11(J)} + 2.*\text{GBAA(J)*GBAB(J)*S12(J)} +$$

$$1 \quad \text{GBAB(J)**2*S22(J)}$$

$$\text{GAM12} = \text{GBAA(J)*GBBA(J)*S11(J)} + (\text{GBAA(J)*GBBB(J)} +$$

$$1 \quad \text{GBAB(J)*GBBA(J))*S12(J)} + \text{GBAB(J)*GBBB(J)*S22(J)}$$

$$\text{GAM13} = \text{GBBA(J)*GAAA(J)*S11(J)} + (\text{GBBA(J)*GAAB(J)} +$$

$$1 \quad \text{GBBB(J)*GAAA(J))*S12(J)} + \text{GBBB(J)*GAAB(J)*S22(J)}$$

$$\text{GAM14} = \text{GBBA(J)*GABA(J)*S11(J)} + (\text{GBBA(J)*GABB(J)} +$$

$$1 \quad \text{GBBB(J)*GABA(J))*S12(J)} + \text{GBBB(J)*GABB(J)*S22(J)}$$

$$\text{GAM15} = \text{GBBA(J)*GBAA(J)*S11(J)} + (\text{GBBA(J)*GBAB(J)} +$$

$$1 \quad \text{GBBB(J)*GBAA(J))*S12(J)} + \text{GBBB(J)*GBAB(J)*S22(J)}$$

$$\text{GAM16} = \text{GBBA(J)**2*S11(J)} + 2.*\text{GBBA(J)*GBBB(J)*S12(J)} +$$

1 GBBB(J)**2*S22(J)

$$\text{GAM}(1) = \text{GAM}(1) + \text{GAM1}$$

$$\text{GAM}(2) = \text{GAM}(2) + \text{GAM2}$$

$$\text{GAM}(3) = \text{GAM}(3) + \text{GAM3}$$

$$\text{GAM}(4) = \text{GAM}(4) + \text{GAM4}$$

$$\text{GAM}(5) = \text{GAM}(5) + \text{GAM5}$$

$$\text{GAM}(6) = \text{GAM}(6) + \text{GAM6}$$

$$\text{GAM}(7) = \text{GAM}(7) + \text{GAM7}$$

$$\text{GAM}(8) = \text{GAM}(8) + \text{GAM8}$$

$$\text{GAM}(9) = \text{GAM}(9) + \text{GAM9}$$

$$\text{GAM}(10) = \text{GAM}(10) + \text{GAM10}$$

$$\text{GAM}(11) = \text{GAM}(11) + \text{GAM11}$$

$$\text{GAM}(12) = \text{GAM}(12) + \text{GAM12}$$

$$\text{GAM}(13) = \text{GAM}(13) + \text{GAM13}$$

$$\text{GAM}(14) = \text{GAM}(14) + \text{GAM14}$$

$$\text{GAM}(15) = \text{GAM}(15) + \text{GAM15}$$

$$\text{GAM}(16) = \text{GAM}(16) + \text{GAM16}$$

700 CONTINUE

C FOURTH ORDER H1 TERMS

IF(H1.EQ.0.0.OR.H1.EQ.4.0)THEN

C H = 0 CONTRIBUTIONS

$$G1111(1) = 8. * ((F1 * X) ** 2 / 2. - 2. * F1 * X - F1 * X * EXP(-F1 * X)) \\ 1 \quad + 3. * (1. - EXP(-F1 * X))$$

$$G2222(1) = 8. * ((F2 * X) ** 2 / 2. - 2. * F2 * X - F2 * X * EXP(-F2 * X)) \\ 1 \quad + 3. * (1. - EXP(-F2 * X))$$

$$GBBBB(1) = 8. * ((FB * X) ** 2 / 2. - 2. * FB * X - FB * X * EXP(-FB * X)) \\ 1 \quad + 3. * (1. - EXP(-FB * X))$$

$$G1112(1) = 2. * EXP(-FB * X) * FF2 * (2. * (EXP(-F1 * X) - 1.) + \\ 1 \quad F1 * X * (1. + EXP(-F1 * X)))$$

$$G111B(1) = 2. * FFB * (2. * (EXP(-F1 * X) - 1.) + \\ 1 \quad F1 * X * (1. + EXP(-F1 * X)))$$

$$G2221(1) = 2. * EXP(-FB * X) * FF1 * (2. * (EXP(-F2 * X) - 1.) + \\ 1 \quad F2 * X * (1. + EXP(-F2 * X)))$$

$$G222B(1) = 2. * FFB * (2. * (EXP(-F2 * X) - 1.) + \\ 1 \quad F2 * X * (1. + EXP(-F2 * X)))$$

$$GBBB2(1) = 2. * FF2 * (2. * (EXP(-FB * X) - 1.) + \\ 1 \quad FB * X * (1. + EXP(-FB * X)))$$

$$GBBB1(1) = 2. * FF1 * (2. * (EXP(-FB * X) - 1.) +$$

$$1 \quad \text{FB*X*(1. + EXP(-FB*X))}$$

$$\text{G1122(1) = DF1*DF2}$$

$$\text{G11BB(1) = DF1*DFB}$$

$$\text{G22BB(1) = DF2*DFB}$$

$$\text{G11B2(1) = FFB*FF2*DF1}$$

$$\text{G22B1(1) = FFB*FF1*DF2}$$

$$\text{GB12B(1) = FF2*FF1*(1. - EXP(-FB*X) -}$$

$$1 \quad \text{FB*X*EXP(-FB*X))}$$

ELSE IF(H1.EQ.1.0.OR.H1.EQ.3.0)THEN

C H = 1 CONTRIBUTIONS

$$\text{G1111(1) = 8.*(F1*X + 2.*F1*X*EXP(-F1*X) + (F1*X)**2*}$$

$$1 \quad \text{EXP(-F1*X)/2. + 3.*(EXP(-F1*X) - 1.)}$$

$$\text{G2222(1) = 8.*(F2*X + 2.*F2*X*EXP(-F2*X) + (F2*X)**2*}$$

$$1 \quad \text{EXP(-F2*X)/2. + 3.*(EXP(-F2*X) - 1.)}$$

$$\text{GBBBBB(1) = 8.*(FB*X + 2.*FB*X*EXP(-FB*X) +}$$

$$1 \quad \text{(FB*X)**2*EXP(-FB*X)/2. + 3.*(EXP(-FB*X) - 1.)}$$

$$\text{G1122(1) = 4.*EXP(-FB*X)*(1. - EXP(-F1*X) - F1*X*}$$

$$1 \quad \text{EXP(-F1*X))*(1. - EXP(-F2*X) - F2*X*EXP(-F2*X))}$$

$$G11BB(1) = 4. * (1. - \text{EXP}(-F1 * X) - F1 * X * \text{EXP}(-F1 * X))$$

$$1 \quad * (1. - \text{EXP}(-FB * X) - FB * X * \text{EXP}(-FB * X))$$

$$G22BB(1) = 4. * (1. - \text{EXP}(-FB * X) - FB * X * \text{EXP}(-FB * X))$$

$$1 \quad * (1. - \text{EXP}(-F2 * X) - F2 * X * \text{EXP}(-F2 * X))$$

$$G1112(1) = 2. * \text{EXP}(-FB * X) * FF2 * (1. - \text{EXP}(-F1 * X) -$$

$$1 \quad F1 * X * \text{EXP}(-F1 * X) - (F1 * X) ** 2 * \text{EXP}(-F1 * X) / 2.)$$

$$G111B(1) = 2. * FF2 * (1. - \text{EXP}(-F1 * X) -$$

$$1 \quad F1 * X * \text{EXP}(-F1 * X) - (F1 * X) ** 2 * \text{EXP}(-F1 * X) / 2.)$$

$$G222B(1) = 2. * FF2 * (1. - \text{EXP}(-F2 * X) -$$

$$1 \quad F2 * X * \text{EXP}(-F2 * X) - (F2 * X) ** 2 * \text{EXP}(-F2 * X) / 2.)$$

$$G2221(1) = 2. * \text{EXP}(-FB * X) * FF1 * (1. - \text{EXP}(-F2 * X) -$$

$$1 \quad F2 * X * \text{EXP}(-F2 * X) - (F2 * X) ** 2 * \text{EXP}(-F2 * X) / 2.)$$

$$GBBB2(1) = 2. * FF2 * (1. - \text{EXP}(-FB * X) -$$

$$1 \quad FB * X * \text{EXP}(-FB * X) - (FB * X) ** 2 * \text{EXP}(-FB * X) / 2.)$$

$$GBBB1(1) = 2. * FF1 * (1. - \text{EXP}(-FB * X) -$$

$$1 \quad FB * X * \text{EXP}(-FB * X) - (FB * X) ** 2 * \text{EXP}(-FB * X) / 2.)$$

$$GB12B(1) = FF2 * FF1 * (FB * X) ** 2 * \text{EXP}(-FB * X) / 2.$$

$$G11B2(1) = 2. * FB * X * FF2 * \text{EXP}(-FB * X) * (1. - \text{EXP}(-F1 * X)$$

$$1 \quad - F1 * X * \text{EXP}(-F1 * X))$$

$$G22B1(1) = 2. * FB * X * FF1 * \text{EXP}(-FB * X) * (1. - \text{EXP}(-F2 * X)$$

$$1 \quad - F2 * X * \text{EXP}(-F2 * X))$$

ELSE

$$\begin{aligned} G1111(1) &= 8. * (F1 * X / H1 + (2. * H1 - 3.) * \text{EXP}(-F1 * X) / (1. - H1))^{**2} - \\ 1 & \quad (2. * H1 + 1.) / H1^{**2} + \text{EXP}(-H1 * F1 * X) / (H1 * (1. - H1))^{**2} \\ 2 & \quad - F1 * X * \text{EXP}(-F1 * X) / (1. - H1) \end{aligned}$$

$$\begin{aligned} G2222(1) &= 8. * (F2 * X / H1 + (2. * H1 - 3.) * \text{EXP}(-F2 * X) / (1. - H1))^{**2} - \\ 1 & \quad (2. * H1 + 1.) / H1^{**2} + \text{EXP}(-H1 * F2 * X) / (H1 * (1. - H1))^{**2} \\ 2 & \quad - F2 * X * \text{EXP}(-F2 * X) / (1. - H1) \end{aligned}$$

$$\begin{aligned} GBBBB(1) &= 8. * (FB * X / H1 + (2. * H1 - 3.) * \text{EXP}(-FB * X) / (1. - H1))^{**2} - \\ 1 & \quad (2. * H1 + 1.) / H1^{**2} + \text{EXP}(-H1 * FB * X) / (H1 * (1. - H1))^{**2} \\ 2 & \quad - FB * X * \text{EXP}(-FB * X) / (1. - H1) \end{aligned}$$

$$\begin{aligned} G1122(1) &= 4. * (1. / H1 + \text{EXP}(-H1 * F1 * X) / (H1 * (H1 - 1.))) + \\ 1 & \quad \text{EXP}(-F1 * X) / (1. - H1)) * (1. / H1 + \text{EXP}(-H1 * F2 * X) / \\ 2 & \quad (H1 * (H1 - 1.)) + \text{EXP}(-F2 * X) / (1. - H1)) * \text{EXP}(-H1 * FB * X) \end{aligned}$$

$$\begin{aligned} G1112(1) &= 2. * FF2 * \text{EXP}(-FB * X) * (1. / H1 + (2. - H1) \\ 1 & \quad * \text{EXP}(-F1 * X) / (H1 - 1.)^{**2} + F1 * X * \text{EXP}(-F1 * X) / \\ 2 & \quad (1. - H1) - \text{EXP}(-H1 * F1 * X) / (H1 * (H1 - 1.)^{**2})) \end{aligned}$$

$$\begin{aligned} G2221(1) &= 2. * FF1 * \text{EXP}(-FB * X) * (1. / H1 + (2. - H1) \\ 1 & \quad * \text{EXP}(-F2 * X) / (H1 - 1.)^{**2} + F2 * X * \text{EXP}(-F2 * X) / \\ 2 & \quad (1. - H1) - \text{EXP}(-H1 * F2 * X) / (H1 * (H1 - 1.)^{**2})) \end{aligned}$$

$$\begin{aligned} G11BB(1) &= 4. * (1. / H1 + \text{EXP}(-H1 * F1 * X) / (H1 * (H1 - 1.))) + \\ 1 & \quad \text{EXP}(-F1 * X) / (1. - H1)) * (1. / H1 + \text{EXP}(-H1 * FB * X) / \end{aligned}$$

$$\begin{aligned}
& 2 \quad (H1*(H1-1.)) + EXP(-FB*X)/(1.-H1)) \\
G22BB(1) = & 4.*(1./H1 + EXP(-H1*F2*X)/(H1*(H1-1.)) + \\
& 1 \quad EXP(-F2*X)/(1.-H1))*(1/H1 + EXP(-H1*FB*X)/ \\
& 2 \quad (H1*(H1-1.)) + EXP(-FB*X)/(1.-H1)) \\
G BBB1(1) = & 2.*FF1*(1./H1 +(2.-H1)*EXP(-FB*X)/(H1-1.)**2 + \\
& 1 \quad FB*X*EXP(-FB*X)/(1.-H1) - \\
& 2 \quad EXP(-H1*FB*X)/(H1*(H1-1.)**2)) \\
GB12B(1) = & FF2*FF1*(EXP(-H1*FB*X)-EXP(-FB*X) \\
& 1 \quad + (H1-1.)*FB*X*EXP(-FB*X)/(H1-1.)**2 \\
G111B(1) = & 2.*FFB*(1./H1 +(2.-H1)*EXP(-F1*X)/(H1-1.)**2 + \\
& 1 \quad F1*X*EXP(-F1*X)/(1.-H1) - \\
& 2 \quad EXP(-H1*F1*X)/(H1*(H1-1.)**2)) \\
G222B(1) = & 2.*FFB*(1./H1 +(2.-H1)*EXP(-F2*X)/(H1-1.)**2 + \\
& 1 \quad F2*X*EXP(-F2*X)/(1.-H1) - \\
& 2 \quad EXP(-H1*F2*X)/(H1*(H1-1.)**2)) \\
G11B2(1) = & 2.*FF2*(EXP(-H1*FB*X) - EXP(-FB*X))* \\
& 1 \quad (1./H1 - EXP(-H1*F1*X)/(H1*(1.-H1)) + EXP(-F1*X)/ \\
& 2 \quad (1.-H1)) \\
G22B1(1) = & 2.*FF1*(EXP(-H1*FB*X) - EXP(-FB*X))* \\
& 1 \quad (1./H1 - EXP(-H1*F2*X)/(H1*(1.-H1)) + EXP(-F2*X)/ \\
& 2 \quad (1.-H1)) \\
G BBB2(1) = & 2.*FF2*(1./H1 +(2.-H1)*EXP(-FB*X)/(H1-1.)**2 +
\end{aligned}$$

$$1 \quad \text{FB} \cdot \text{X} \cdot \text{EXP}(-\text{FB} \cdot \text{X}) / (1 - \text{H1}) -$$

$$2 \quad \text{EXP}(-\text{H1} \cdot \text{FB} \cdot \text{X}) / (\text{H1} \cdot (\text{H1} - 1)^2)$$

C 4TH ORDER EQUIVALENTS

$$\text{C G2211} = \text{G1122}$$

$$\text{C G1212} = \text{G2121}$$

$$\text{C G1221} = \text{G2112}$$

$$\text{C G1121} = \text{G1112} = \text{G2111} = \text{G1211}$$

$$\text{C G2221} = \text{G2122} = \text{G2212} = \text{G1222}$$

$$\text{C G11BB} = \text{GBB11}$$

$$\text{C G1B1B} = \text{GB1B1}$$

$$\text{C G1BB1} = \text{GB11B}$$

$$\text{C G22BB} = \text{GBB22}$$

$$\text{C G2B2B} = \text{GB2B2}$$

$$\text{C G2BB2} = \text{GB22B}$$

$$\text{C GBB12} = \text{G12BB} = \text{GBB21} = \text{G21BB} \quad (\text{H2} \ \& \ \text{H3})$$

$$\text{C GB12B} = \text{GB21B} = \text{G2BB1} = \text{G1BB2} \quad (\text{H1} \ \& \ \text{H2})$$

$$\text{C GB1B2} = \text{GB2B1} = \text{G2B1B} = \text{G1B2B} \quad (\text{H1} \ \& \ \text{H3})$$

$$\text{C G111B} = \text{GB111} = \text{G1B11} = \text{G11B1}$$

$$\text{C G222B} = \text{GB222} = \text{G2B22} = \text{G22B2}$$

$$\text{C G11B2} = \text{G112B} = \text{G2B11} = \text{GB211}$$

$$\text{C G1B12} = \text{G121B} = \text{G21B1} = \text{GB121}$$

C G1B21 = G12B1 = GB112 = G211B

C G22B1 = G221B = G1B22 = GB122

C G2B21 = G212B = GB212 = G12B2

C G2B12 = G21B2 = G122B = GB221

C GBBB1 = GBB1B = GB1BB = G1BBB

C GBBB2 = G2BBB = GB2BB = GBB2B

ENDIF

IF(H2.EQ.0.0.OR.H2.EQ.4.0)THEN

C FOURTH ORDER H2 TERMS

C H = 0 CONTRIBUTIONS

G1111(2) = 8.*((F1*X)**2/2. - 2.*F1*X - F1*X*EXP(-F1*X)

1 + 3.*(1. - EXP(-F1*X)))

G2222(2) = 8.*((F2*X)**2/2. - 2.*F2*X - F2*X*EXP(-F2*X)

1 + 3.*(1. - EXP(-F2*X)))

GBBBB(2) = 8.*((FB*X)**2/2. - 2.*FB*X - FB*X

1 *EXP(-FB*X) + 3.*(1. - EXP(-FB*X)))

G1112(2) = 2.*EXP(-FB*X)*FF2*(2.*(EXP(-F1*X) - 1.) +

1 F1*X*(1. + EXP(-F1*X)))

$$G111B(2) = 2.*FFB*(2.*(EXP(-F1*X) - 1.) +$$

$$1 \quad F1*X*(1. + EXP(-F1*X)))$$

$$G2221(2) = 2.*EXP(-FB*X)*FF1*(2.*(EXP(-F2*X) - 1.) +$$

$$1 \quad F2*X*(1. + EXP(-F2*X)))$$

$$G222B(2) = 2.*FFB*(2.*(EXP(-F2*X) - 1.) +$$

$$1 \quad F2*X*(1. + EXP(-F2*X)))$$

$$GBBB2(2) = 2.*FF2*(2.*(EXP(-FB*X) - 1.) +$$

$$1 \quad FB*X*(1. + EXP(-FB*X)))$$

$$GBBB1(2) = 2.*FF1*(2.*(EXP(-FB*X) - 1.) +$$

$$1 \quad FB*X*(1. + EXP(-FB*X)))$$

$$G1212(2) = DF1*DF2$$

$$G1B1B(2) = DF1*DFB$$

$$G2B2B(2) = DF2*DFB$$

$$G1B12(2) = FFB*FF2*DF1$$

$$G2B21(2) = FFB*FF1*DF2$$

$$GBB12(2) = FF2*FF1*(1. - EXP(-FB*X) -$$

$$1 \quad FB*X*EXP(-FB*X))$$

ELSE IF(H2.EQ.1.0.OR.H2.EQ.3.0)THEN

C H = 1 CONTRIBUTIONS

$$G1111(2) = 8.*(F1*X + 2.*F1*X*EXP(-F1*X) + (F1*X)**2*$$

$$1 \quad EXP(-F1*X)/2. + 3.*(EXP(-F1*X) - 1.))$$

$$G2222(2) = 8.*(F2*X + 2.*F2*X*EXP(-F2*X) + (F2*X)**2*$$

$$1 \quad EXP(-F2*X)/2. + 3.*(EXP(-F2*X) - 1.))$$

$$GBBBBB(2) = 8.*(FB*X + 2.*FB*X*EXP(-FB*X) +$$

$$1 \quad (FB*X)**2*EXP(-FB*X)/2. + 3.*(EXP(-FB*X) - 1.))$$

$$G1212(2) = 4.*EXP(-FB*X)*(1. - EXP(-F1*X) - F1*X*$$

$$1 \quad EXP(-F1*X))*(1. - EXP(-F2*X) - F2*X*EXP(-F2*X))$$

$$G1B1B(2) = 4.*(1. - EXP(-F1*X) - F1*X*$$

$$1 \quad EXP(-F1*X))*(1. - EXP(-FB*X) - FB*X*EXP(-FB*X))$$

$$G2B2B(2) = 4.*(1. - EXP(-FB*X) - FB*X*$$

$$1 \quad EXP(-FB*X))*(1. - EXP(-F2*X) - F2*X*EXP(-F2*X))$$

$$G1112(2) = 2.*EXP(-FB*X)*FF2*(1. - EXP(-F1*X) -$$

$$1 \quad F1*X*EXP(-F1*X) - (F1*X)**2*EXP(-F1*X)/2.)$$

$$G111B(2) = 2.*FFB*(1. - EXP(-F1*X) -$$

$$1 \quad F1*X*EXP(-F1*X) - (F1*X)**2*EXP(-F1*X)/2.)$$

$$G222B(2) = 2.*FFB*(1. - EXP(-F2*X) -$$

$$1 \quad F2*X*EXP(-F2*X) - (F2*X)**2*EXP(-F2*X)/2.)$$

$$G2221(2) = 2.*EXP(-FB*X)*FF1*(1. - EXP(-F2*X) -$$

$$1 \quad F2*X*EXP(-F2*X) - (F2*X)**2*EXP(-F2*X)/2.)$$

$$GBBB2(2) = 2.*FF2*(1. - EXP(-FB*X) -$$

$$1 \quad FB*X*EXP(-FB*X) - (FB*X)**2*EXP(-FB*X)/2.)$$

$$GBBB1(2) = 2.*FF1*(1. - EXP(-FB*X) -$$

$$1 \quad FB*X*EXP(-FB*X) - (FB*X)**2*EXP(-FB*X)/2.)$$

$$GBB12(2) = FF2*FF1*(FB*X)**2*EXP(-FB*X)/2.$$

$$G1B12(2) = 2.*FB*X*FF2*EXP(-FB*X)*(1.-EXP(-F1*X)$$

$$1 \quad - F1*X*EXP(-F1*X))$$

$$G2B21(2) = 2.*FB*X*FF1*EXP(-FB*X)*(1.-EXP(-F2*X)$$

$$1 \quad - F2*X*EXP(-F2*X))$$

ELSE

$$G1111(2) = 8.*(F1*X/H2 + (2.*H2-3.)*EXP(-F1*X)/(1.-H2)**2 -$$

$$1 \quad (2.*H2+1.)/H2**2 + EXP(-H2*F1*X)/(H2*(1.-H2))**2$$

$$2 \quad - F1*X*EXP(-F1*X)/(1.-H2))$$

$$G2222(2) = 8.*(F2*X/H2 + (2.*H2-3.)*EXP(-F2*X)/(1.-H2)**2 -$$

$$1 \quad (2.*H2+1.)/H2**2 + EXP(-H2*F2*X)/(H2*(1.-H2))**2$$

$$2 \quad - F2*X*EXP(-F2*X)/(1.-H2))$$

$$GBBBBB(2) = 8.*(FB*X/H2 + (2.*H2-3.)*EXP(-FB*X)/(1.-H2)**2 -$$

$$1 \quad (2.*H2+1.)/H2**2 + EXP(-H2*FB*X)/(H2*(1.-H2))**2$$

$$2 \quad - FB*X*EXP(-FB*X)/(1.-H2))$$

$$G1212(2) = 4.*(1./H2 + EXP(-H2*F1*X)/(H2*(H2-1.)) +$$

$$1 \quad \text{EXP}(-F1*X)/(1.-H2))*(1./H2 + \text{EXP}(-H2*F2*X)/(H2*(H2-1.))$$

$$2 \quad + \text{EXP}(-F2*X)/(1.-H2))*\text{EXP}(-H2*FB*X)$$

$$G1112(2) = 2.*FF2*\text{EXP}(-FB*X)*(1./H2 +$$

$$1 \quad (2.-H2)*\text{EXP}(-F1*X)/(H2-1.)**2 + F1*X*\text{EXP}(-F1*X)/$$

$$2 \quad (1.-H2) - \text{EXP}(-H2*F1*X)/(H2*(H2-1.)**2))$$

$$G2221(2) = 2.*FF1*\text{EXP}(-FB*X)*(1./H2 +$$

$$1 \quad (2.-H2)*\text{EXP}(-F2*X)/(H2-1.)**2 + F2*X*\text{EXP}(-F2*X)/$$

$$2 \quad (1.-H2) - \text{EXP}(-H2*F2*X)/(H2*(H2-1.)**2))$$

$$G1B1B(2) = 4.*(1./H2 + \text{EXP}(-H2*F1*X)/(H2*(H2-1.)) +$$

$$1 \quad \text{EXP}(-F1*X)/(1.-H2))*(1./H2 + \text{EXP}(-H2*FB*X)/(H2*(H2-1.))$$

$$2 \quad + \text{EXP}(-FB*X)/(1.-H2))$$

$$G2B2B(2) = 4.*(1./H2 + \text{EXP}(-H2*F2*X)/(H2*(H2-1.)) +$$

$$1 \quad \text{EXP}(-F2*X)/(1.-H2))*(1./H2 + \text{EXP}(-H2*FB*X)/(H2*(H2-1.))$$

$$2 \quad + \text{EXP}(-FB*X)/(1.-H2))$$

$$G111B(2) = FF2*FF1*(\text{EXP}(-H2*FB*X)-\text{EXP}(-FB*X)$$

$$1 \quad + (H2-1.)*FB*X*\text{EXP}(-FB*X))/(H2-1.)**2$$

$$G111B(2) = 2.*FFB*(1./H2 +(2.-H2)*\text{EXP}(-F1*X)/(H2-1.)**2 +$$

$$1 \quad F1*X*\text{EXP}(-F1*X)/(1.-H2) -$$

$$2 \quad \text{EXP}(-H2*F1*X)/(H2*(H2-1.)**2))$$

$$G222B(2) = 2.*FFB*(1./H2 +(2.-H2)*\text{EXP}(-F2*X)/(H2-1.)**2 +$$

$$1 \quad F2*X*\text{EXP}(-F2*X)/(1.-H2) -$$

$$2 \quad \text{EXP}(-H2*F2*X)/(H2*(H2-1.)**2))$$

$$G1B12(2) = 2.*FF2*(EXP(-H2*FB*X) - EXP(-FB*X))*$$

$$1 \quad (1./H2 - EXP(-H2*F1*X)/(H2*(1.-H2)) + EXP(-F1*X)/$$

$$2 \quad (1.-H2))$$

$$G2B21(2) = 2.*FF1*(EXP(-H2*FB*X) - EXP(-FB*X))*$$

$$1 \quad (1./H2 - EXP(-H2*F2*X)/(H2*(1.-H2)) + EXP(-F2*X)/$$

$$2 \quad (1.-H2))$$

$$GBBB1(2) = 2.*FF1*(1./H2 + (2.-H2)*EXP(-FB*X)/(H2-1.)**2 +$$

$$1 \quad FB*X*EXP(-FB*X)/(1.-H2) -$$

$$2 \quad EXP(-H2*FB*X)/(H2*(H2-1.)**2))$$

$$GBBB2(2) = 2.*FF2*(1./H2 + (2.-H2)*EXP(-FB*X)/(H2-1.)**2 +$$

$$1 \quad FB*X*EXP(-FB*X)/(1.-H2) -$$

$$2 \quad EXP(-H2*FB*X)/(H2*(H2-1.)**2))$$

ENDIF

IF(H3.EQ.0.0.OR.H3.EQ.4.0)THEN

C H3 FOURTH ORDER TERMS

C H = 0 CONTRIBUTIONS

$$G1111(3) = 8.*((F1*X)**2/2. - 2.*F1*X - F1*X*EXP(-F1*X)$$

$$1 \quad + 3.*(1. - EXP(-F1*X)))$$

$$G2222(3) = 8.*((F2*X)**2/2. - 2.*F2*X - F2*X*EXP(-F2*X)$$

$$1 \quad + 3.*(1. - EXP(-F2*X)))$$

```

GBBBB(3) = 8.*((FB*X)**2/2. - 2.*FB*X - FB*X
1  *EXP(-FB*X) + 3.*(1. - EXP(-FB*X)))

G1112(3) = 2.*EXP(-FB*X)*FF2*(2.*(EXP(-F1*X) - 1.) +
1  F1*X*(1. + EXP(-F1*X)))

G111B(3) = 2.*FFB*(2.*(EXP(-F1*X) - 1.) +
1  F1*X*(1. + EXP(-F1*X)))

G2221(3) = 2.*EXP(-FB*X)*FF1*(2.*(EXP(-F2*X) - 1.) +
1  F2*X*(1. + EXP(-F2*X)))

G222B(3) = 2.*FFB*(2.*(EXP(-F2*X) - 1.) +
1  F2*X*(1. + EXP(-F2*X)))

GBBB2(3) = 2.*FF2*(2.*(EXP(-FB*X) - 1.) +
1  FB*X*(1. + EXP(-FB*X)))

GBBB1(3) = 2.*FF1*(2.*(EXP(-FB*X) - 1.) +
1  FB*X*(1. + EXP(-FB*X)))

G1221(3) = DF1*DF2

G1BB1(3) = DF1*DFB

G2BB2(3) = DF2*DFB

G1B21(3) = FFB*FF2*DF1

G2B12(3) = FFB*FF1*DF2

GBB12(3) = FF2*FF1*(1. - EXP(-FB*X) -
1  FB*X*EXP(-FB*X))

ELSE IF(H3.EQ.1.0.OR.H3.EQ.3.0)THEN

```

C H = 1 CONTRIBUTIONS

$$G1111(3) = 8. * (F1 * X + 2. * F1 * X * EXP(-F1 * X) + (F1 * X) ** 2 * EXP(-F1 * X) / 2. + 3. * (EXP(-F1 * X) - 1.))$$

$$G2222(3) = 8. * (F2 * X + 2. * F2 * X * EXP(-F2 * X) + (F2 * X) ** 2 * EXP(-F2 * X) / 2. + 3. * (EXP(-F2 * X) - 1.))$$

$$GBBBBB(3) = 8. * (FB * X + 2. * FB * X * EXP(-FB * X) + (FB * X) ** 2 * EXP(-FB * X) / 2. + 3. * (EXP(-FB * X) - 1.))$$

$$G1221(3) = 4. * EXP(-FB * X) * (1. - EXP(-F1 * X) - F1 * X * EXP(-F1 * X)) * (1. - EXP(-F2 * X) - F2 * X * EXP(-F2 * X))$$

$$G1BB1(3) = 4. * (1. - EXP(-F1 * X) - F1 * X * EXP(-F1 * X)) * (1. - EXP(-FB * X) - FB * X * EXP(-FB * X))$$

$$G2BB2(3) = 4. * (1. - EXP(-FB * X) - FB * X * EXP(-FB * X)) * (1. - EXP(-F2 * X) - F2 * X * EXP(-F2 * X))$$

$$G1112(3) = 2. * EXP(-FB * X) * FF2 * (1. - EXP(-F1 * X) - F1 * X * EXP(-F1 * X) - (F1 * X) ** 2 * EXP(-F1 * X) / 2.)$$

$$G111B(3) = 2. * FFB * (1. - EXP(-F1 * X) - F1 * X * EXP(-F1 * X) - (F1 * X) ** 2 * EXP(-F1 * X) / 2.)$$

$$G222B(3) = 2. * FFB * (1. - EXP(-F2 * X) - F2 * X * EXP(-F2 * X) - (F2 * X) ** 2 * EXP(-F2 * X) / 2.)$$

$$G2221(3) = 2. * EXP(-FB * X) * FF1 * (1. - EXP(-F2 * X) - F2 * X * EXP(-F2 * X) - (F2 * X) ** 2 * EXP(-F2 * X) / 2.)$$

$$G\text{BBB}2(3) = 2.*FF2*(1. - \text{EXP}(-FB*X) -$$

$$1 \quad FB*X*\text{EXP}(-FB*X) - (FB*X)**2*\text{EXP}(-FB*X)/2.)$$

$$G\text{BBB}1(3) = 2.*FF1*(1. - \text{EXP}(-FB*X) -$$

$$1 \quad FB*X*\text{EXP}(-FB*X) - (FB*X)**2*\text{EXP}(-FB*X)/2.)$$

$$G\text{BB}12(3) = FF2*FF1*(FB*X)**2*\text{EXP}(-FB*X)/2.$$

$$G1B21(3) = 2.*FB*X*FF2*\text{EXP}(-FB*X)*(1.-\text{EXP}(-F1*X)$$

$$1 \quad - F1*X*\text{EXP}(-F1*X))$$

$$G2B12(3) = 2.*FB*X*FF1*\text{EXP}(-FB*X)*(1.-\text{EXP}(-F2*X)$$

$$1 \quad - F2*X*\text{EXP}(-F2*X))$$

ELSE

$$G1111(3) = 8.*(F1*X/H3 + (2.*H3-3.)*\text{EXP}(-F1*X)/(1.-H3)**2$$

$$1 \quad - (2.*H3+1.)/H3**2 + \text{EXP}(-H3*F1*X)/(H3*(1.-H3))**2$$

$$2 \quad - F1*X*\text{EXP}(-F1*X)/(1.-H3))$$

$$G2222(3) = 8.*(F2*X/H3 + (2.*H3-3.)*\text{EXP}(-F2*X)/(1.-H3)**2$$

$$1 \quad - (2.*H3+1.)/H3**2 + \text{EXP}(-H3*F2*X)/(H3*(1.-H3))**2$$

$$2 \quad - F2*X*\text{EXP}(-F2*X)/(1.-H3))$$

$$G\text{BBBB}(3) = 8.*(FB*X/H3 + (2.*H3-3.)*\text{EXP}(-FB*X)/(1.-H3)**2$$

$$1 \quad - (2.*H3+1.)/H3**2 + \text{EXP}(-H3*FB*X)/(H3*(1.-H3))**2$$

$$2 \quad - FB*X*\text{EXP}(-FB*X)/(1.-H3))$$

$$G1221(3) = 4. * (1./H3 + EXP(-H3*F1*X))/(H3*(H3-1.))$$

$$1 \quad + EXP(-F1*X)/(1.-H3)) * (1./H3 + EXP(-H3*F2*X)/$$

$$2 \quad (H3*(H3-1.)) + EXP(-F2*X)/(1.-H3)) * EXP(-H3*FB*X)$$

$$G1112(3) = 2. * FF2 * EXP(-FB*X) * (1./H3 +$$

$$1 \quad (2.-H3) * EXP(-F1*X)/(H3-1.) ** 2 + F1 * X * EXP(-F1*X)/$$

$$2 \quad (1.-H3) - EXP(-H3*F1*X)/(H3*(H3-1.) ** 2))$$

$$G2221(3) = 2. * FF1 * EXP(-FB*X) * (1./H3 +$$

$$1 \quad (2.-H3) * EXP(-F2*X)/(H3-1.) ** 2 + F2 * X * EXP(-F2*X)/$$

$$2 \quad (1.-H3) - EXP(-H3*F2*X)/(H3*(H3-1.) ** 2))$$

$$G1BB1(3) = 4. * (1./H3 + EXP(-H3*F1*X))/(H3*(H3-1.))$$

$$1 \quad + EXP(-F1*X)/(1.-H3)) * (1./H3 + EXP(-H3*FB*X)/$$

$$2 \quad (H3*(H3-1.)) + EXP(-FB*X)/(1.-H3))$$

$$G2BB2(3) = 4. * (1./H3 + EXP(-H3*F2*X))/(H3*(H3-1.))$$

$$1 \quad + EXP(-F2*X)/(1.-H3)) * (1./H3 + EXP(-H3*FB*X)/$$

$$2 \quad (H3*(H3-1.)) + EXP(-FB*X)/(1.-H3))$$

$$GBB12(3) = FF2*FF1*(EXP(-H3*FB*X)$$

$$1 \quad -EXP(-FB*X) + (H3-1.)*FB*X*EXP(-FB*X))$$

$$2 \quad /((H3-1.)**2)$$

$$G111B(3) = 2.*FFB*(1./H3 + (2.-H3)*EXP(-F1*X)/(H3-1.)**2$$

$$1 \quad + F1*X*EXP(-F1*X)/(1.-H3) -$$

$$2 \quad EXP(-H3*F1*X)/(H3*(H3-1.)**2))$$

$$G222B(3) = 2.*FFB*(1./H3 + (2.-H3)*EXP(-F2*X)/(H3-1.)**2$$

$$1 \quad + F2*X*EXP(-F2*X)/(1.-H3) -$$

$$2 \quad EXP(-H3*F2*X)/(H3*(H3-1.)**2))$$

$$G1B21(3) = 2.*FF2*(EXP(-H3*FB*X) - EXP(-FB*X))*(1./H3 -$$

$$1 \quad EXP(-H3*F1*X)/(H3*(1.-H3)) + EXP(-F1*X)/(1.-H3))$$

$$G2B12(3) = 2.*FF1*(EXP(-H3*FB*X) - EXP(-FB*X))*(1./H3 -$$

$$1 \quad EXP(-H3*F2*X)/(H3*(1.-H3)) + EXP(-F2*X)/(1.-H3))$$

$$GBBB1(3) = 2.*FF1*(1./H3 + (2.-H3)*EXP(-FB*X)/(H3-1.)**2$$

$$1 \quad + FB*X*EXP(-FB*X)/(1.-H3) -$$

$$2 \quad EXP(-H3*FB*X)/(H3*(H3-1.)**2))$$

$$GBBB2(3) = 2.*FF2*(1./H3 + (2.-H3)*EXP(-FB*X)/(H3-1.)**2$$

$$1 \quad + FB*X*EXP(-FB*X)/(1.-H3) -$$

$$2 \quad EXP(-H3*FB*X)/(H3*(H3-1.)**2))$$

ENDIF

C 4TH ORDER AB MATRIX ELEMENTS

$$GAAAA = G1111(1) + G1111(2) + G1111(3) +$$

$$1 \quad G2222(1) + G2222(2) + G2222(3) + 2.*(G1122(1) +$$

$$2 \quad G1212(2) + G1221(3)) + 4.*(G1112(1) + G1112(2) +$$

$$3 \quad G1112(3) + G2221(1) + G2221(2) + G2221(3))$$

$$RBBBBB = GBBBB(1) + GBBBB(2) + GBBBB(3)$$

$$GBBBA = GBBB1(1) + GBBB1(2) + GBBB1(3) +$$

$$1 \quad GBBB2(1) + GBBB2(2) + GBBB2(3)$$

$$GBBAA = G11BB(1) + G22BB(1) + 2.*(GBB12(2) +$$

$$1 \quad GBB12(3))$$

$$GBAAB = G1BB1(3) + G2BB2(3) + 2.*(GB12B(1) +$$

$$1 \quad GBB12(2))$$

$$GBABA = G1B1B(2) + G2B2B(2) + 2 \cdot (GB12B(1) + 1 \cdot GBB12(3))$$

$$GAAAB = G111B(1) + G111B(2) + G111B(3) + 1 \cdot G222B(1) + G222B(2) + G222B(3) + G11B2(1) + 2 \cdot G1B12(2) + G1B21(3) + G22B1(1) + G2B21(2) + 3 \cdot G2B12(3)$$

C 4TH ORDER Gijkl EQUIVALENTS

$$C \quad GBBAB = GBBBA$$

$$C \quad GBABB = GBBBA$$

$$C \quad GABBB = GBBBA$$

$$C \quad GAABB = GBBAA$$

$$C \quad GABBA = GBAAB$$

$$C \quad GABAB = GBABA$$

$$C \quad GABAA = GAAAB$$

$$C \quad GBAAA = GAAAB$$

$$C \quad GAABA = GAAAB$$

C GAMMA 4 CONTRIBUTIONS

DO 2000 I=1,16

GIJKL(1) = GAAAA

GIJKL(2) = GAAAB

GIJKL(3) = GIJKL(2)

GIJKL(4) = GBBAA

GIJKL(5) = GIJKL(2)

GIJKL(6) = GBABA

GIJKL(7) = GBAAB

GIJKL(8) = GBBBA

GIJKL(9) = GIJKL(2)

GIJKL(10) = GIJKL(7)

GIJKL(11) = GIJKL(6)

GIJKL(12) = GIJKL(8)

GIJKL(13) = GIJKL(4)

GIJKL(14) = GIJKL(8)

GIJKL(15) = GIJKL(8)

GIJKL(16) = RGBBBB

LAM(1) = LAMA**4

LAM(2) = LAMA**3*LAMB

LAM(3) = LAM(2)

LAM(4) = LAMA**2*LAMB**2

LAM(5) = LAM(2)

LAM(6) = LAM(4)

LAM(7) = LAM(4)

LAM(8) = LAMB**3*LAMA

LAM(9) = LAM(2)

LAM(10) = LAM(4)

LAM(11) = LAM(4)

LAM(12) = LAM(8)

LAM(13) = LAM(4)

LAM(14) = LAM(8)

LAM(15) = LAM(8)

LAM(16) = LAMB**4

GAMMA4(I) = (GAM(I) - GIJKL(I))*X**4*LAM(I)

FOURTH(A) = FOURTH(A) + GAMMA4(I)

2000 CONTINUE

C WRITE(5,*) 'GAMMA 4 =',FOURTH(A)

2500 CONTINUE

LAM4 = 6.*FOURTH(1)

HEX3 = 2.3094*THIRD

HEX4 = 2.*(FOURTH(1) + 4.*FOURTH(2))

BCC3 = 3.26599*THIRD

BCC4 = FOURTH(1) + 8.*FOURTH(2) + 2.*FOURTH(3)

1 + 4.*FOURTH(4)

TRANS1 = SPIN - HEX3**2/(12.*HEX4)

TRANS2 = SPIN - BCC3**2/(12.*BCC4)

C CONTINUOUS TRANSITION POINTS IN FILE 11

IF(SPIN-TRANS2.LE..0001)THEN

! WRITE(11,*) TAU,F,SPIN

ENDIF

WRITE(2,*) 'DIS/HEX',TRANS1,'DIS/BCC',TRANS2

WRITE(3,*) TRANS2,SPIN,X

```
WRITE(4,*) X,F
```

```
stop
```

```
end
```

CHAPTER 5: Asymmetric block copolymers at immiscible polymer/polymer interfaces

5.1 Block copolymer architecture

While immiscible homopolymers commonly undergo phase separation at macroscopic length scales, incorporation of a covalent linkage between two such homopolymers to form a diblock copolymer can have dramatic consequences for phase separation at significantly reduced length scales.^{1,2} The important parameters to consider in the design of AB block copolymers are volume fraction (f_A , the number fraction of A repeat units), which can be also referred as block asymmetry, chemical composition and block incompatibility (χN) defined as a product of the Flory-Huggins parameter (χ) and the chain length (N). These materials self-assemble and form periodic nanoscale morphologies, whose symmetry and sizes depend on factors such as chemical identity, molecular composition, molecular weight and temperature.¹⁻⁸ These self-organizing materials are of great interest due to variety of applications in engineered-surfaces, biomaterials, membranes and are highly studied in multicomponent systems of homopolymer/copolymer mixtures in confined geometries such as polymer thin-films (thicknesses ≈ 100 -500 nm) as studied here.

In the presence of a parent homopolymer, copolymer molecules at sufficiently high concentration form micelles and segregate to existing interfaces.^{2,4-7,9-19} Previous studies of Wei *et al.*^{20,21} have established that the dewetting kinetics of a copolymer-containing thin polymer film on an immiscible polymer substrate can be tuned by varying the concentration of a molecularly-symmetric copolymer (*ca.* Fig. 5.1). Taking the earlier findings into consideration, we have extended the studies of macroscopic dewetting behavior to molecular-

level phenomena by introducing the block compositional asymmetry into copolymer self-organization and polymer/polymer interfacial modification.

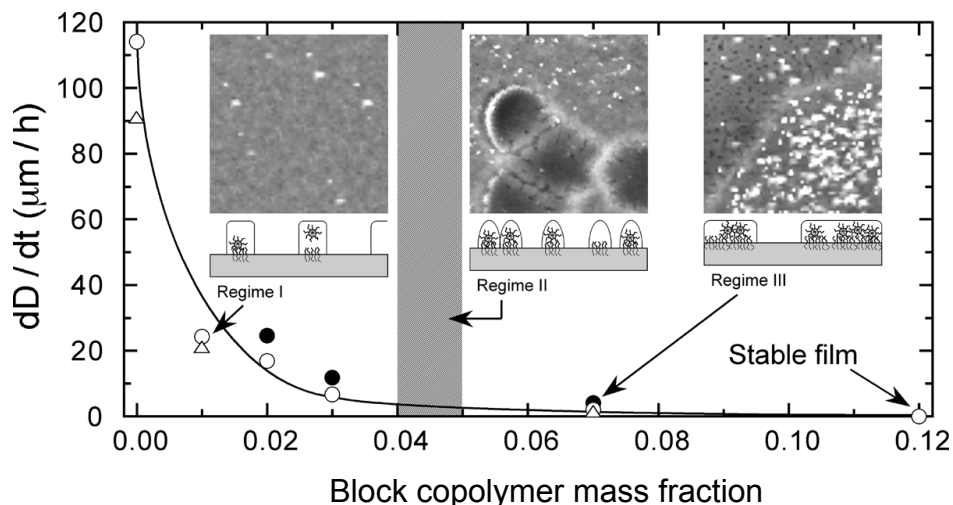


Figure 5.1 Copolymer-induced changes in dewetting mechanism presented with the macroscopic dewetting rate (dD/dt) and AFM height images (5 mm x 5 mm) of the polymer/polymer interface after selective dissolution of the top layer. The different symbols correspond to results from different analyses of the data.²⁰

5.2 Overview on block copolymer micelles and critical micelle concentration (CMC)

Block copolymer micelles are generated by (i) copolymers that are molecularly dissolved in a solvent, which is selective for one of the blocks and poor to the other, and, then (ii) a change in external stimuli (i.e., a change in temperature, composition of the solvent etc.). Concentration of copolymer molecules also plays a major role in micellization.

One of the most important characteristics of copolymer micellization is indicated by the critical micelle concentration (CMC), above which, copolymer molecules exist as micelles, as well as in single-chain form (*ca.* Fig. 5.2 (top)). As the concentration reaches this

critical value, copolymer chains start interacting with each other and forming nanostructures called “micelles” in order to avoid unfavorable interaction between the solvophobic part of the copolymer molecules and the surrounding media (i.e., solvent or homopolymer molecules). At this critical concentration, solvent molecules can be found to interact with the corona of the micelles which forces micelles to form loose aggregates in larger size than the ones formed at higher concentrations. Once the concentration is sufficiently high, most of the block copolymer molecules are found in micellar form, a low-energy-state configuration (*ca.* Fig. 5.2 (bottom)). The solvent molecules will eventually be pushed out completely resulting in a decrease in micelle size.

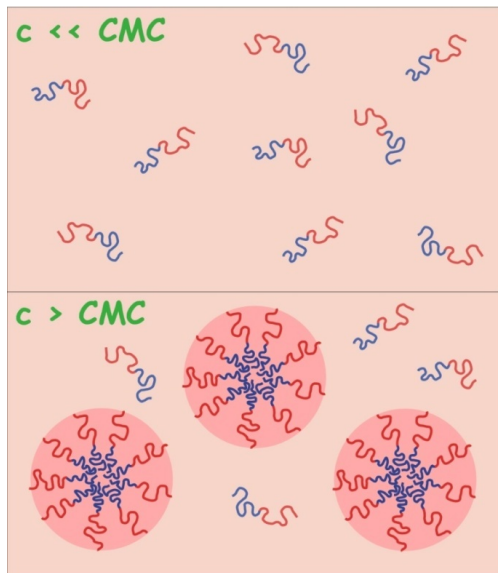


Figure 5.2 Illustration of an AB diblock copolymer molecules (A: red , B: blue) in an A-selective solvent. At concentrations much lower than the CMC (top), copolymer molecules exhibit single chains, and at concentrations that are higher than the CMC (bottom), copolymer molecules tend to form micellar structures and minimize the interactions between the hydrophobic core and the surrounding solvent molecules.

In principle, the CMC of copolymers can be determined by physical methods such as osmotic pressure, electrical conductivity or surface tension measurements that are sensitive to sudden changes in physico-chemical properties of polymer solution at or near the CMC. The CMC values for the asymmetric copolymers utilized in this study were determined from two methods: (i) dry-brush theory developed by Leibler²³⁻²⁵, and (ii) self-consistent field theory developed by Duque.²⁶ CMC values calculated by the first method mentioned above have been obtained under the assumption that the corona of the micelles remains “dry”; i.e., large homopolymer cannot penetrate through the dense corona due to disparities in molecular weight. This also means that the CMC values are independent of the molecular weight in which the SM copolymer molecules are embedded. Details of these calculations are presented in two sections in Appendices 5.A and 5.B.

The morphology of block copolymer micelles can be investigated by methods: transmission electron microscopy (TEM), small angle neutron scattering (SANS), small angle X-ray scattering (SAXS) and atomic force microscopy (AFM). Common morphologies for micelles as reported by Price, Esselink and Lam *et al.*^{27,28} show spherical shape; depending on the block asymmetry, thus, incompatibility. Morphologies may vary such as ellipsoidal, flower-like, vesicles, crew-cut micelles, rod-like micelles.^{14,29-31} In cases of some of these nanostructures being responsive to external stimuli such as a change in temperature, for instance, can cause spherical micelles of block copolymers to transform into worm-like (cylindrical) micelles or even nanotubes.³²⁻³⁴ If a micelle contacts a surface, it may break, allowing the copolymer molecules to adopt a more thermodynamically-favored conformation

along the surface. In some cases, such rearrangement may lead to morphologies, such as lamellae.³⁵ Zhulina and Birshstein³⁶ and Halperin³⁷ observed morphologies of micelles in star shape. These micelles are spherical with small core and expanded corona, and form when the length of soluble block is considerably longer than that of the insoluble block. One type of nanostructures we have hypothesized of accounting for in this study, are micelles with large cores and short coronas, called as “*crew-cut*” which are formed by asymmetric block copolymers with relatively long insoluble blocks, as reported earlier by Nagarajan,³⁸ and later by Eisenberg³⁹ and their coworkers.

5.3 Motivation for this study

In the present study, we investigate the interfacial partitioning and the effect of copolymer compositional asymmetry of poly(styrene-*b*-methyl methacrylate) (SM) diblock on the stability of thin planar films of polystyrene (PS) and poly(methyl methacrylate) (PMMA) homopolymers. At all concentrations (above the CMC) probed, the block copolymer molecules exhibit aggregates, which are thermodynamically stable nanostructures that are capable of molecular reorganization in order to adopt a more thermodynamically favored arrangement along the surface. This “transient” nature of micelles makes it difficult to assess the role of assembling in discrete molecules on morphological development near surfaces/interfaces.

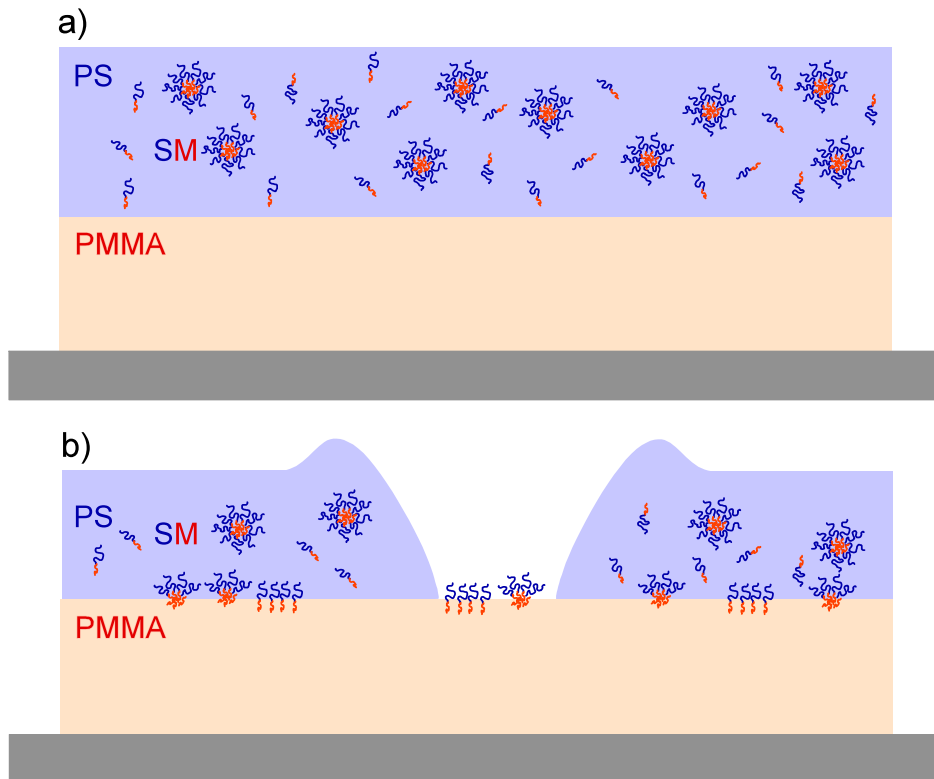


Figure 5.3 Cross-section illustration of a dewetting hole in the presence of free micelles, surface micelles and interfacial copolymer patches on the PS/PMMA double-layered assemblies investigated

Discrete nanostructures anticipated in this study include free micelles, surface micelles along the PS/PMMA interface, and PS-*b*-PMMA (SM) copolymer (brush) patches along the PS/PMMA interface. Blended with PS, the SM molecules can self-assemble into free micelles with coronas consisting of PS and cores of PMMA, distributed throughout the PS homopolymer if the SM concentration is above that of CMC.

The as-cast top layer (*cf.* Fig. 5.3a) possesses very likely a non-equilibrium morphology. Upon annealing in the melt (*cf.* Fig 5.3b), this morphology is refined as (*i*) the copolymer molecules self-organize into micelles, which migrate (along with free SM

copolymers) to the PS/PMMA interface (likely also to the film/free surface interface), thus forming brush patches along the interface and (ii) the top polymer layer dewets from the immiscible polymer substrate. The molecular weight of the top film was chosen deliberately to be much lower than the bottom substrate so that dewetting of the top layer occurs, which, thereby permits us to study SM copolymer activity at the PS/PMMA interface. While at equilibrium, the size and aggregation number of the micelles is expected to be uniform, our previous studies have demonstrated that the size of such micelles in dewetting polymer thin films varies considerably due to the temperature treatment at various time intervals. This may have an effect on the stability of the top PS layer.

Here we explore the stabilization effect of copolymer molecules on immiscible polymer/polymer assembly by changing the chemical composition the block copolymer, as well as copolymer concentration, molecular weight and film thickness of the polymer assemblies. It is anticipated the outcome of this study benefits bulk compatibilization efforts by developing a molecular-level understanding of the structuring processes that occur within close proximity to developing polymer/polymer interfaces.

5.4 Experimental

5.4.1 Materials

Three polystyrene (PS30, 50 and 216) homopolymers (the subscripts used in the nomenclature denote the number-average molecular weight, M_n , in kg/mol and polydispersity index, M_w/M_n is 1.06 for all the PS products) were purchased from Pressure Chemical, Inc.

and Polymer Source, Inc. Poly(methyl methacrylate) (PMMA243, numerical designation denotes the molecular weight in kg/mol) homopolymer and $M_w/M_n = 1.06$. Five PS-*b*-PMMA (SM) copolymers (PS₅₀-*b*-PMMA₅₄, PS₅₀-*b*-PMMA₂₀, PS₂₀-*b*-PMMA₅₀, PS₅₀-*b*-PMMA₁₀ and PS₁₀-*b*-PMMA₅₀, where the subscripted numerical designation denotes the block weight in kg/mol) were obtained from Polymer Source, Inc. (*ca.* Table 5.1). All polymeric materials were used as-received. Solvent-grade toluene, acetic acid, cyclohexane and 1-chloropentane were obtained from Fisher Scientific and Sigma Aldrich and used as-received for selective-layer removal.

Table 5.1 Molecular weight and the PDI values for the SM copolymers

PS- <i>b</i> -PMMA (SM) diblock copolymers (M_n in kDa)		M_w/M_n
9.3- <i>b</i> -51	(noted in the text as PS ₁₀ - <i>b</i> -PMMA ₅₀)	1.09
20.2- <i>b</i> -50.5	(noted in the text as PS ₂₀ - <i>b</i> -PMMA ₅₀)	1.07
50- <i>b</i> -10.5	(noted in the text as PS ₅₀ - <i>b</i> -PMMA ₁₀)	1.06
50- <i>b</i> -21	(noted in the text as PS ₅₀ - <i>b</i> -PMMA ₂₀)	1.08
50- <i>b</i> -54	(noted in the text as PS ₅₀ - <i>b</i> -PMMA ₅₄)	1.04

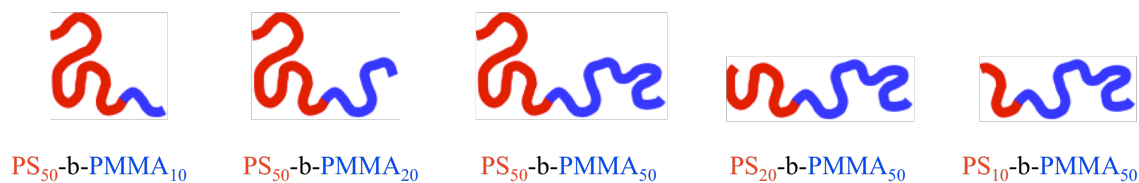


Figure 5.4 Illustration of block asymmetry in SM copolymers used in the study (PS block in red, PMMA block in blue)

5.4.2 Methods

Sample preparation methods are arranged in four main sections: (i) (PS/SM)/PMMA, and (ii) PS/(PMMA/SM) bilayers on silicon substrates, (iii) PS/SM/PMMA trilayers on silicon substrates, and (iii) self-standing films of PS/SM on TEM grids.

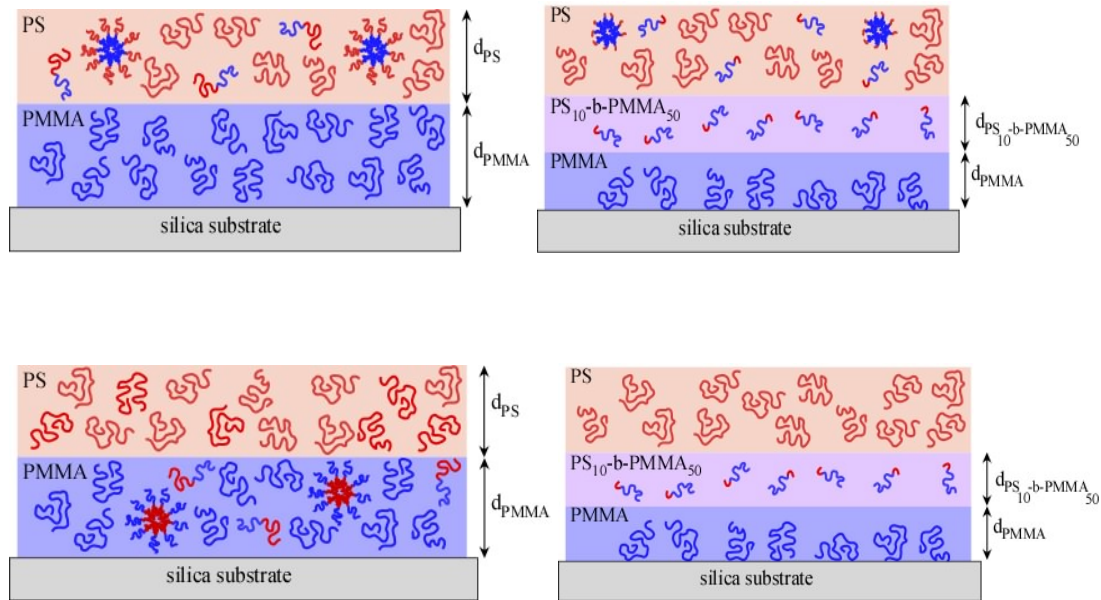


Figure 5.5 Illustrative representation laminate systems: Bilayers: (PS/SM)/PMMA (top left) and PS/(PMMA/SM) (bottom left). Trilayers: (PS/SM)/SM/PMMA (topright) and PS/SM/PMMA (bottom right).

5.4.2.1 (PS/SM)/PMMA bilayers

Solutions consisting of 1.35 wt% PMMA243 in toluene were prepared, and thin polymer films were spun-cast onto silicon wafer with a Headway spin-coater at 2000 rpm for 30 s. These conditions were crucial to ensure a constant film thickness of 50 nm for PMMA243, as discerned by ellipsometry, to permit systematic and quantitative comparison. In addition,

solutions composed of 1.45 wt% PS/SM in toluene were prepared and likewise spun-cast onto glass slides under similar conditions.

The series of SM copolymers with block weights varying systematically from 10 to 50 kg/mol was used for this purpose. In addition, the molecular weight of the PS ranged from 30 to 216 kg/mol. The mass fraction of SM copolymer in the PS layer ranged from 0.00 (pure PS) to 0.04. Since PS does not interact to any discernible extent with glass and the amount of SM copolymer in solution was relatively small. Dried PS/SM films measuring ≈ 55 -60 nm could be easily floated off on water and deposited directly on the PMMA243 substrate to form a bilayer film.

5.4.2.2 PS/(PMMA/SM) bilayers

Solutions consisting of 1.35 wt% PMMA243/SM in toluene were prepared and thin polymer films were spun-cast onto silicon wafer with a Headway spin-coater at 2000 rpm for 30 s. These conditions were crucial to ensure a constant film thickness of 50 nm for the PMMA243/SM layer, as discerned by ellipsometry, to permit systematic and quantitative comparison. In addition, solutions composed of 1.45 wt% PS50 in toluene were prepared and likewise spun-cast onto glass slides under similar conditions. The series of SM copolymers with block weights varying systematically from 10 to 50 kg/mol was used for this purpose. The mass fraction of SM copolymer in the PMMA243 layer ranged from 0 (pure PMMA243) to 0.04. Since PS50 does not interact to any discernible extent with glass and the amount of SM copolymer in solution was relatively small. Dried PS50 films measuring ≈ 55 -60 nm could

be easily floated off on water and deposited directly on the PMMA substrate to form a bilayer film.

5.4.2.3 PS/SM/PMMA and (PS/SM)/SM/PMMA trilayers on silicon substrates

Solutions consisting of 1.4 wt% PMMA243 in toluene were prepared, and thin polymer films were spun-cast onto silicon wafer with a Headway spin-coater at 2000 rpm for 30 s to ensure a constant film thickness of 54 nm for PMMA243, as discerned by ellipsometry. PMMA243 substrates were annealed for 12 hours on Mettler-Toledo hot stage under a continuous stream of nitrogen gas at 180°C. The substrates were cooled slowly down to the ambient temperature, and, then gently rinsed with toluene. The resultant film thickness measured by ellipsometry was 51 nm. One symmetric (PS₁₀-b-PMMA₅₀) and two asymmetric (PS₁₀-b-PMMA₅₀ and PS₅₀-b-PMMA₁₀) diblock copolymers were used as thin midlayers with thicknesses varied from 2.4 nm to 10 nm, were spun-cast from toluene solutions directly on the PMMA243 substrate. The samples were dried overnight. Solutions of 1.55 wt% PS30 and 1.55 wt% PS30/(0.25wt% SM) in toluene were prepared and likewise spun-cast onto glass slides under similar conditions. Dried PS30 and PS30/SM films measuring ≈60 nm could be floated off easily on water and deposited directly on the SM/PMMA243 substrate to form a trilayer film. After drying the bilayer and trilayer laminates in air at room temperature for 24 h, the samples were annealed individually at 180°C, above the glass transition temperature (T_g) of both PS (≈100°C) and PMMA (≈120°C), under a circulating N₂ flow (to avoid oxidative degradation) for pre-designated time intervals and then cooled the system below the lowest T_g. Dewetting kinetic in the top PS layer was monitored at various temperatures *in*

situ with an Olympus BX60 optical microscope equipped with a computer-interfaced CCD camera and operated in reflection mode. Surface topologies of the PMMA surface and PS/PMMA interface (after dewetting and/or selective solvent removal of PS) were examined by AFM in tapping mode on Digital Instruments 3000 and PSIA XE-100 instruments, respectively. TEM samples of the double-layer assemblies were prepared in two different ways: (i) direct spin-casting of, or (ii) floating of thin films on SiO_x-coated grids. Annealing period of these samples varied from 1 min to 30 min. The samples were exposed to the vapor of 0.5% RuO₄(aq) for 7 min in order to stain the PS phase and examined by means of a Zeiss EM902 electron spectroscopic microscope operated at 80 kV and an energy loss of 0 eV.

5.4.2.4 Self-standing thin-films of (PS/SM) on Cu TEM grids

Solutions of 1.45 wt% PS₅₀/PS₁₀-b-PMMA₅₀ and 1.45 wt% PS₁₀-b-PMMA₅₀ in toluene were prepared and likewise spun-cast onto glass slides under similar conditions as explained earlier. Dried PS/SM films measuring ≈60 nm could be floated off easily on water and deposited directly on Cu TEM grids with 1mm mesh size. The samples were dried at ambient temperature for 48 hours and then annealed at 120°C on Mettler-Toledo hot stage, under a circulating N₂ flow (to avoid oxidative degradation of PS). The grid was not touching the graphite plates as it was standing between two glass pieces on the corners providing the thin-polymer layers an air/air interface on both sides. The dewetting kinetics of both PS/SM and SM layers were monitored *in situ* with an Olympus BX60 optical microscope equipped with a computer-interfaced CCD camera and operated in reflection mode.

5.5. Results and Discussion

5.5.1 (PS/SM)/PMMA bilayers

As pure PS films dewet from PMMA substrates at temperatures far above the T_g s of both polymers, the dewetting follows the conventional route of nucleation and growth of circular holes. Upon nucleating, a hole is created in the top film and its diameter (D) grows linearly with annealing time (t); the dewetting rate (dD/dt) is constant. When the hole reaches a certain critical size (determined by the thickness of the PS layer), a rim is formed at the perimeter of the hole. When the rims of neighboring holes merge into each other they become straight ribbons; the ribbons eventually break into isolated droplets. While the linearity of the growth of the holes was found to be independent of the molecular weights of both PS and PMMA, the dewetting rate depended strongly on the PS molecular weight as can be clearly seen in Fig. 5.6a-c. When annealed at same temperature, at 180°C, PS30 dewetted faster than PS50 and PS50 dewetted much faster than PS216. This behavior was attributed to the decrease of the viscosity (η) of the top layer with decreasing molecular weight. In experiments involving high molecular weight PMMA243, AFM topography scans detected no geometrical deformation of the PS/PMMA243 interface during dewetting of PS (PS30 and PS50) from PMMA243. This finding confirmed theoretical predictions that the bottom PMMA layer behaved like a solid substrate since its viscosity was at least more than two orders of magnitude higher than that of PS30 and PS50 top layer ($\eta_{PMMA} \gg \eta_{PS}$).

Our previous studies²¹ have established that the addition of a nearly symmetric PS₅₀-*b*-PMMA₅₄ copolymer to PS50 decreased systematically the dewetting rate until the top

PS50/PS₅₀-*b*-PMMA₅₄ layer was eventually stabilized at relatively high copolymer concentrations (> 10 wt% copolymer). In addition, the time dependence of hole size was found to be nearly linear, in which case linear dewetting rates were reported. Upon closer examination of this trend in Fig. 5.6b, we find a sharp reduction in the dewetting rate at ≈ 1 wt% PS₅₀-*b*-PMMA₅₄ copolymer.

If the size of the PS block is held constant and the size of the PMMA block is varied (which reflects changes in incompatibility between the copolymer and the PS matrix and, thus, the driving force for copolymer self-assembly), several important trends are observed. First, a reduction in PMMA block size promotes greater stabilization as the dewetting rate generally decreases. Such enhanced stabilization is accompanied by a reduced driving force for micellization, which implies that the copolymer molecules can travel to and stabilize the PS/PMMA interface. Note that the PS₅₀-*b*-PMMA₁₀ copolymer with the shortest PMMA block stabilizes the assembly at < 1 wt% copolymer. In addition, a sharp drop in dewetting rate remains evident from ≈ 0.8 -1.0 wt% copolymer. Conversely, when the PS block is shortened and the driving force for micellization is increased, the dewetting rate is observed to increase (Fig. 5.6a-b). In conclusion, the results included in Fig. 5.6a-b indicate that copolymer molecules with relatively short PMMA blocks segregate readily from the PS matrix towards and reside along the PS/PMMA interface where the short PMMA blocks can mix with the bottom PMMA substrate (essentially anchor itself to the PMMA matrix).

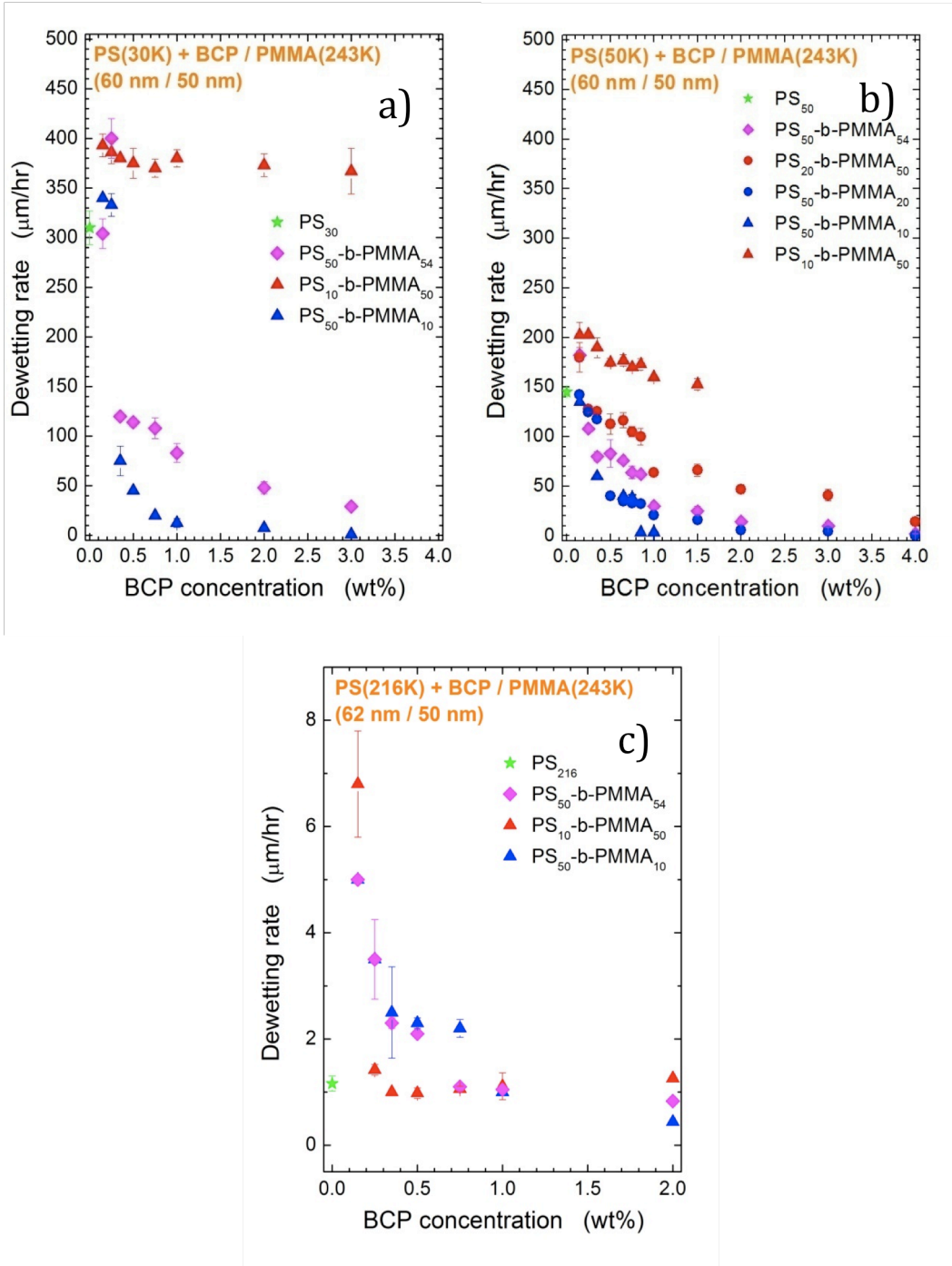


Figure 5.6 Linear dewetting rate of PS/SM on PMMA243 at 180°C as a function of SM concentration: (a) PS30, (b) PS5, (c) PS216.

Conversely, as the PS block is shortened ($\text{PS}_{10}\text{-b-PMMA}_{50}$), and the driving force for micellization is increased, we detect dewetting rates that are higher than those of the copolymer-free PS/PMMA bilayer (symbolized as “green stars” on the plots); the dewetting rate is nearly independent of the copolymer concentration (*cf.* Fig. 5.6a). This observation is contradictory to the previous findings where block copolymers are known to stabilize interfaces. This behavior can be attributed tentatively to the segregation of SM aggregates to the PS/PMMA interface, where they contribute to an increase in the PS30/PMMA243 interfacial area. Directly after spin-casting, $\text{PS}_{10}\text{-b-PMMA}_{50}$ micelles with short PS corona are formed (the micelle concentration is higher than that of free chains due to the large PMMA block). Upon annealing, aggregates and free SM molecules migrate to the PS/PMMA interface. PMMA blocks of the SM copolymer exhibit autophobic behavior with high molecular weight PMMA243 homopolymer chains; they can, however, be partially adsorbed on the PMMA243 surface, which might result in an increase the interfacial area between PS30/PMMA243. At very low concentrations of SM copolymers with large PMMA blocks added in to the PS50 layer, similar behavior is observed but in this case, different than the PS30 system, the copolymer concentration seems to have a positive effect on stability but the resulting dewetting rates are still higher than that of copolymer-free case up to 1.5 wt% $\text{PS}_{10}\text{-b-PMMA}_{50}$ (*cf.* Fig. 5.6a-b)).

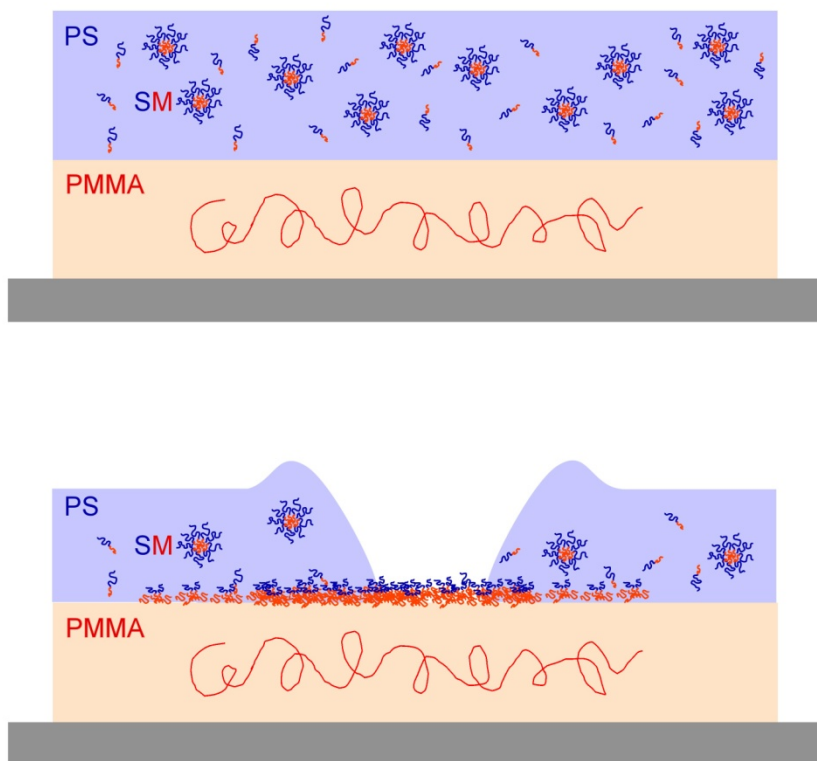


Figure 5.7 Illustration of aggregates formed by $PS_{10}\text{-}b\text{-}PMMA_{50}$ in PS30 on PMMA243 (top). Upon annealing, micelle aggregates and free SM molecules migrate to the PS/PMMA interface (bottom). PMMA blocks of the SM copolymer exhibit autophobic behavior with high molecular weight PMMA243 homopolymer chains; they can, however, be partially adsorbed on the PMMA243 surface, which might result in an increase the interfacial area between PS30/PMMA243.

After PS30/ $PS_{10}\text{-}b\text{-}PMMA_{50}$ layer dewets from PMMA243, residual PS30 layer is selectively removed with cyclohexane from the sample surface (the PMMA layer on the substrate remains intact because PMMA is not soluble in cyclohexane). The dewetted areas (inside the holes) are scanned with an AFM and PS30/PMMA243 interface demonstration of a roughened surface with a root-mean-square (RMS) roughness value of 0.7 nm at 0.15wt% $PS_{10}\text{-}b\text{-}PMMA_{50}$ molecules (RMS for pure PMMA surface is ≈ 0.45 nm). As SM amount is

further increased, the RMS roughness increases to 1.2 nm but then drops down sharply to 0.6 nm when the SM copolymer molecules amount is at 3wt%. We attribute this effect tentatively to having more SM molecules and patches located at the PS/PMMA interface, thus, stabilizing the top PS30 layer. PS/PMMA previously roughened due to interfacial heterogeneity is also reduced. In addition, we detect changes in the shape of the rim. While at higher SM concentrations the rim remains quite circular, at low SM concentrations the shape “circularity” gets distorted. This hypothesis can also be represented as shown schematically in Fig. 5.8. When adsorbing from the top PS, PS₁₀-*b*-PMMA₅₀ form “crew-cut” aggregates. The film is already structured upon annealing and these micelle aggregates adsorb at the interface but do not break instantaneously. PS30 layer dewets much faster than the micelles travelling to the interface, and not being able to break fast enough to pin the PS layer on PMMA243. As the rims of the dewetted holes hit these interfacial heterogeneities, they become non-circular. (OM PICS with inlets of 2D AFM showing the RMS values!! And next to these pics, add 3D AFM images)

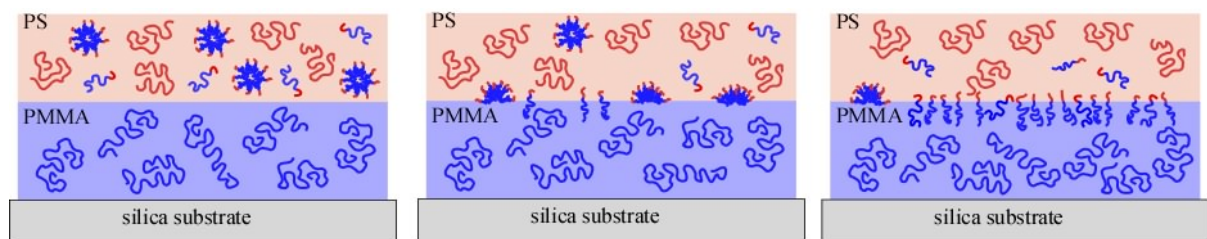


Figure 5.8 Representation of SM micelles segregating from PS30 and not having sufficient time to break and adsorb at the interface. PS30 layer dewets much faster than the micelles travelling to the interface, and not being able to break fast enough to pin the PS layer on PMMA243.

5.5.2 (PS/SM)/PMMA bilayers

Despite reversed micelle morphologies, wherein SM copolymer micelles and free chains segregate from PS homopolymer and migrate to the PS/PMMA interface in Fig. 5.6, when the same SM copolymer molecules are instead added in the bottom PMMA layer, in Fig. 5.9, we surprisingly observe a similar dewetting behavior to that of seen in Fig. 5.6.

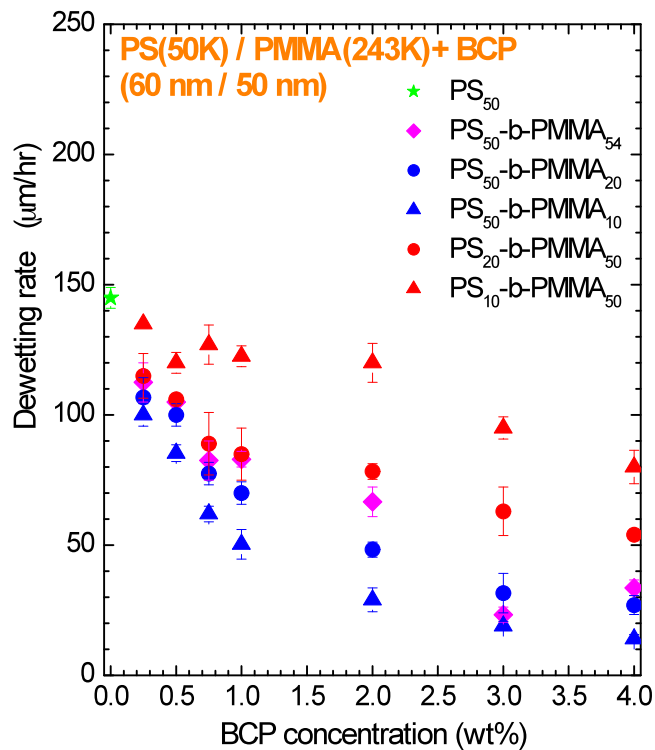


Figure 5.9 Linear dewetting rate of PS50 on PMMA243/SM at 180°C as a function of SM concentration for four different copolymers.

In both scenarios, PS₅₀-b-PMMA₁₀ copolymer molecules are the most effective at stabilizing the double-layered assembly. It should be recognized that increased driving force

for micellization in diblock copolymers possessing relatively large PS blocks (i.e. PS₅₀-b-PMMA₁₀, PS₅₀-b-PMMA₂₀ and PS₅₀-b-PMMA₅₄) might be compromised by the higher viscosity of the PMMA substrate. Also, one can speculate that the “conventional” dewetting behavior seen in silica/PMMA243/PS50 may be associated with a higher stability of the PMMA243 layer on the substrate due to well-documented strong interactions between PMMA and silica. PMMA is physically anchored on silica substrate upon spin-casting as opposed to when the molecules are added in the PS homopolymer) but high viscosity disparity between PS and PMMA (viscosity of PMMA is almost 2 orders of magnitude higher than that of PS) might offset this effect.

When PS₁₀-b-PMMA₅₀ copolymer molecules are added in the bottom PMMA243 layer, we do not observe an increase in top PS layer instability for systems containing PS₁₀-b-PMMA₅₀ or PS₂₀-b-PMMA₅₀; this behavior is in contrast to that observed when the same copolymer molecules are embedded in the top PS30 or PS50 matrices (refer to Fig 5.6a and 5.6b). The dewetting rates are reduced as the PS₁₀-b-PMMA₅₀ copolymer amount in PMMA243 is increased up to 4wt%. In conjunction with our experimental findings, one proposed explanation to the “expected” stability trends we observe when SM molecules are segregating from PMMA243 is that, as represented in Fig. 5.10, the micelles formed by SM molecules in the PMMA243 homopolymer matrix can migrate to the interface and break.

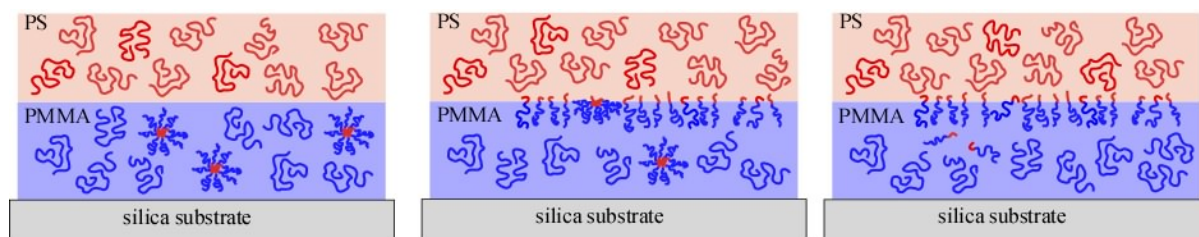


Figure 5.10 Representation of SM micelles segregating from PMMA243 and having sufficient time to break and adsorbed at the interface, thus, stabilizing the top PS layer.

5.5.3 Self-standing thin-films of (PS/SM) on Cu TEM grids

Self-standing films of both PS₅₀ and PS₅₀/PS₁₀-b-PMMA₅₀ copolymer (0.15 wt%) of 60nm thickness were prepared on Cu TEM grids (*ca.* Fig 5.11) and were used to explore film stability by annealing slightly above the T_g .

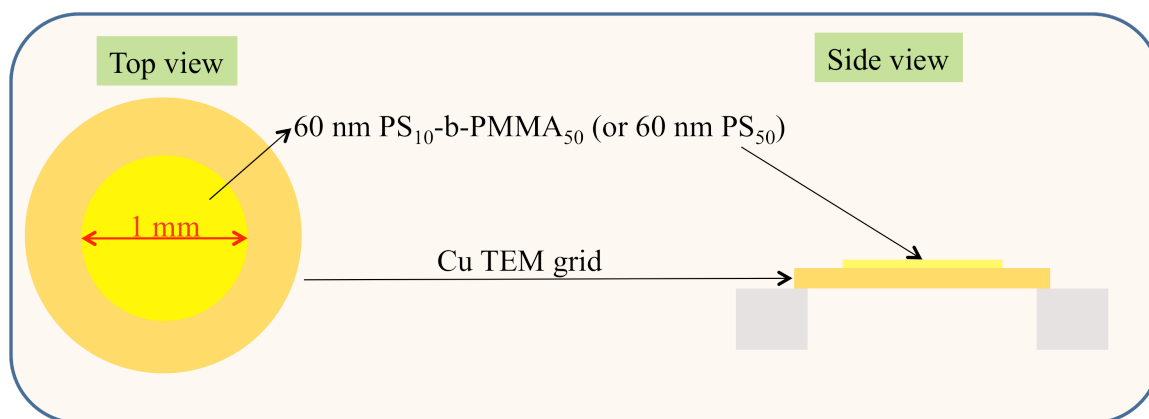


Figure 5.11 60nm-thick self-standing films of PS₅₀ and PS₅₀/PS₁₀-b-PMMA₅₀ (0.15 wt%) on Cu TEM grid with 1mm grid size. The grids are not touching the graphite plates; they are standing between two glass pieces on the corners. The middle hole where the film is located is freely standing, having an air/air interface on both sides.

The film stability was very sensitive to temperature; the films started rupturing around 120°C from side of the grid and it was completely torn before the temperature reached 160°C. Although temperature is a key parameter in micellization kinetics, since the purpose of the tests was to see which film (copolymer-added vs. copolymer-free) would dewet faster, annealing temperature was reduced from 180°C to 125°C to aid the observation of the film rupture process. PS50 films ruptured almost instantaneously when the temperature reached about 120°C. The SM copolymer-containing films were more stable but eventually failed. From this observation, it can be concluded that the destabilization of the PS with containing the PS₁₀-*b*-PMMA₅₀ copolymer is not due to the segregation to the free surface.

In order to test our hypothesis on surface heterogeneity due to crew-cut micelles, we have switched our interest from (PS/SM)/PMMA bilayer laminates to PS/SM/PMMA trilayer laminates where SM copolymer is spun-cast directly at the PS/PMMA interface.

5.5.4 PS/SM/PMMA and (PS/SM)/SM/PMMA trilayers on silicon substrates

In order to study the effect of the localization of the PS₁₀-*b*-PMMA₅₀ copolymer (PS30/PMMA243 interface vs. mixing with the PS30 top layer), we have deposited a thin layer of PMMA243 directly onto the silicon wafer and annealed this substrate above the T_g of PMMA243. The resultant film thickness was 54 nm, as measured by ellipsometry. By capitalizing on strong interaction between PMMA243 and silica, the purpose of those experiments was to immobilize some PMMA243 chains on the substrate. Any unbound PMMA243 was washed off the substrate with toluene. The final film thickness of the PMMA layer was 51 nm, as discerned by ellipsometry. Three SM copolymer (PS₁₀-*b*-PMMA₅₀, PS₁₀-

b-PMMA₅₀ and PS₅₀-*b*-PMMA₅₄) layer, thicknesses varied from 2.1 to 10 nm, were subsequently spin-coated on top of the substrate-bound PMMA₂₄₃ layer and the top layer was deposited via the floating method described earlier. The layer consisted of either pure PS₃₀ or a mixture of PS₃₀ and the PS₁₀-*b*-PMMA₅₀ copolymer (concentration 0.25 wt%). This procedure enabled us to control the amount of the PS₁₀-*b*-PMMA₅₀ copolymer at the interface. To discern if the PS₁₀-*b*-PMMA₅₀ copolymer is capable of stabilizing the PS/PMMA bilayer assembly, we have constructed a trilayer design wherein the copolymer is placed as a very thin middle layer directly at the PS/PMMA interface after the PMMA substrate is annealed and gently rinsed with toluene.

As documented by the data in Fig. 5.12, the dewetting rate of the PS layer can be reduced substantially if the SM midlayer thickness is at least ≈ 6 nm. This observation is consistent with the expectation that the copolymer, if located at the PS/PMMA interface, will serve to stabilize the top layer. This result is only achieved, however, when the midlayer is sufficiently thick, presumably to form a contiguous layer. According to Fig. 5.12, the dewetting rate of the top layer increases as the SM midlayer thickness decreases, confirming that a specific film thickness is required to ensure top film stabilization. At a thickness of ≈ 4 -5 nm, the dewetting rate is comparable to that of the copolymer-free PS (≈ 300 $\mu\text{m}/\text{h}$). Upon further reduction of the SM layer thickness, the dewetting rate exceeds that of neat PS, indicating that the SM layer is unable to remain coherent and breaks upon annealing. Another intriguing observation is that PS layer with and without copolymer exhibit almost identical dewetting kinetics, which confirms that only the copolymer at the interface regulates dewetting. Apparently there is sufficient amount of free SM micelles and free SM molecules

at the PS/PMMA interface, which seem to offset the instability induced by the crew-cut micelles present in the top PS30 layer.

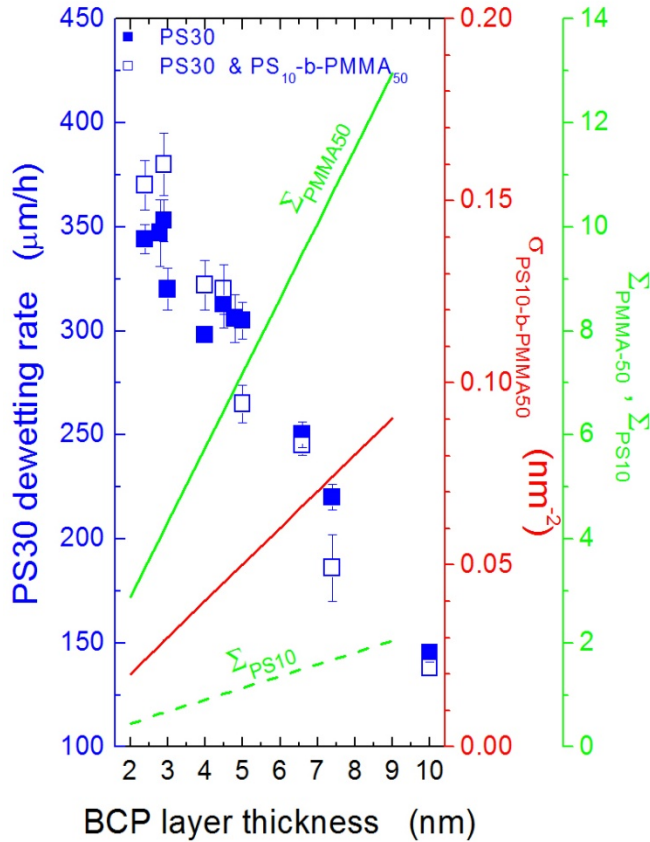


Figure 5.12 Linear dewetting rate of PS30/PS₁₀-*b*-PMMA₅₀ on PMMA243 at 180°C as a function of PS₁₀-*b*-PMMA₅₀ layer film thickness: (a) copolymer-free PS30 and (b) 0.25wt% copolymer-added PS30. Grafting densities are represented as a function of midlayer film thickness. Mushroom-to-brush crossover for the PS block is at $\Sigma_{PS10} = 1$.

At a midlayer thickness of ≈ 3.6 nm, the dewetting rate reaches a maximum, which compares favorably with data for the same copolymer at low concentrations in the bilayered assembly (*cf.* Fig. 12). Below this thickness, the dewetting rates decrease with decreasing

midlayer thickness. Optical micrographs of the dewetting trilayered systems reveal additional evidence of interfacial heterogeneity. At high SM layer thicknesses, circular holes develop as the PS layer dewets. At lower thicknesses, the rims of the dewetted holes become rough, and the shape of the holes deviates from circular. After removing the PS layer and scanning the area inside dewetted holes with AFM, the PS/PMMA interface shows evidence of roughening with a root-mean-square (RMS) roughness of 0.8 nm at ≈ 2 nm midlayer thickness (it is ≈ 0.4 nm for pure, annealed PMMA). As the SM layer thickness increases, the RMS roughness increases to 1.2 nm, but then abruptly drops to 0.5 nm when the midlayer is ≈ 7 nm thick. In this limit, the SM layer remains contiguous and stabilizes the top PS layer. In Fig. 5.12, the population of asymmetric PS₁₀-b-PMMA₅₀ molecules at the interface is so low that a contiguous midlayer is not achieved and the top layer is destabilized.

At large PS₁₀-b-PMMA₅₀ copolymer thicknesses, the dewetting kinetics of the PS₃₀ top layer can be reduced substantially increasing the stability of the top PS layer (*cf.* Fig. 5.12). The results are consistent with the neat PS₃₀/PMMA₂₄₃ system, proving that the modification of the PMMA₂₄₃ layer does not yield to unexpected dewetting behavior. The observed enhancement in the stability of the top PS₃₀ layer was solely due to the PS₁₀-b-PMMA₅₀ spun-cast directly at the PS₃₀/PMMA₂₄₃ interface.

Another indication of interfacial heterogeneity is the grafting density of the individual blocks of the copolymer molecules. Copolymer self-organization at the PS/PMMA interface, in terms of achieving stability, can be represented as the mushroom-to-brush crossover, at which the grafting density of the block forming the corona. In our calculations, grafting density of each block in the copolymer molecules is denoted as σ_{PS} or σ_{PMMA} , and total

grafting density of the block copolymer, denoted as Σ_{SM} . Grafting density (σ_{SM}) can be represented as

$$\boxed{\text{Diagram showing a red 'X' shape inside a rectangular box, representing a grafting density.}} \quad (1)$$

or in terms of d_{SM} (midlayer SM film thickness in nm), ρ_{SM} (density of the copolymer, assumed as 1 g/cm^3), N_A (the Avogadro's number) and the number-average molecular weight of the SM molecule (M_n):

$$\sigma_{SM} = \frac{N_A d_{SM} \rho_{SM}}{M_n} \quad (2)$$

Total grafting density of the block copolymer is given by

$$\boxed{\text{Diagram showing a red 'X' shape inside a rectangular box, representing a grafting density.}} \quad (3)$$

as a function of σ_{SM} , gyration radius of the corresponding block ($R_{g,block}$), represented as:

$$R_{g,block} = a\sqrt{N/6} \quad (4)$$

, a is the monomer size (0.74 nm for PMMA and 0.7 nm for PS) and “ N ” is the degree of polymerization of the corresponding block).

Top PS film stabilized upon reaching the mushroom-to-brush crossover, where grafting density of PS, Σ_{PS10} is equal to 1. This result is in agreement with our previous

findings from dewetting and OM studies which confirms that there is a certain thickness of the copolymer film at the interface required to stabilize the PS top layer. The crossover from the mushroom-to-brush regime occurs at ≈ 4 nm SM midlayer thickness, where we see a change in roughness, as well as the shape of the rims. This might indicate that micellar structures and aggregates are already formed in the film and they reside at the interface.

The other two systems we explored were the trilayer designs in which PS₅₀-b-PMMA₁₀ and PS₅₀-b-PMMA₅₄ were spun-cast directly at the interface as described earlier. According to our results shown in Fig. 5.13 and 5.14.

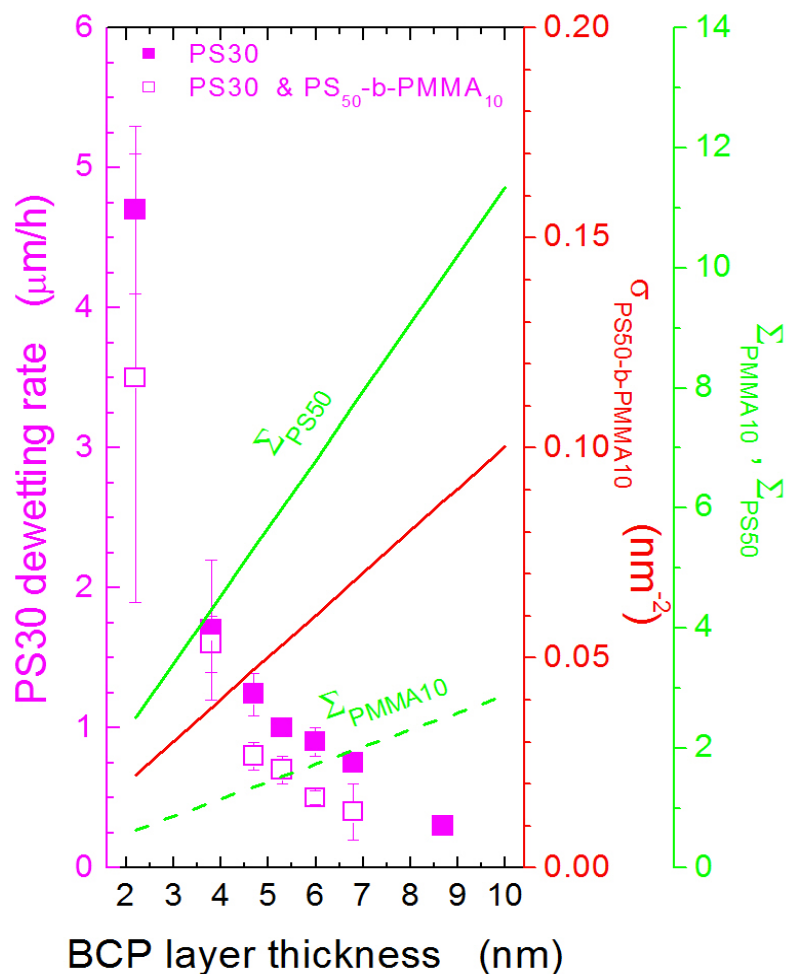


Figure 5.13 Linear dewetting rate of PS30/PS₅₀-*b*-PMMA₁₀ on PMMA243 at 180°C as a function of PS₅₀-*b*-PMMA₁₀ layer film thickness: (a) copolymer-free PS30 and (b) 0.25wt% copolymer-added PS30. Grafting densities are represented as a function of midlayer film thickness.

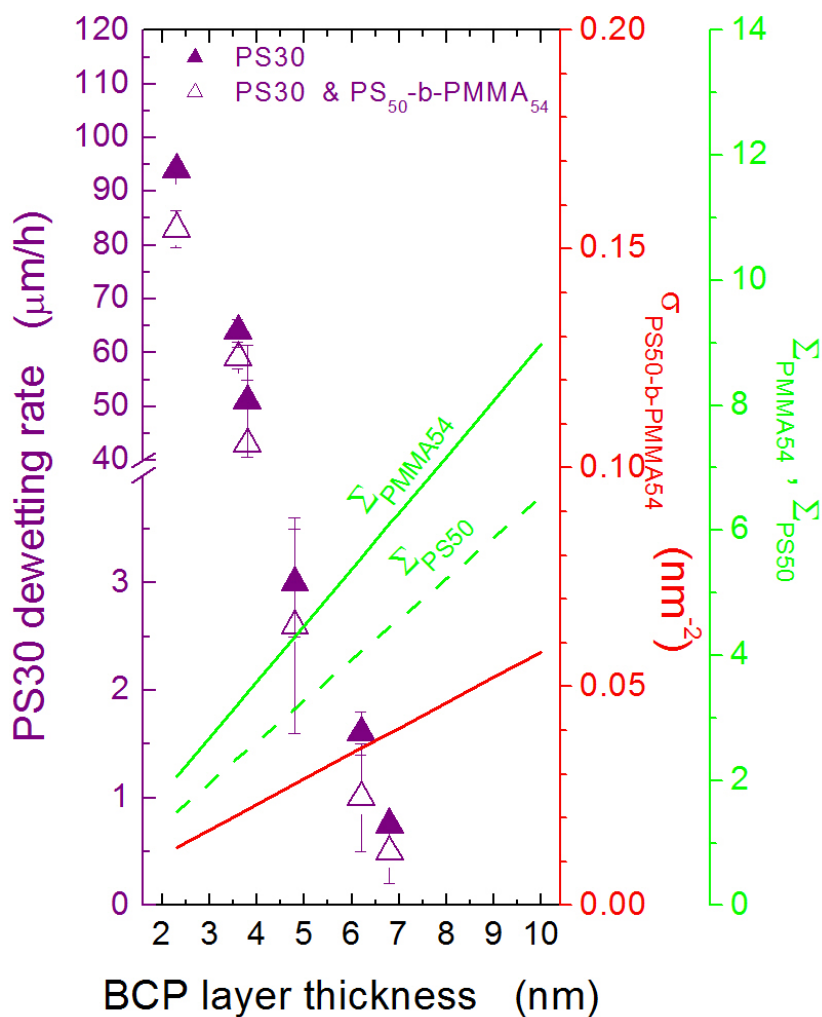


Figure 5.14 (Left) Linear dewetting rate of PS30/PS₅₀-*b*-PMMA₅₄ on PMMA243 at 180°C as a function of PS₅₀-*b*-PMMA₅₄ layer film thickness: (a) copolymer-free PS30 and (b) 0.25wt% copolymer-added PS30. Grafting densities are represented as a function of midlayer film thickness.

According to the dewetting kinetics, the asymmetric copolymer PS₅₀-*b*-PMMA₁₀ stabilizes the system more efficiently, even at low film thicknesses such as ≈2 nm. According to the grafting density values, its long PS block should switch from mushroom-to-brush confirmation, at ≈1nm; compared to that of PS₅₀-*b*-PMMA₅₄ copolymer, which is ≈1.5 nm.

Considering the gyration radius of the PS block, which is $\approx 5\text{-}6\text{nm}$ as a rough estimate, our understanding is insufficient to explain whether the interface has a contiguous layer of these copolymers, although the dewetting rate drops dramatically at $\approx 4\text{nm}$ of $\text{PS}_{50}\text{-}b\text{-PMMA}_{54}$ thickness where we see a change in the dewetting mechanism observed with *in situ* OM.

In order to develop a better understanding on the molecular-level of interfacial structuring, we have also calculated the CMC values for each block copolymer using the “dry-brush” theory developed by Leibler²⁵ and his coworkers (refer to Appendix 5.1). Although these calculations are independent of the matrix molecular weight, in which copolymer molecules embedded in, these rough estimates have, at least, given us valuable guidance with our overall experimental scheme. Our results agree with those obtained by SCFT modeling by Duque.²⁶ As expected, the copolymer with the lowest CMC value is the symmetric molecule, $\text{PS}_{50}\text{-}b\text{-PMMA}_{54}$. Other molecules with the same large PMMA block but with shorter PS blocks exhibit nearly the same CMC values. However, due to its highest molecular weight, which results in the highest incompatibility with the PS homopolymer, the symmetric copolymer molecules are entitled to a higher entropic penalty, thus, start forming micelles at very low concentration. The asymmetric copolymer molecules with the larger PMMA blocks, not start forming micelles at around the same low concentration, but also, they possess more free chains to incorporate into micelles due to its lower molecular weight.

According to our calculations, copolymer molecules with large PS short PMMA blocks have relatively high CMC values but in reality, these molecules might not even form micelles to induce lateral heterogeneities in given circumstances.

The next chapter brings another perspective to copolymer-mediated stabilization of immiscible polymer interfaces by employing block copolymer mixtures. Our results are concluded in such a way that will serve as a complimentary study for the SM-induced interface studies in Chapter 5.

References

1. Bates, F. S. & Fredrickson, G. H. Block Copolymer Thermodynamics: Theory and Experiment. *Annual Reviews in Physical Chemistry* **41**, 525-557 (1990).
2. Lodge, T. P. Block Copolymers: Past Successes and Future Challenges. *Macromolecular Chemistry and Physics* **204**, 265-273 (2003).
3. Wiltshire, J. T. & Qiao, G. G. Synthesis of core cross-linked star polymers with adjustable coronal properties. *Macromolecules* **41**, 623-631 (2008).
4. Cavallo, A.; Muller, M. & Binder, K. Monte Carlo simulation of a homopolymer-copolymer mixture interacting with a surface: Bulk versus surface micelles and brush formation. *Macromolecules* **41**, 4937-4944 (2008).
5. Klymko, T.; Subbotin, A. & ten Brinke, G. Distribution of homopolymer in lamellar self-assembled diblock copolymer/homopolymer blends involving specific interactions. *Macromolecules* **40**, 2863-2871 (2007).
6. Cavallo, A.; Muller, M.; Binder, K. Formation of micelles in homopolymer-copolymer mixtures: Quantitative comparison between simulations of long chains and self-consistent field calculations. *Macromolecules* **39**, 9539-9550 (2006).
7. Cheng, J. Y.; Mayes, A. M. & Ross, C. A. Nanostructure engineering by templated self-assembly of block copolymers. *Nature Materials* **3**, 823-828 (2004).
8. Hamley, I. W. Nanostructure fabrication using block copolymers. *Nanotechnology* **14**, 39-39 (2003).
9. Krishnan, R. S.; Mackay, M. E.; Duxbury, P. M.; Hawker, C. J.; Asokan, S.; Wong, M. S.; Goyette, R. & Thiyagarajan, P. Improved polymer thin-film wetting behavior through nanoparticle segregation to interfaces. *Journal of Physics, Condensed Matter* **19**, 356003-356003 (2007).
10. de Silva, J. P.; Geoghegan, M.; Higgins, A. M.; Krausch, G.; David, M. O.; Reiter, G. Switching layer stability in a polymer bilayer by thickness variation. *Physical Review Letters* **98** (2007).
11. Segalman, R. A. Patterning with block copolymer thin films. *Materials Science & Engineering R* **48**, 191-226 (2005).

12. Kim, S. H.; Misner, M. J. & Russell, T. P. Solvent-induced ordering in thin film diblock copolymer/homopolymer mixtures. *Advanced Materials* **16**, 2119-+-2119-+ (2004).
13. Zhang, Z.; Wang, Z.; Xing, R. & Han, Y. Patterning thin polymer films by surface-directed dewetting and pattern transfer. *Polymer* **44**, 3737-3743 (2003).
14. Goldraich, M.; Talmon, Y.; Alexandridis, P.; Lindman, B. *Amphiphilic block copolymers: self assembly and applications* (Elsevier, Amsterdam, 2000).
15. Matsen, M. W. Stabilizing New Morphologies by Blending Homopolymer with Block Copolymer. *Physical Review Letters* **74**, 4225-4228 (1995).
16. Shull, K. R. Mean-field theory of block copolymers: bulk melts, surfaces, and thin films. *Macromolecules* **25**, 2122-2133 (1992).
17. Mayes, A. M.; Russell, T. P.; Satija, S. K. & Majkrzak, C. F. Homopolymer distributions in ordered block copolymers. *Macromolecules* **25**, 6523-6531 (1992).
18. Whitmore, M. D. & Noolandi, J. Theory Of Micelle Formation In Block Copolymer Homopolymer Blends. *Macromolecules* **18**, 657-665 (1985).
19. Whitmore, M. D. & Noolandi, J. Theory of micelle formation in block copolymer-homopolymer blends. *Macromolecules* **18**, 657-665 (1985).
20. Wei, B. in *Chemical & Biomolecular Engineering* (NC State Univ., 2005).
21. Wei, B.; Lam, P.G.; Braunfeld, M.; Agard, D.A.; Genzer, J; Spontak, R.J. Tunable Instability Mechanisms of Polymer Thin Films by Molecular Self-Assembly. *Langmuir* **22**, 8642-8645 (2006).
22. Zhao, C.L.; Winnik, M.A.; Riess, G.; Croucher, M.D.. Fluorescence Probe Techniques Used To Study Micelle Formation In Water-Soluble Block Copolymers. *Langmuir* **6**, 514-516 (1990).
23. Hu, W.; Koberstein, J.T.; Lingelser, J.P.; Gallot, Y. Interfacial Tension Reduction in Polystyrene/ Poly(dimethylsiloxane) Blends by the Addition of Poly(styrene-b-dimethylsiloxane). *Macromolecules* **28**, 5209-5214 (1995).
24. Leibler, L. Block Copolymers At Interfaces. *Physica A* **172**, 258-268 (1991).

25. Leibler, Ludwik;Orland, Henri & Wheeler, John C. Theory of critical micelle concentration for solutions of block copolymers. *The Journal of Chemical Physics* **79**, 3550-3557 (1983).
26. Duque, D. Theory of copolymer micellization. *Journal Of Chemical Physics* **119**, 5701-5704 (2003).
27. Esselink, F.J.; Dormidontova, E.; Hadziioannou, G. Evolution of block copolymer micellar size and structure evidenced with cryo electron microscopy. *Macromolecules* **31**, 2925 (1998).
28. Lam, Y.M.; Grigorieff, N.; Goldbeck-Wood, G. Direct visualisation of micelles of Pluronic block copolymers in aqueous solution by cryo-TEM. *Physical Chemistry Chemical Physics* **1**, 3331-3334 (1999).
29. Cheng, D.; SC, Ng; Chan, H.S.O. Morphology of polyaniline nanoparticles synthesized in triblock copolymers micelles. *Thin Solid Films* **477**, 19-23 (2005).
30. Calderara, F.; Hruska, Z.; Hurtrez, G.; Lerch, J.P.; Nugay, T.; Riess, G. Investigation Of Polystyrene-Poly(Ethylene Oxide) Block-Copolymer Micelle Formation In Organic And Aqueous-Solutions By Nonradiative Energy-Transfer Experiments. *Macromolecules* **27**, 1210-1215 (1994).
31. Calderara, F. (University Upper Alsace, France, 1995).
32. Castelletto, V.; Caillet, C.; Hamley, I.W. Liquid-Solid Transition in a Model Hard Sphere System of Block Copolymer Micelles. *Physical Review E* **65**, 050601 (2002).
33. Castelletto, V.; Hamley, I.W., Pedersen, J.S. A Small Angle Neutron Scattering Investigation of the Structure of Highly Swollen Block Copolymer Micelles. *J. Chem. Phys.* **117**, 8124-8129 (2002).
34. Connell, S.D.; Collins, S.; Fundin, J.; Yang, Z., Hamley, I.W. In Situ Atomic Force Microscopy Imaging of Block Copolymer Micelles Adsorbed on a Solid Substrate. *Langmuir* **19**, 10449-10453 (2003).
35. Spontak, R.J.; Patel, N.P. in *Developments in Block Copolymer Science and Technology* (John Wiley & Sons, 2004).
36. Zhulina, E.B.; Birshstein, T.M. E.B. Zhulina and T.M. Birstein, *Vysokomol. Soedin.*, Ser. A **27**, 511 (1985). *Vysokomol. Soedin., Ser. A* **27**, 511 (1985).

37. Halperin, A. Starlike Micelles - Their Growth In Homopolymer Solutions. *Macromolecules* **22**, 3806-3807 (1989).
38. Nagarajan, R.; Ganesh, K. Block Copolymer Self-Assembly In Selective Solvents - Theory Of Solubilization In Spherical Micelles. *Macromolecules* **22**, 4312-4325 (1989).
39. Moffitt, M.; Khougaz, K.; Eisenberg, A. Micellization of ionic block copolymers. *Accounts of Chemical Research* **29**, 95-102 (1996).
40. Russell, T.P.; Hjelm Jr., R.P.; Seeger, P.A. Temperature Dependence of the Interaction Parameter of Polystyrene and Poly(methy methacrylate). *Macromolecules* **23**, 890 (1990).

Appendix

Appendix A. CMC values via dry-brush theory

Self-organization of block copolymer molecules at immiscible interfaces can reduce the interfacial tension. When copolymers are added into a system, the entropy of mixing of the copolymer with the homopolymer favors a random distribution of these self-assembly molecules in the bulk. However, the unfavorable interaction of the block segments of different species tend to drive the copolymer toward the interface, resulting in a reduction in interfacial tension, thus, acting as an emulsifier at the interface. The reduction in interfacial tension is directly related to the formation and the number of copolymer micelles in the system. When the copolymer concentration exceeds a critical concentration called “critical micelle concentration” (CMC), copolymer molecules reside in micellar phase and exist as free chains. Formation of micelles and aggregates limit the migration of copolymer molecules to the interface, thus, the interfacial tension becomes independent of copolymer concentration above CMC.

We have based our CMC calculations on the dry-brush theory,²³⁻²⁴ which was developed by one of the pioneering investigators of micellization in block copolymers. According to this theory, block copolymer corona cannot be penetrated by large homopolymer chains. The resultant CMC values, which are independent of the homopolymer matrix molecular weight, are given by

$$\Phi_{\text{CMC}} = \exp(\mu_{\text{CMC}} / kT - \chi N_A) \quad (\text{A5.1})$$

where A denotes the shorter sequence and the chemical potential at the CMC (Φ_{CMC}) is defined as

$$\mu_{\text{CMC}}/kT = (1.5)^{4/3} * f^{4/9} * (1.74 * f^{1/3} - 1)^{1/3} * (\chi N)^{1/3} \quad (\text{A5.2})$$

where f is the symmetry factor which is the ratio of number of the monomers of the short block to the total number of monomer units in the system (N_A/N), k is the Boltzmann constant, T is the absolute temperature (K) and χ is the thermodynamic incompatibility parameter, and for a PS/PMMA binary system, defined as⁴⁰

$$\chi_{\text{PS-b-PMMA}}: (0.028 \pm 0.002) + (3.9 \pm 0.6) / T \text{ (K)} \quad (\text{A5.3})$$

In our calculations, PMMA block is denoted as A and PS block as B. The temperature value used is 453.15K. According to our calculations, CMC decreases with increasing incompatibility and with increasing molecular weights of the copolymer and homopolymers, which is in agreement with the theoretical studies (*cf.* Table A5.1).

Table A5.1 CMC values via dry-brush theory²³⁻²⁴

SM copolymer	N_A	N_B	N (N_A + N_B)	f_A	μ/kT	χ^lN_A	μ/kT- χ^lN_A	CMC = exp (μ/kT-χ^lN_A)
PS₅₀-<i>b</i>-PMMA₅₄	480.3	473.1	953.4	0.496	4.4	18.1	-13.7	1.15x10⁻⁶
PS₅₀-<i>b</i>-PMMA₂₀	485.1	183.1	668.2	0.274	3.4	7.0	-3.6	2.66 x10⁻²
PS₅₀-<i>b</i>-PMMA₁₀	485.1	87.6	572.7	0.153	2.7	3.4	-0.6	5.39 x10⁻¹
PS₂₀-<i>b</i>-PMMA₅₀	194.0	442.4	636.5	0.695	4.2	16.9	-12.7	2.91 x10⁻⁶
PS₁₀-<i>b</i>-PMMA₅₀	89.3	446.8	536.2	0.833	4.1	17.1	-13.0	2.27 x10⁻⁶

Appendix B. CMC values via self-consistent field theory (SCFT)

According to the theory developed by Duque,²⁶ an incompressible mixture of copolymers and homopolymers are examined in a SCFT using a standard Gaussian model. For the case of copolymers in solution, where the micelle concentration is low, each micelle is treated as isolated.

For simplicity, micelle translational entropy is ignored in the calculations. SCFT was used to calculate the excess free energy of an isolated micelle for different bulk copolymer concentrations (or equivalently, the chemical potential of the copolymers in the bulk). The CMC value is obtained when the excess free energy becomes zero.²⁶

Table A5.2 CMC values via self-consistent field theory

SM copolymer	CMC in PS30	CMC in PS50
PS ₅₀ - <i>b</i> -PMMA ₅₄	2.50E-05	2.20E-06
PS ₅₀ - <i>b</i> -PMMA ₂₀	3.50E-02	1.60E-02
PS ₅₀ - <i>b</i> -PMMA ₁₀	N/A	N/A
PS ₂₀ - <i>b</i> -PMMA ₅₀	7.90E-06	7.60E-07
PS ₁₀ - <i>b</i> -PMMA ₅₀	3.50E-06	5.00E-06

In the simulations, the excess free energy for PS₅₀-*b*-PMMA₁₀ is always positive, so the CMC value could not be calculated.

Appendix C. Interfacial tension vs. diblock asymmetry and concentration in PS/SM/PMMA bilayers via Self-Consistent Field Theory

In this Appendix, interfacial tension in PS/SM copolymer/PMMA blends is calculated via self-consistent field theory. The blends are treated as 1D system and PS/PMMA interface is fixed at $z = 0$. The blends reach PMMA bulk state as $z \rightarrow -\infty$, and reach PS bulk state as $z \rightarrow +\infty$. Homopolymer PS, homopolymer PMMA and SM copolymer are denoted as A, B and AB, respectively. With these calculations, we intend to address questions such as (i) how interfacial tension varies as different copolymer molecules are added, and (ii) how the copolymer molecules distribute within the blends.

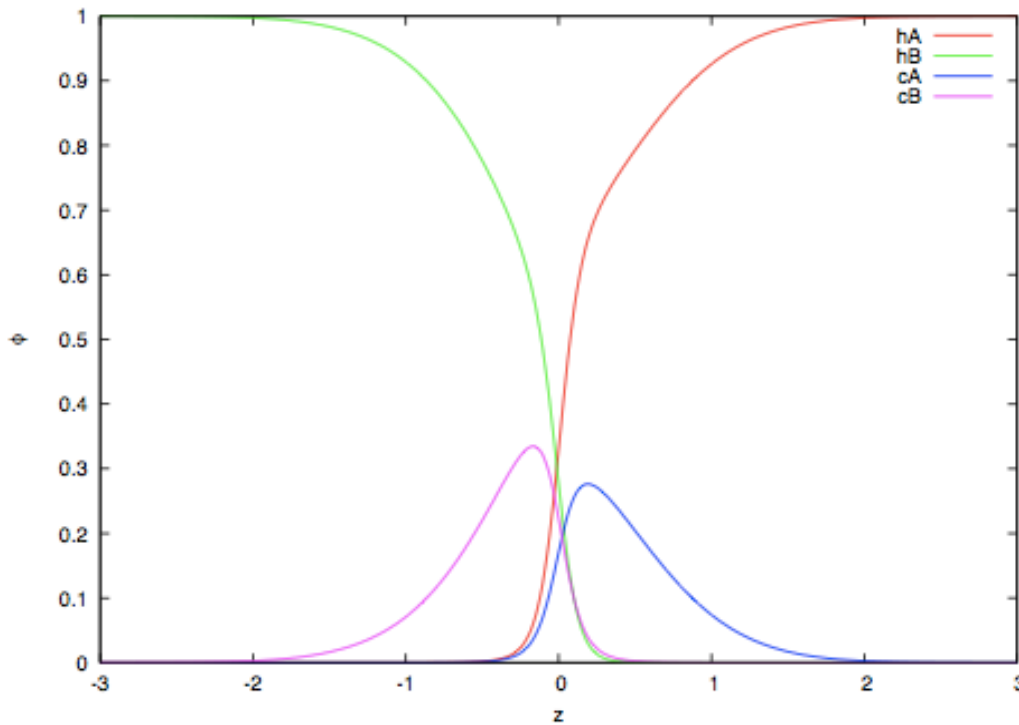


Figure A5.1 Typical density profile for PS₃₀/PS₅₀-b-PMMA₅₄/PMMA₂₄₃

According to the results, the symmetric copolymer molecules mostly reside at the interface; on the other hand, the asymmetric blocks mostly remain in the bulk state. These results are not in completely in agreement with our experimental studies, however, we want to emphasize that all these calculations are in equilibrium, thereby the calculations are independent from the matrix homopolymer in which the copolymer molecules added, however, the initial position of the diblock copolymers should have effect on dynamics.

Chapter 6: Mixtures of asymmetric block copolymers at immiscible PS/PMMA interfaces

6.1 Motivation

Our previous studies have established that self-organization of asymmetric copolymer molecules changes substantially the properties of an immiscible polystyrene/poly(methyl methacrylate) (PS/PMMA or SM) laminate by modifying the interfacial properties due to adsorption and lateral structuring. Block compositional asymmetry as well as other parameters, such as copolymer concentration and geometry, in which copolymer self-assembly is confined, have demonstrated profound effect on lateral structuring at interfaces. Before introducing a new concept in designing novel means of compatibilization, which helps us develop a molecular-level understanding of partitioning of block copolymers at the interface between two immiscible homopolymers, it is be useful to summarize the results of how block copolymer compositional asymmetry and concentration affect an immiscible PS₅₀/PMMA₂₄₃ interface (*cf.* Fig. 6.1).

Consider a bilayer system comprising PS/PMMA sandwich placed on top of a flat substrate with the PMMA layer being in contact with the substrate and PS film being exposed to the surface. A symmetric PS₅₀-*b*-PMMA₅₄ copolymer used at relatively high copolymer concentrations (>10 wt% copolymer) stabilizes the PS/PMMA bilayer. Reducing the concentration of the SM copolymer leads to destabilization of the top PS layer. The trends in the behavior are obvious. The highest dewetting rate occurs for most systems when no SM copolymer is added to the interface. Increasing the concentration of the SM copolymer improves the stability of the system and reduces the dewetting rate of the top PS

film. If the size of the PS block is held constant and the size of the PMMA block is varied which reflects changes in incompatibility between the copolymer and PS matrix and, thus, the driving force for copolymer self-assembly, several important trends are observed.

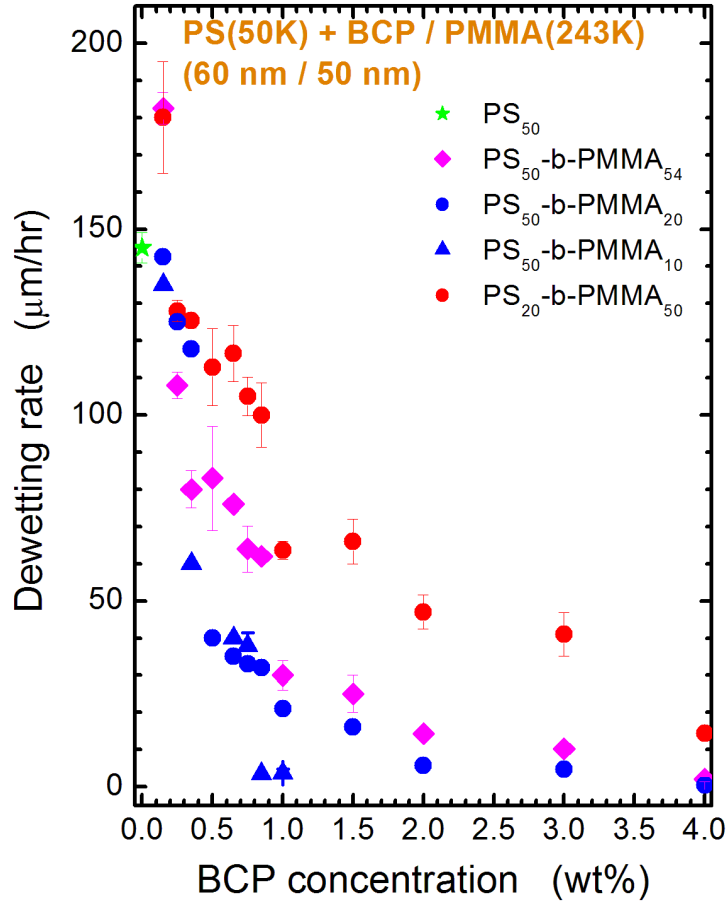


Figure 6.1 Linear dewetting rates of PS50/SM on PMMA243 at 180°C as a function of SM copolymer concentration. One symmetric and three asymmetric copolymers are embedded in PS.

A reduction in PMMA block size of the copolymer molecules enhances stabilization of the top PS50 layer as the dewetting rate decreases. Reduced driving force for

micellization indicates that the copolymer molecules can migrate effectively to the PS₅₀/PMMA₂₄₃ (numbers denote the molecular weight in kg/mol) interface and cause stabilization. Note that the PS₅₀-*b*-PMMA₁₀ copolymer with the shortest PMMA block stabilizes the assembly at < 1 wt% copolymer. In addition, a sharp drop in dewetting rate remains evident from ≈0.8-1.0 wt% copolymer concentration.

In a reverse fashion, when the PS block is shortened, thus, the driving force for micellization is increased, the dewetting rate is observed to increase. The same precipitous drop noted earlier remains apparent. Taken together, our results exhibit that copolymer molecules with relatively short PMMA blocks segregate more readily from the PS matrix and locate along the PS/PMMA interface where the short PMMA blocks can mix with the bottom PMMA substrate.

From our asymmetric block copolymer studies it is clear that there is an interplay between micellization and stabilization for the self-organization of these molecules at the PS/PMMA interface; this trend is highly dependent on the incompatibility between the blocks (hence, between the copolymer molecules and the surrounding media) and on copolymer concentration. These observations have led to new studies that aimed at exploring lateral structuring of PS/PMMA assemblies containing mixtures of copolymers with complementary asymmetric composition, such as (PS₅₀-*b*-PMMA₁₀ / PS₁₀-*b*-PMMA₅₀) and (PS₅₀-*b*-PMMA₂₀ / PS₂₀-*b*-PMMA₅₀). With these systems, we will be addressing questions such as: (1) is there a competition between copolymer micelles and free copolymer chains? (2) What does the interface look like at low and high copolymer concentrations? (3) How does the interfacial arrangement of the copolymer at the interface change as a function of

time and copolymer concentration? (4) What is the reason behind the stability effect seen by ‘large PS-short PMMA block’ copolymers (PS₅₀-*b*-PMMA₁₀ and PS₅₀-*b*-PMMA₂₀) at low concentration values, ≈ 0.5 -1.0 wt%?

6.2 Experimental

6.2.1 Materials

PS homopolymer, designated as PS50 (the suffix denotes the number-average molecular weight, M_n , in kg/mol and polydispersity index, M_w/M_n is 1.06) was purchased from Pressure Chemical, Inc. PMMA (PMMA243, numerical designation denotes the molecular weight in kg/mol) homopolymer and polydispersity index, M_w/M_n is 1.06) was purchased from Polymer Source Co. Four asymmetric PS-*b*-PMMA (SM) copolymers (S₅₀-M₂₀, S₂₀-M₅₀, S₅₀-M₁₀ and S₁₀-M₅₀, where the subscripted numerical designation denotes the block weight in kg/mol) were obtained from Polymer Source, Inc. All polymeric materials were used as-received. Solvent-grade toluene was purchased from Sigma Aldrich and used as-received for solution preparation purposes.

6.2.2 Methods

Solutions consisting of 1.35 wt% PMMA243 in toluene were prepared, and thin polymer films were spun-cast onto silicon wafer with a Headway spin-coater at 2000 rpm for 30 s. These conditions were crucial to ensure a constant film thickness of 50 nm for the PMMA243/SM layer, as discerned by ellipsometry, to permit systematic and quantitative

comparison. In addition, solutions composed of 1.55 wt% PS50 with mirrored copolymer pairs of (PS₅₀-*b*-PMMA₁₀ / PS₁₀-*b*-PMMA₅₀) and (PS₅₀-*b*-PMMA₂₀ / PS₂₀-*b*-PMMA₅₀) in toluene were prepared and likewise spun-cast onto glass slides under similar conditions. The mass fraction of SM copolymer mixtures in the PS50 layer ranged from 0 (pure PS50) to 0.04. Equimass mixtures (compositionally equal) of (PS₅₀-*b*-PMMA₂₀ / PS₂₀-*b*-PMMA₅₀) were employed for each desired copolymer concentration. For the mixtures of (PS₅₀-*b*-PMMA₁₀ / PS₁₀-*b*-PMMA₅₀) copolymer pair, the composition of PS₁₀-*b*-PMMA₅₀ was varied from 50 wt% (yielding an equimass) to 99 wt% (in PS₁₀-*b*-PMMA₅₀). The composition of the PS₅₀-*b*-PMMA₁₀ copolymer was varied accordingly. Dried PS50/SM mixture films measuring 60 nm could be easily floated off on water and deposited directly on the PMMA substrate to form a bilayer film.

After drying the bilayers in air at room temperature for 24 h, the samples were annealed individually at 180°C, above the glass transition temperature (T_g) of both PS ($\approx 100^\circ\text{C}$) and PMMA ($\approx 120^\circ\text{C}$), under a circulating N₂ flow (to avoid oxidative degradation) for pre-designated time intervals. Dewetting kinetics of the top PS layer was monitored at various temperatures *in situ* with an Olympus BX60 optical microscope equipped with a computer-interfaced CCD camera and operated in reflection mode.

6.3 Results and Discussion

6.3.1 Equimass mixtures of PS_{50} - b - $PMMA_{20}$ / PS_{20} - b - $PMMA_{50}$

Measured dewetting rates are presented in Fig. 6.2; they reveal that the dewetting rates of systems composed of compositionally equal copolymer mixtures of PS_{50} - b - $PMMA_{20}$ / PS_{20} - b - $PMMA_{50}$ lie between those of systems modified with the neat copolymers. This observation suggests strongly that, under at least some experimental conditions, the dewetting behavior of the double layer with a copolymer mixture may be satisfactorily approximated by a linear rule of mixtures. In addition, a sharp drop in dewetting rate remains evident from ≈ 0.75 - 1.0 wt% copolymer concentration.

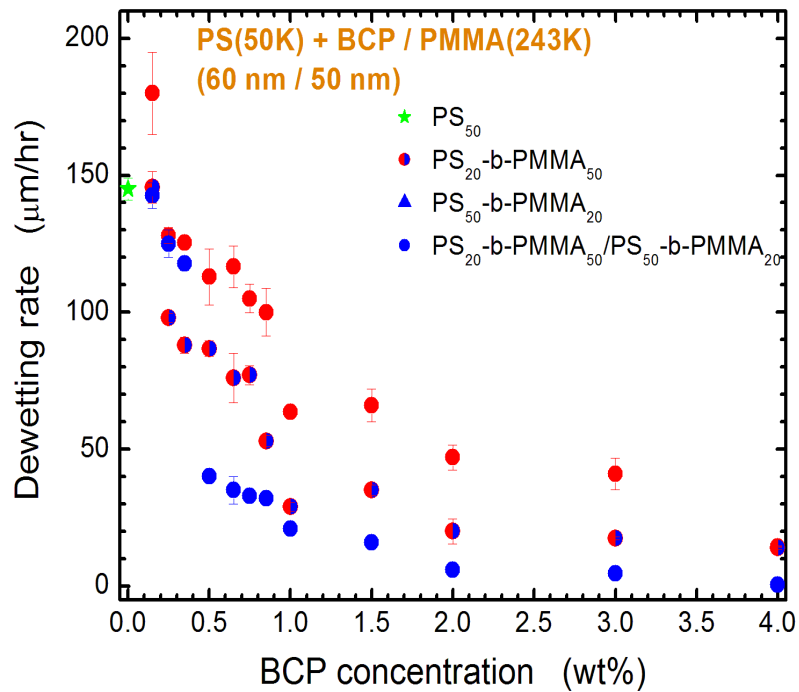


Figure 6.2 Linear dewetting rate for PS_{50} containing equimass PS_{20} - b - $PMMA_{50}$ and PS_{50} - b - $PMMA_{20}$ mixtures on $PMMA_{243}$ at 180°C as a function of copolymer concentration.

At relatively higher compositions (> 1 wt%), the dewetting kinetics is governed by the copolymer with large-PS short-PMMA blocks, $PS_{50}-b-PMMA_{20}$. This can be related to the ability of free $PS_{50}-b-PMMA_{20}$ chains to migrate to the interface faster than the $PS_{20}-b-PMMA_{50}$ micelles thus pinning the top PS layer down. This phenomenon takes over $\approx 0.75 - 1.0$ wt%. Intriguingly, there is a jump in dewetting rates at very low concentrations (0.15 - 0.35 wt%) of copolymers with large-PMMA blocks (i.e., $PS_{10}-b-PMMA_{50}$, $PS_{20}-b-PMMA_{50}$ and $PS_{50}-b-PMMA_{54}$). When there is a sufficient amount of free copolymers chains in the system, not only are they capable of migrating faster to and occupying the interface and adsorbed on corresponding phases. At very low concentrations mentioned above, majority of SM copolymer molecules reside in copolymer micelles and these micelles do not break as quickly as the top PS layer dewets, resulting in exhibiting higher dewetting rates than that of copolymer-free top PS layer.

In order to investigate the effect of micellization on interfacial stability, we direct our attention to an even more fascinating pair study, mixtures of ($PS_{50}-b-PMMA_{10} / PS_{10}-b-PMMA_{50}$). Top PS layer with $PS_{50}-b-PMMA_{10}$ copolymer is the most stable system. However, $PS_{10}-b-PMMA_{50}$ is proven to destabilize the interface due to its tendency to form micelles. Incorporation of the mixture of these two copolymer molecules in the top PS layer will give us a better insight into the effect of block asymmetry at polymer/polymer interfaces.

6.3.2 Mixtures of $PS_{50}\text{-}b\text{-}PMMA_{10}$ / $PS_{10}\text{-}b\text{-}PMMA_{50}$

We opt to use the $PS_{10}\text{-}b\text{-}PMMA_{50}$ copolymer composition as the leading independent variable and show that $PS_{10}\text{-}b\text{-}PMMA_{50}$ / $PS_{50}\text{-}b\text{-}PMMA_{10}$ mixtures follow the aforementioned scaling behavior for the dewetting rate for all compositions up to 97wt% $PS_{10}\text{-}b\text{-}PMMA_{50}$. In mixtures having $PS_{10}\text{-}b\text{-}PMMA_{50}$ in compositions higher than 97wt% the dewetting rate becomes nearly independent of the $PS_{10}\text{-}b\text{-}PMMA_{50}$ copolymer concentration, approaching the dewetting rates of the individual $PS_{10}\text{-}b\text{-}PMMA_{50}$ copolymer series. The stabilization effect of $PS_{50}\text{-}b\text{-}PMMA_{10}$ can be observed at 2wt% in composition at copolymer mixture concentrations of 1wt% or higher.

As the composition of the $PS_{50}\text{-}b\text{-}PMMA_{10}$ / $PS_{10}\text{-}b\text{-}PMMA_{50}$ mixtures is varied gradually, individual dewetting trends shown in Fig. 6.3 can be represented in a master curve (*cf.* Fig. 6.4) as a function of the $PS_{50}\text{-}b\text{-}PMMA_{10}$ copolymer concentration. As the composition of the $PS_{10}\text{-}b\text{-}PMMA_{50}$ copolymer, which has a tendency to form micelles faster due to its large PMMA block, is increased up to 97wt% of the dewetting rates becomes almost independent of the $PS_{10}\text{-}b\text{-}PMMA_{50}$ copolymer concentration, approaching the dewetting rates of the individual copolymer series. The stabilization effect can be observed when the composition of $PS_{50}\text{-}b\text{-}PMMA_{10}$ is ≈ 2 wt% in the mixture and at copolymer mixture concentrations of 1wt% or higher.

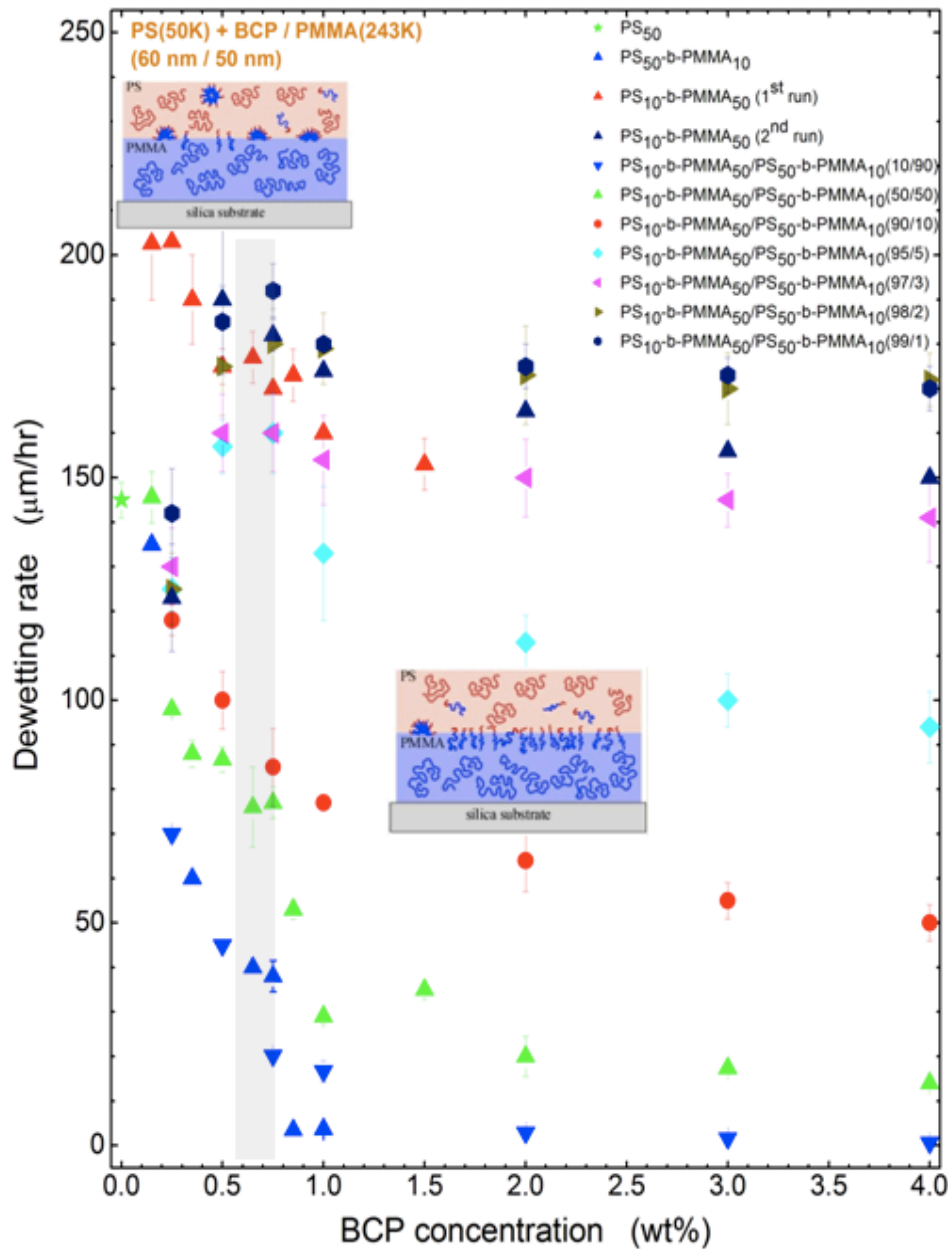


Figure 6.3 Linear dewetting rate for PS_{50} containing $\text{PS}_{10}\text{-}b\text{-PMMA}_{50}$ and $\text{PS}_{50}\text{-}b\text{-PMMA}_{10}$ mixtures on PMMA_{243} at 180°C as a function of copolymer concentration. The composition of $\text{PS}_{10}\text{-}b\text{-PMMA}_{50}$ was varied from 50wt% (yielding an equimass mixture, 50/50) to 99wt% (99/1). The composition of the $\text{PS}_{50}\text{-}b\text{-PMMA}_{10}$ copolymer was varied accordingly. The grey bar represents the concentration regime, beyond which the stability is governed by $\text{PS}_{50}\text{-}b\text{-PMMA}_{10}$. The cartoon on the top left is an illustration of $\text{PS}_{10}\text{-}b\text{-PMMA}_{50}$ micelles at the interface, and the one on the bottom right side represents the stability induced by $\text{PS}_{50}\text{-}b\text{-PMMA}_{10}$ chains.

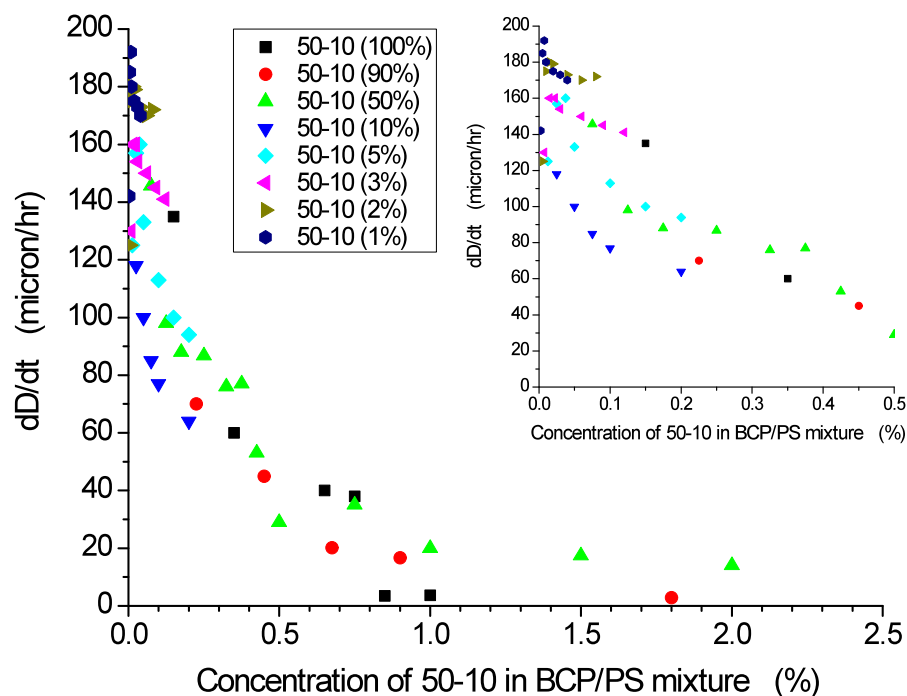


Figure 6.4 Linear dewetting rate for PS_{10} - b - $PMMA_{50}$ and PS_{50} - b - $PMMA_{10}$ mixtures containing PS_{50} on $PMMA_{243}$ at $180^{\circ}C$ as a function of PS_{50} - b - $PMMA_{10}$ copolymer concentration. PS_{50} - b - $PMMA_{10}$ copolymer is denoted as 50-10 (w%) for simplicity and “w” represents the weight composition of this copolymer in the mixture.

As our previous results demonstrated such structuring can be highly heterogeneous and in thin-film geometries, such interfacial heterogeneities, may adversely affect the stability. Structure variations of copolymer molecules along the interface provide experimental evidence of lateral interfacial structuring. In this study, we explored the copolymer mixtures consisted of two mirrored asymmetric copolymers, PS_{20} - b - $PMMA_{50}$ / PS_{50} - b - $PMMA_{20}$ and

PS₁₀-*b*-PMMA₅₀ / PS₅₀-*b*-PMMA₁₀. We have addressed questions such as (i) how the interface evolve in terms of copolymer-driven lateral structuring at different copolymer concentrations, and (ii) what molecular and environmental factors cause either interfacial structuring or copolymer self-assembly to dominate. The interplay between stabilization at the interface and interfacial heterogeneity formation can be clearly seen when equimass mixtures of mirrored copolymers are added in the top film. As demonstrated in our copolymer studies, the copolymer molecules with short PS block and large PMMA block forms micelles and aggregates almost instantaneously upon spin-casting, on the other hand, the molecules with large PS block and short PMMA block mostly remain as free chains. The competition between these two molecules also reflects on the dewetting trends. As the copolymer concentration increases, we see the stabilization in the top PS film and this behavior almost follows a rule of mixtures, wherein the data lies between the individual dewetting trends of the each copolymer-added system. As one copolymer composition (PS₁₀-*b*-PMMA₅₀) is gradually varied in the copolymer mixture, this competition becomes more apparent. At low concentrations, the interfacial heterogeneities formed by this copolymer become more dominant at low mixture concentrations as the amount of this copolymer is increased. More micelles are present compared to the free SM copolymer chains and the PS layer dewets faster than the aggregates migrating to the interface and breaking. As the concentration of PS₅₀-*b*-PMMA₁₀ in the copolymer mixture increases, we observe an increase in stability ≈ 0.5 - 1.0 , another similar stabilization behavior that exhibited in bilayers, in which this copolymer was incorporated. As the composition of the (PS₁₀-*b*-PMMA₅₀) is further increased, it almost converges to the dewetting trend as if only (PS₁₀-*b*-PMMA₅₀) copolymer

was added in the top PS layer, as expected. As shown in Fig. 6.4, this composition-dependent study can be represented as a function of (PS₅₀-b-PMMA₁₀) copolymer.

CHAPTER 7 Conclusions and Recommendations for Future Work

7.1 General remarks

In this PhD dissertation, we have investigated the parameters such as copolymer/nanoparticle concentration, architecture and molecular weight combined with film thickness, time and temperature in order to develop a molecular-level insight on how lateral interfacial structuring occurs at immiscible polymer/polymer interfaces.

In order to develop a molecular-level understanding of how these ‘smart’ self-assembling materials and grafted nanoparticles interact both intra- and inter-molecularly and form ordered structures in bulk, as well as at immiscible interfaces, we first focused on the response of core-shell polymer nanoparticles, designated CSNGs, composed of a cross-linked divinylbenzene core and poly(methyl methacrylate) (PMMA) arms as they segregate from PMMA homopolymer. Our previous study with these nanoparticles has established the arms exhibit autophobic character when dispersed in high molecular weight homopolymer matrices and segregate to the interface with another fluid. These were bilayer systems comprising thin films of polystyrene (PS) placed directly on top of PMMA/microgel substrates. These PS/PMMA laminates above the glass transition temperature ($T_g \approx 100^\circ\text{C}$) for up to 12 hours under continuous N_2 flow demonstrated that these PMMA-arm particles not only migrate to the PS/PMMA interface but also form elaborate aggregate structures, i.e., chains, revealed by sequence AFM images acquired from where the top PS layer dewetted. In some cases (e.g., at the 6 and 9 h anneal times) near the PS island boundary, some of the particles faded into the PMMA matrix, thus supporting our earlier observations that the

particles can be forced back into the matrix upon post-annealing upon switching from a relatively low interfacial energy ($\approx 2 \text{ mJ/m}^2$) to surface energy ($\approx 30 \text{ mJ/m}^2$), which tends to keep the surface of the dewetted PMMA substrate flat. For cross-sectional transmission electron microscopy (TEM) imaging of the PS/PMMA/CSNGs bilayers, a new core-shell polymer nanoparticle has been synthesized with an acrylic core derived from ethylene glycol dimethacrylate (EGDMA) and PS arms and designated as CSNG-R (“R” denoting “reverse” in chemistry to distinguish these new generation particles from their counterparts with PS core and PMMA arms). In this case, the PS arms could be stained selectively, thereby allowing direct visualization of the unstained CSNG-R cores and nanoparticle aggregations migrating to the interface.

Our earlier findings showed profound effect of surface tension/interfacial tension interplay on responsiveness of these core-shell nanoparticles. We have further explored the migration of these new-generation nanoparticles (CSNG-Rs) segregating from PS homopolymer to PS/PMMA interfaces. Unlike the dewetting patterns observed with the PMMA-arm particles, which exhibit classical nucleation and growth mechanism with circular hole formation, we have observed an intriguing dewetting pattern and CSNG-Rs forming lateral aggregates and tentacle-like structures at the interface. Our initial efforts have demonstrated that high-molecular-weight PS (both 204 and 879 kDa) layers can be stabilized on silicon substrates with the addition of 20 wt% CSNG-Rs. Preliminary experiments to study the stabilization effect of these new-generation particles by a member of the Spontak/Genzer groups, Xiaojing Cai, have demonstrated that after spin-casting, a nearly-monolayer ($\approx 10 \text{ nm}$ thick, considering the nanoparticle diameter is 13 nm) can be

floated onto DI water and remains stable. If the as-spun monolayer is annealed, it cannot be removed easily from the glass slide using a neutral (toluene) or PMMA-selective solvent (acetic acid), indicating that either (i) the acrylic core is able to interact with the silicon substrate or (ii) the monolayer is held tightly in place in-plane, almost like a network formed by the particles. Addition of the same PS-arm CSNG-Rs to the bottom layer of a double-layered laminate wherein a thick layer (≈ 100 nm) of high-molecular-weight PS (204 kDa or 879 kDa) is the bottom layer and PMMA (51 kDa) forms the top layer results in the formation of discrete “tentacular” features along the polymer/polymer interface. AFM images confirm that these features consist of 3D ridges and valleys. Further tests on mono- and single-layer stability tests will provide more insight on the evolution of lateral interfacial structuring in bilayer systems.

In parallel with our core-shell particle studies, we have also explored the structuring of copolymer molecules that are far from equilibrium in bulk and complex laminate of polymer thin films. Our early copolymer studies concentrated on exploring the effect of molecular asymmetry in triblock copolymers on order-disorder transition temperature, referred as T_{ODT} . Molecularly asymmetric poly(styrene-*b*-isoprene-*b*-styrene) triblock copolymers, designated as A_1BA_2 , were grown gradually from a parent poly(styrene-*b*-isoprene) diblock copolymer, designated as A_1B , in a progressively uniform fashion. Our mean-field theory calculations were in agreement with dynamic rheological results by our colleagues at Procter & Gamble Co., and have proven that the resultant ODT minimum is due to mixing between long B and short A_2 blocks.

Our main focus on copolymer studies consists of PS-*b*-PMMA diblock copolymer-containing bilayers of PS/PMMA. Thin films of the PS top layer measuring ≈ 60 -100 nm thick are not stable for the molecular weights examined (≈ 30 -216 kDa) and dewet spontaneously from the PMMA bottom layer when the bilayer assembly is annealed at temperatures above T_{g} of both homopolymers. Addition of the diblock copolymer to the PS layer is found to enhance generally the overall stability of the upper layer, as evidenced by the net reduction in dewetting rate (i.e., the hole growth velocity, dD/dt) seen for several copolymers at different concentrations. Film stability depends on a variety of factors, i.e., copolymer concentration, copolymer composition, film thickness and PS molecular weight. Dewetting rates at ultrathin interlayer thicknesses are higher than those of the neat PS for systems consisting of a neat PS or a mixed PS/SM copolymer top layer. As the thickness increases, the dewetting rate decreases and the roughness of the dry PMMA increases to a maximum and then decreases, suggesting that a stable copolymer brush assembly forms along the interface. In this PhD Thesis, we focus primarily on the effect of the copolymer chemical composition (i.e., block sizes) on the dewetting behavior of PS/SM thin films on PMMA. We elucidate the interfacial segregation and concurrent micellization of diblock copolymers in a dynamically evolving environment with changing boundary conditions as spherical holes develop. These studies reveal that in-plane interfacial nanostructures produced by block copolymers may not always provide stabilization of the bilayer; this behavior has been attributed to the interplay between copolymer micellization and copolymer segregation at the immiscible polymer interface. In order to comprehend this unexpected behavior, we have designed trilayer laminates in which block copolymer molecules are

directly placed at the PS/PMMA interface. The dewetting rate of the PS layer can be reduced if the PS₁₀-*b*-PMMA₅₀ midlayer is ≈ 6 nm or thicker. This observation is consistent with the expectation that the copolymer, if located at the PS/PMMA interface, will serve to stabilize the top layer, if the midlayer is sufficiently thick, presumably to form a contiguous layer.

Lastly, we have investigated the dewetting behavior of PS/PMMA assemblies containing compositionally varied mixtures of mirrored copolymers, such as PS₅₀-*b*-PMMA₁₀ / PS₁₀-*b*-PMMA₅₀ and PS₅₀-*b*-PMMA₂₀ / PS₂₀-*b*-PMMA₅₀. The dewetting rates of systems composed of copolymer mixtures lie between those of systems modified with the neat copolymers. This observation suggests that the dewetting behavior of the double layer with a copolymer mixture may be approximated satisfactorily by a linear rule of mixtures.

7.2 Conclusions

Our investigations and findings have been summarized under four general topics: 1) thermal response of PMMA-arm CSNGs, 2) nanoparticle architecture on dewetting mechanism and lateral structuring (PS-arm vs. PMMA-arm CSNGs), 3) effect of block copolymer composition and concentration on polymer thin-film stability (stability induced by mixing vs. destabilization due to micellization) and 4) copolymer mixtures in thin-films (competition between lateral structuring vs. micellization).

7.2.1 Thermal response of PMMA-arm CSNGs

In this study, we explore the behavior of CSNGs comprising a poly(methyl methacrylate) (PMMA) shell in molten PMMA thin films. The surface segregation and emergence of

CSMG nanoparticles from the PMMA matrix depends on the interplay between entropically-driven autophobicity and enthalpically-governed surface/interfacial energy. Autophobicity between the PMMA arms and the PMMA homopolymer forces the nanoparticles to segregate from the PMMA matrix and form aggregates along the surface. Autophobicity occurs due to two structural disparities between free (PMMA homopolymer) and surface-grafted (CSNGs) chains. The first is the high grafting density of the brush, forming the outer layer of the nanoparticles. The second factor is the disparity in chain length between the grafted PMMA arms and free PMMA homopolymer chains; the arms are much shorter (110 repeat units) than the PMMA homopolymer (2,260 repeat units). As a result of these factors, the CSNG nanoparticles have a tendency to segregate from long PMMA homopolymer chains and migrate to the free-air interface; however, the high surface energy of PMMA homopolymer film forces CSNGs to remain buried within the matrix (just beneath the surface), as evidenced by the absence (or disappearance) of nanoscale surface features revealed by AFM imaging. When a thin film of polystyrene (PS) is placed on top of a PMMA/CSNG layer, the nanoparticles segregate to and thus roughen the PMMA/PS interface, as evidenced by AFM analysis. We attribute this behavior to a change in surface vs. interfacial energies.

In order to fully comprehend the thermal response of these nanoparticles, we have varied systematically the annealing time of the particle-added PS/PMMA laminates under continuous N₂ flow. This study has not only revealed the kinetics of the particle elevation from/protrusion to PMMA homopolymer utilizing the interplay between surface energetics but also have shown another intriguing aspect of these grafted particles such as formation of block nanoparticle aggregates. Even at relatively short annealing times (e.g., 1 hour), AFM

topography scans have demonstrated that the PS/PMMA interface roughens due to particle presence in forms of 3-5 particle aggregates. As the annealing time is further increased, particle aggregates start forming chain-like structures, almost like a network. Our efforts in image analysis (calculating the overall the particle density, average aggregation number vs. annealing time, ratio of dewetted areas and number of holes vs. annealing time) and designing a model that would relate this particle aggregation/chain-forming behavior to the processing conditions warrants further investigation.

7.2.2 Nanoparticle architecture on dewetting mechanism and lateral structuring: PS-arm vs. PMMA-arm CSNGs

After our attempts to cross-section PS/PMMA bilayers containing CSNGs in the top PS film failed due to nature of the particles (PS core could not be stained due to the dense-PMMA brush corona), PS-arm/PEGDMA-core particles (CSNG-Rs) were synthesized and a thin-layer of CSNG-R layer was sandwiched between two thick-PS900 slabs. The samples were first cross-sectioned by using a microtome and then in-plane views were collected by means of TEM. Nanoparticle aggregates, not individual nanoparticles, could be clearly seen to migrate to the PS/PMMA interface, forming network-like aggregates. This behavior not only supports our earlier findings on segregation with reverse-type nanoparticles (CSNGs) but also can be attributed to the intramolecular interactions between particle arms.

We also extended our previous study to explore the effect of reverse core-shell microgel particles (CSNG-Rs) made of a cross-linked acrylic core and PS arms on interfacial activity at PMMA/PS contacts. The system is arranged such that a layer of PS homopolymer

(thickness ≈ 100 nm) containing the CSNG-Rs is deposited on top of flat silica surface and covered with the PMMA homopolymer film (thickness ≈ 60 nm). Upon annealing, the CSNG-Rs travel to the PMMA/PS interface. We explore the effect of 1) the CSNG-Rs molecular weight and concentration in the PS phase, and 2) the molecular weight of PS on the resulting segregation of the CSNG-Rs and the corresponding morphology of the PMMA/PS interface. Our earlier results have demonstrated the stabilization effect of PS-arm particles with 20 wt% loading on PS homopolymer layers at long annealing times at 180°C . As the particle concentration increases lateral structuring of the particles at the interface develops as evidenced by non-spherical shapes of the rims of dewetted holes. Both particle concentration and particle molecular weight have an effect on interfacial structuring. Annealing of a laminate with ≈ 15 wt% particle concentration, tentacular structures occur in-plane and dewetting rate slows down substantially. Optical microscopy images of the interface of a PMMA51/PS204 +15 wt% CSNG laminate (with the PMMA top layer removed by acetic acid) after long-time annealing at 190°C exhibit the tentacular features. AFM images confirm that these features consist of valleys. We attribute this behavior to the intramolecular organization and lateral structuring of CSNG-R aggregates at the PMMA/PS interface.

7.2.3 Effect of block copolymer nature and architecture on polymer thin-film stability: Stability induced by mixing vs. destabilization due to micellization

In this study, we investigate the effect of block size on the dewetting behavior of PS/SM thin films on PMMA substrates. Polystyrene (PS) loaded with poly(styrene-*b*-methyl methacrylate) (SM) diblock copolymer dewets at a slower rate from poly(methyl methacrylate) (PMMA) underlayer via classical nucleation and growth (NG) as evidenced by the presence of circular holes at 180°C. Upon long-time dewetting, various nanoscale topologies due to copolymer structuring in both dewetted and non-dewetted areas that depend sensitively on copolymer concentration and film thickness are observed.

Addition of a nearly-symmetric PS₅₀-*b*-PMMA₅₄ copolymer to PS decreases systematically the dewetting rate until the top PS/SM layer is eventually stabilized at relatively high copolymer concentrations (>10 wt% of SM copolymer). The time dependence of hole size is nearly linear. If the size of the PS block is held constant and the size of the PMMA block is varied (which reflects changes in incompatibility between the copolymer and PS matrix and, thus, the driving force for copolymer self-assembly), several important trends are observed. First, a reduction in PMMA block size promotes greater stabilization as the dewetting rate generally decreases. Such enhanced stabilization is accompanied by a reduced driving force for micellization, which implies that the copolymer molecules can populate effectively the PS/PMMA interface and affect stabilization. PS₅₀-*b*-PMMA₁₀ copolymer with the shortest PMMA block stabilizes the assembly at < 1 wt% copolymer. In addition, a sharp drop in dewetting rate remains evident from ≈0.8-1.0 wt% copolymer. Conversely, when the PS block is shortened and the driving force

for micellization is increased, the dewetting rate increases as well. The same drop in dewetting rate noted earlier remains apparent. These trends are likewise observed when the molecular weight of the top PS film is varied. Taken together, our results indicate that copolymer molecules with relatively short PMMA blocks segregate more readily from the PS matrix towards the PS/PMMA interface where they assemble with the short PMMA block penetrating effectively into the underlying PMMA substrate.

Despite reversed micelle morphologies, similar behavior is observed when the same SM copolymers are added to the bottom PMMA layer. While it appears that the crew-cut aggregates formed by the PS₅₀-*b*-PMMA₁₀ copolymer molecules are the most effective at stabilizing the double-layered assembly, it should be recognized that the increased driving force for micellization in copolymers possessing relatively large PS blocks may be compromised by the higher viscosity of the PMMA substrate.

7.2.4 Copolymer mixtures in thin-films: Competition between interfacial structuring vs. micellization

All individual copolymer stability trends and lateral structuring observed as a result of the copolymer micellization vs. copolymer/homopolymer mixing have provided insight into this complex segregation phenomenon. These experiments have suggested extensions involving the addition of mirrored diblock copolymer mixtures comprising SM copolymers with complementary chemical compositions in PS/PMMA laminates. Specifically, we have investigated the dewetting behavior of PS/PMMA assemblies containing compositionally-varied SN copolymer mixtures, i.e., PS₅₀-*b*-PMMA₁₀ / PS₁₀-*b*-PMMA₅₀ and PS₅₀-*b*-PMMA₂₀

/ PS_{20-*b*}-PMMA₅₀. One general observation is that the dewetting trends composed of copolymer mixtures lie between those of pure SM copolymer systems. This observation suggests strongly that the dewetting behavior of the double layer with a copolymer mixture may be approximated satisfactorily by a linear rule of mixtures. As a consequence, the dewetting behavior of mixtures of PS_{50-*b*}-PMMA₁₀ / PS_{10-*b*}-PMMA₅₀ with gradually-varying composition can be generalized by collapsing individual data sets in a master curve, which depicts the dewetting rate as a function of the composition of one of the SM copolymers in the mixture. We opt to use the PS_{10-*b*}-PMMA₅₀ copolymer composition as the leading independent variable and show that PS_{10-*b*}-PMMA₅₀/PS_{50-*b*}-PMMA₁₀ mixtures follow the aforementioned scaling behavior for the dewetting rate for all compositions up to 97wt% PS_{10-*b*}-PMMA₅₀. In mixture having PS_{10-*b*}-PMMA₅₀ in concentrations higher than 97wt% the dewetting rate becomes nearly independent of the PS_{10-*b*}-PMMA₅₀ copolymer concentration, approaching to the dewetting rates of the individual PS_{10-*b*}-PMMA₅₀ copolymer series. The stabilization effect of PS_{50-*b*}-PMMA₁₀ can be observed at 2wt% in composition at copolymer mixture concentrations of 1wt% or higher.

7.3 Recommendations for future work

SM diblock copolymers and PS-arm nanoparticles have demonstrated that they can be used as compatibilizers of immiscible PS/PMMA interfaces. Future work utilizing copolymers and nanoparticles in interfacial modifications is summarized under two main sections: core-shell nanoparticles and block copolymers.

7.3.1 Core-shell nanoparticles

Further investigation pertaining to particle analysis and chain formation of the particles (i.e., effect of number of arms on particle aggregation, particle size and the disparity between the particle and matrix molecular weight) would provide molecular-level understanding of the segregation behavior of the PMMA-arm particles. Diffusion-limited aggregation phenomenon might be another useful study pursue. Computer simulations should be employed to explore systematically the effect of the various structure parameters, i.e., molecular weight, arm length, grafting density of arms and crosslink density of the core, on autophobicity, and complement the experimental studies. This step will help to narrow down the broad parameter space and will assist in rational material design before actual experiments are conducted.

Designing experiments with coumarin-doped PMMA-armed particles, which are currently available in our inventory, can also be used to keep track of the migration of the nanoparticles, and their localization in the bulk and at the interface.

Stability of the bare PS-arm monolayer, thus, its effect both on the stabilization of a thin PS-layer on silicon wafer and on the formation of the tentacular-like structures at the PS/PMMA interface are rather intriguing observations; the reasons behind this phenomenon should be investigated by varying systematically the thickness of the PS-arm nanoparticle layer as well as changing the thickness and molecular weight of the PS layer.

Our preliminary results have shown that PMMA-arm particles can be patterned on PMMA homopolymer surfaces via electric field, without the need of a sacrificial PS layer. Although the Au substrate brings heterogeneities to the PMMA/CSNG layers, the findings

are very promising. The substrate can be switched from Au to silicon wafer, which would reduce the surface defects, on the other hand, the conductivity difference between Au and Si would play a role in tuning the electric field applied (i.e., change in voltage). If silicon substrate is used as an electrode, a higher voltage is needed to generate the same electric field effect compared to the one generated by utilizing Au electrodes because Au is more conductive than Si (even heavily doped). New design rules include the optimization of the gap between the electrodes (including switching from parallel electrodes to gradient-like gaps), voltage applied, and loading of the particles in the homopolymer matrix.

7.3.2 Block copolymers

Understanding the lateral self-assembly structuring along the immiscible interfaces is the key point of this study. In order to develop deeper molecular-level insight micellization kinetics of the block copolymers should be explored via computer simulations. Our most current collaboration with Professor An-Chang Shi of McMaster University will provide us with invaluable insight on non-equilibrium conditions of copolymer micellization kinetics.

Our efforts in determining the PS domains in PS/SM copolymer/PMMA trilayer systems by using an IR microscope were not successful due to the detection limitations of the instrument. Alternative methods such as a free electron laser-photoemission electron microscope system (FEL PEEM) might be helpful to comprehend the lateral structuring at the PS/PMMA interface by locating the PS domains when copolymer molecules are directly placed at the interface. A more thorough study of systematical AFM imaging (i.e., time vs. annealing on hole formation, hole shape, change in interfacial area for PS/PMMA laminates)

would aid us have a deeper understanding of time series of copolymer structuring at the interface.

Copolymer mixture studies have helped us create new experimental designs. It would be useful to vary the copolymer pair composition for the other mirrored copolymer mixture, $PS_{50}\text{-}b\text{-}PMMA_{20}$ / $PS_{20}\text{-}b\text{-}PMMA_{50}$. Additionally, experiments with mixtures of different copolymer pairs such as $PS_{10}\text{-}b\text{-}PMMA_{50}$ / $PS_{50}\text{-}b\text{-}PMMA_{54}$, $PS_{20}\text{-}b\text{-}PMMA_{50}$ / $PS_{50}\text{-}b\text{-}PMMA_{50}$ and $PS_{10}\text{-}b\text{-}PMMA_{50}$ / $PS_{20}\text{-}b\text{-}PMMA_{50}$) can be performed to study the controlled micelle core effect in dewetting and lateral structuring. In order to comprehend completely the system behavior, dewetting studies by means of optical microscopy and AFM would have to be complemented with TEM investigations in order to understand the structure of the copolymer (including copolymer aggregates) in the vicinity of the PS/PMMA interface.

Considering the stability effect both observed via the utilization of copolymer molecules and PS-arm nanoparticles, block copolymers mixed with CSNG-Rs might open vast opportunities in accessible morphologies and thus, exploring this complex structuring phenomenon occurring at immiscible interfaces.

Preliminary results of dewetting trends on designs with different geometries (i.e. copolymer-added PS layer on a PMMA bottom layer vs. copolymer-added PMMA layer on a on PS layer) have demonstrated tremendous disparity in stability for these systems. This system should also be investigated in more details.

The results from this PhD thesis and the future studies on interfacial modification will provide alternative routes to tailored and responsive polymer films and surfaces.